Title
Atomistic Simulations of Extended Defects in Metals

Author
Freitas, Rodrigo

Publication Date
2018

Peer reviewed|Thesis/dissertation

Atomistic Simulations of Extended Defects in Metals

by
Rodrigo Freitas

A dissertation submitted in partial satisfaction of the
requirements for the degree of
Doctor of Philosophy

in

Engineering - Materials Science and Engineering

in the

Graduate Division
of the
University of California, Berkeley.

Committee in charge:
Professor Mark Asta, Co-Chair
Dr. Vasily Bulatov, Co-Chair
Professor Daryl Chrzan
Professor Sanjay Govindjee

Spring 2018

Atomistic Simulations of Extended Defects in Metals

Abstract

Atomistic Simulations of Extended Defects in Metals

by

Rodrigo Freitas
Doctor of Philosophy in Engineering – Materials Science and Engineering
University of California, Berkeley

Professor Mark Asta, Co-Chair
Dr. Vasily Bulatov, Co-Chair

In this dissertation the thermodynamic and kinetic properties of extended defects in metals are investigated using atomistic simulation methods, i.e., methods in which the behavior of individual atoms is explicitly considered. The dissertation is divided into two main applications. The first presents a study of surface steps where a theory for the thermodynamic properties of steps on faceted crystalline surfaces is introduced, leading to the development of an equation for the temperature dependence of the step free energy γ^{st}. The application of this new formalism is demonstrated in thermodynamic-integration (TI) calculations of γ^{st}, based on Molecular Dynamics (MD) simulations, considering $\langle 110 \rangle$ steps on the $\{111\}$ surface of a classical potential model for elemental copper for a temperature range of zero up to the melting point. Calculated results for γ^{st} show relatively weak temperature dependencies up to a homologous temperature of 0.6, above which the temperature dependence becomes strong and γ^{st} becomes more isotropic. It is found that γ^{st} remains finite up to the melting point, indicating the absence of a roughening temperature for this $\{111\}$ surface facet, but γ^{st} decreases by roughly fifty percent from the zero-temperature value. At high temperatures the step becomes configurationally disordered due to the presence of appreciable capillary fluctuations; these fluctuations are investigated by computing the fluctuation spectrum near the melting temperature. Step stiffnesses are derived from the fluctuation analysis and the values obtained are compared to γ^{st} as obtained from the TI study. Results from the capillary-fluctuation analysis and TI calculations yield statistically significant differences that are discussed within the framework of statistical-mechanical theories for configurational contributions to step free energies. The second application of the dissertation focuses on the study of quantum effects on dislocation motion. The thermally activated motion of dislocations in α-iron is investigated using a simulation method that rigorously accounts for quantum effects on the dynamics of condensed-phase systems, namely the Ring-Polymer Molecular Dynamics method. Calculated results for the flow stress of $\frac{1}{2}\langle 111 \rangle$ screw dislocations indicate that arguments based solely on the zero-point energy of the system overestimate the observed reduction in the Peierls stress by a factor of four as they do not account for the atomic quantum dispersion, i.e., the finite size of the atomic wave function as opposed to the point-particle representation in classical mechanics.

Contents

Chapter 1: Introduction **1**
1.1 Defects in metals . . . 1
1.2 Method development in computational materials science . . . 3
1.3 Dissertation outline . . . 5

Chapter 2: Theory and simulation methods **7**
2.1 The embedded-atom method . . . 7
2.2 Molecular Dynamics . . . 9
2.3 Ring-Polymer Molecular Dynamics . . . 13
2.4 Ring-Polymer Molecular Dynamics code implementation . . . 17

Chapter 3: Step free energies at faceted solid surfaces **25**
3.1 Motivation and overview . . . 25
3.2 Thermodynamic theory of surface steps . . . 26
3.3 Thermodynamic integration formalism . . . 31
3.4 Atomistic simulations . . . 35
3.5 Results and discussion . . . 38
3.6 Summary and conclusions . . . 43

Chapter 4: Capillary fluctuations of surface steps **47**
4.1 Motivation and overview . . . 47
4.2 Capillary-wave model . . . 48
4.3 Methodology of atomistic simulations . . . 52
4.4 Results . . . 59
4.5 Discussion . . . 61
4.6 Summary and conclusions . . . 63

Chapter 5: Quantum effects on dislocation motion **65**
5.1 Motivation and overview . . . 65
5.2 Results and discussion . . . 65
5.3 Summary and conclusions . . . 71

Chapter 6: Summary and future work **73**
6.1 Thermodynamics and kinetics of surface steps . . . 73
6.2 Quantum effects on dislocation motion . . . 75

References **76**

Appendix A: Convergence of thermodynamic integration for steps **91**

Appendix B: Simulation of quantum and classical dislocation motion **93**

Acknowledgments

I would like to thank my advisors, Mark Asta and Vasily V. Bulatov, for their guidance and teaching. I also thank the collaborators and co-workers I've been lucky to have over the past years: Tim Frolov, Maurice de Koning, Tomas Oppelstrup, Alfredo Correa, Babak Sadigh, and Luis Zepeda-Ruiz. I would also like to thank Professor Jeff J. Hoyt for the valuable discussions and input on the work on surface steps, and also for giving me freedom and support in conducting the discussion sections for MSE-103.

I would also like to thank the members of the dissertation committee, Professor Daryl Chrzan and Professor Sanjay Govindjee, as well as the other members of the qualifying exam committee, Professor Andrew Minor and Professor Gerbrand Ceder, for their critical examination of this work and their helpful comments and suggestions.

The work presented in this dissertation would have not been possible without the financial support provided by different sources. I would like to acknowledge the Livermore Graduate Scholar Program from Lawrence Livermore National Laboratory for the funding provided. Computing support for the research on quantum effects on dislocation motion came from the Institutional Computing Grand Challenge program at LLNL. The work on thermodynamics and kinetics of surface steps was supported by the U.S. National Science Foundation (Grant No. DMR-1105409 and No. DMR-1507033).

Chapter 1:

Introduction

The origins of materials science as an academic subject are rooted in the empirical approach of traditional metallurgy. Many of the processes of traditional metallurgy were developed before microscopy was able to reveal the nanoscale features of materials: metallurgists were manipulating and controlling elements of the microstructure of materials that they did not know and could not see. The advent of microscopy techniques with resolution higher than light microscopes and the maturation of theoretical materials science created, jointly, the materials analysis paradigm, namely relating the structure of a material to its properties. This new strategy for materials engineering in which mechanism-based understanding can be hoped to lead to new materials was augmented by the introduction of computational models of materials, with which the study and theoretical modeling of increasingly complex materials and their constituent microstructure elements was made possible. This dissertation is focused on the advancement and application of atomistic modeling methods for studying microstructure elements of crystalline solids, i.e., crystal defects. Due to the broadness of this field we will restrict ourselves to line defects in crystalline metals: a class of crystal imperfections that is complex to model because of their spatial extension and long-range strain fields, in contrast to localized point defects for example.

1.1 Defects in metals

Defects in crystalline metals [1, 2] are regions where the periodic arrangement of atoms according to the underlying crystal lattice is broken. Figure 1.1 illustrates three different crystal defects, all obtained from real atomistic simulations. In fig. 1.1a we have a surface step [3–5]: an abrupt interruption of the first surface layer (colored in yellow in the figure). Steps are regions where atomic attachment is much more energetically favorable than a region with a flat surface, one can think in terms of broken bonds: atoms on the step edge have more broken bonds than atoms in a perfectly flat surface, therefore they will attract a nearby atom, from the crystal melt for example, more strongly. The prediction and understanding of step properties is fundamental to the understanding of crystal growth. Figure 1.1b illustrates a grain boundary [6–8]: the interface between two crystals with different orientations, atoms in the immediate vicinity of the grain boundary are colored in grey, while the perfect crystal grains are colored in blue. Differently from surface steps, grain boundaries are usually deep inside the crystal, this allow them to act as sources and sinks for point defects such as vacancies and interstitials, making the understanding of grain boundaries fundamental in developing radiation-resistant materials for example. Their energetics and motion are also key to understanding the phenomena of grain growth and recrystallization in the processing of materials. In fig. 1.1c we have a network of dislocations [9, 10], different colors are used for

different Burgers vectors. Dislocations are fundamental in understanding crystal plasticity, when dislocations move around they carry with them a small amount of plastic deformation defined by the Burgers vector, allowing metals to deform plastically. The interaction between grain boundaries and dislocations is one of the most important in understanding the mechanical behavior of crystalline metals.

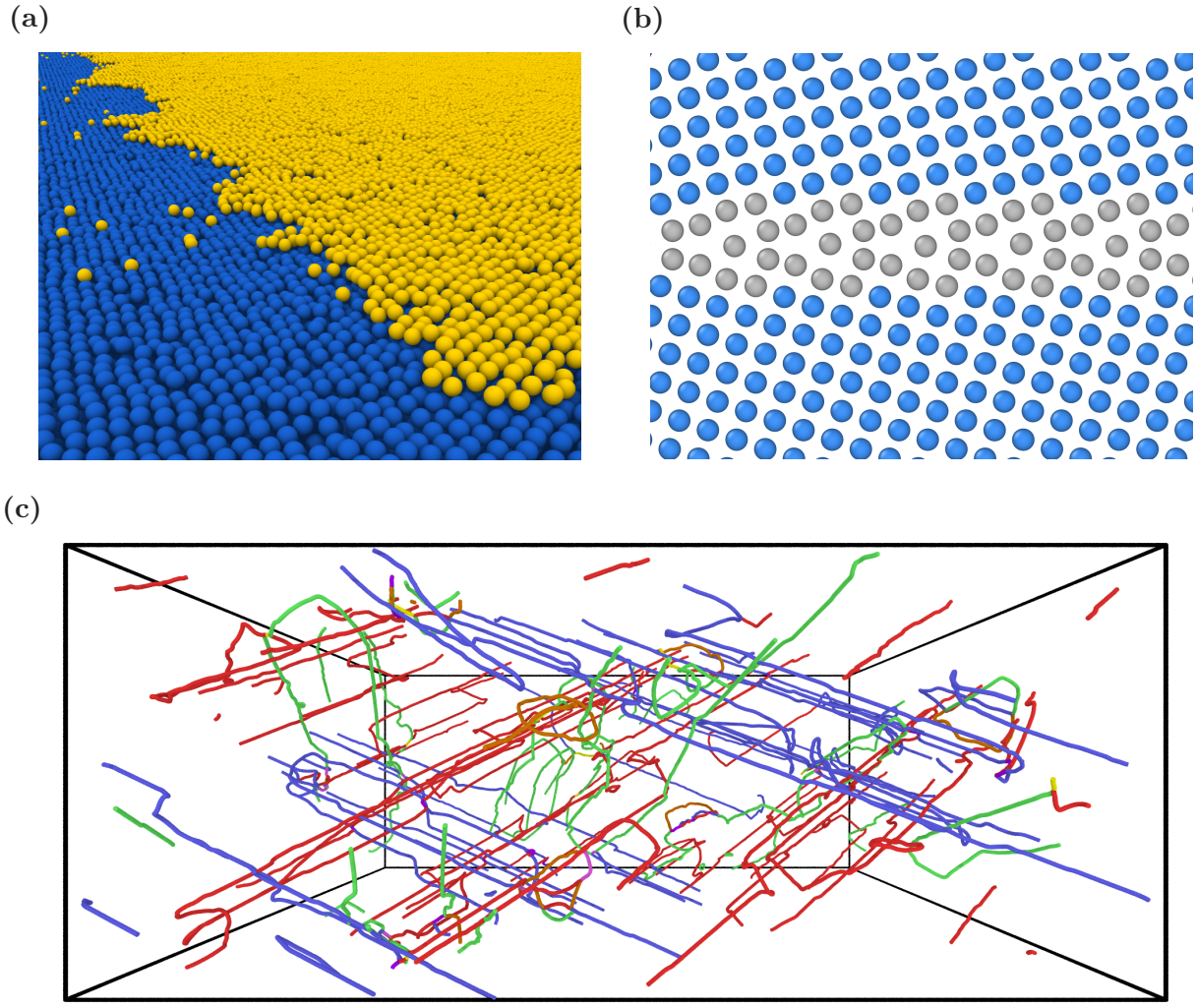

Figure 1.1: **(a)** Surface step. Atoms belonging to the crystal first layer were colored in yellow to facilitate the visualization of the step. **(b)** Grain boundary. Atoms in blue belong to perfect crystal structure, atoms in gray are in the immediate vicinity of the grain boundary interface. **(c)** Network of dislocations. Each color represents a different Burgers vector for that dislocation [11]. The dislocation line information shown was extracted from an atomistic simulation with 58 million atoms.

One of the goals of materials engineering is to leverage the rich assortment of defects features to tailor materials properties. Let us consider for example nanotwinned metals [12], a material with high strength and considerable ductility, a combination that is difficult to obtain but of utmost importance for structural materials. Nanotwinned metals are polycrystalline solids with grains of $\sim 1\mu$m that present a high density of coherent twin boundaries

(CTB) separated by a few nm, forming regular structures. Compared to other materials with the same composition, nanotwinned metals have superior strength and resistance to failure, properties attributed to the interaction between defects in them, namely the dislocations' interaction with the CTBs. For dislocations to move inside a nanotwinned metal they need to be transmitted across CTBs since the nanoscopic spacing between the boundaries inhibit dislocation motion and pile-up within the grains. But the CTBs represent a high energetic barrier for dislocation motion, resulting in a material with high strength. Besides altering the properties of nanotwinned metals, the defects also allow the adjustment of the mechanical properties by changing the CTB separation distance and geometry, thereby allowing the fine tuning of the material's properties to a specific application.

The engineering of materials such as nanotwinned metals requires a fundamental understanding of the mechanism behind its properties, thus it is of paramount importance to have a deep comprehension of defects. For example, we would like to understand how defects interact with each other, for CTB it is the twin boundary interaction with dislocations that result in the remarkable properties of nanotwinned metals. Another important property of defects is their thermal stability, one of the biggest difficulties in developing nanocrystalline metals [13, 14] is avoiding grain growth, or coarsening, which destroys nanostructure and all properties arising from them consequently.

It is our goal in this dissertation to study the fundamental physical properties of defects in metals. Chapters 3 and 4 focus on the physics of surface steps and their thermodynamic and kinetic properties. In chapter 5 we examine the role of quantum effects in dislocation motion, which is related to fundamental questions in the physics of dislocations.

1.2 Method development in computational materials science

The steady increase in computational power has enabled the numerical modeling of complex systems of interest in materials science, including extended defects and interfaces in metals. One evidence of the widespread availability of powerful computers for modeling materials is the recent establishment of large collaborative projects aimed at building databases of materials properties obtained solely from computer simulations [15, 16]. Nevertheless, the advancement of the field of computational materials science has come not only through the development of increasingly powerful computers, comparatively important contributions came in the way of novel simulation methodologies. Consider for example the method of Molecular Dynamics (MD), frequently used to simulate atomistic systems where the dynamics of the atoms is described by classical mechanics. The MD method was first introduced by Berni Alder and Thomas Wainwright [17] in the late 1950's when they investigated systems of 32 to 500 hard-sphere particles inside a box of fixed volume using the most advanced computers at the time. It is often pointed out that nowadays the simulation of hundreds of millions of atoms [11] using interatomic potentials that are computationally much more intensive than the hard-sphere potential are possible due to the increase in computational power. But comparatively large advancements have also been made to the MD methodology, expanding it far beyond its initial capabilities. For example, a few notable contributions are

- the seminal work of Shuichi Nosé [18] and William Hoover [19] in using the extended

Lagrangian formalism to formulate the equations of motion for constant-temperature MD.

- the development of a Lagrangian which allowed the simulation of systems under the most general conditions of externally applied stress by Michele Parrinello and Aneesur Rahman [20].

- the development of a formalism for generating MD integrators by Mark Tuckerman and coworkers [21].

- the formulation of the embedded-atom method (EAM) for interatomic potentials, which incorporates the picture of metallic bonding and allows the simulation of metallic alloys, by Michael Baskes, Murray Daw, and Stephen Foiles [22].

- the extension of molecular dynamics beyond the interatomic potentials formulation by combining it with density functional theory (also known as *ab initio* molecular dynamics) by Roberto Car and Michele Parrinello [23].

- the development of path-integral molecular dynamics [24, 25] for computing equilibrium properties of quantum systems at finite temperature through the classical isomorphism between the quantum and classical partition functions, first observed by Richard Feynman and Hagen Kleinert [26].

- the development of nudged elastic band [27] and similar "string" methods, allowing the estimation of minimum energy paths for a multitude of processes in materials science and related fields.

- the development and formalization of the transition path sampling technique [28], allowing the formulation of barrier-crossing events in a solid statistical mechanical framework; and the reliable calculation of transition rates for thermodynamic conditions where atomistic simulations could not be applied due to timescale problems.

The development of these sophisticated methods, and many others, have allowed the simulation of different and complex materials under a wide variety of external condition. Moreover, novel methods often allow the calculation of materials properties that were not possible to be obtained from simulations before, expanding the range of applicability of computer simulations of materials.

In this dissertation we examine properties of extended defects that, despite the advances in computational capabilities, have proven to be challenging to simulate with the currently available simulation techniques and theories. For example, in chapters 3 and 4 we study how the free energy of surface steps can be computed from two different methods based on thermodynamics and statistical mechanics models of these defects. Despise the importance of the step free energy, as described in the previous section, measurements of this quantity remain relatively rare. In chapter 5 we study how quantum effects can affect the thermally activated motion of dislocations. Despite recent studies suggesting that some quantum effects should have important consequences on dislocation motion, no direct and unbiased simulation of the quantum motion of dislocations has been undertaken so far.

1.3 Dissertation outline

The remainder of this dissertation is organized as follows. Chapter 2 includes a discussion of the theory and methods relevant for the remainder of the dissertation. We start by describing the physical theory behind the embedded-atom method, which is the level of theory chosen to treat the interatomic interactions between metallic elements in chapters 3, 4, and 5. We also present in chapter 2 two simulation methods that are employed in this dissertation: the Molecular Dynamics method and the Ring-Polymer Molecular Dynamics method, used to compute canonical ensemble averages and dynamic properties of classical and quantum systems, respectively. Finally, we describe our implementation of the Ring-Polymer Molecular Dynamics method in LAMMPS [29], an open source and parallel software for Molecular Dynamics simulation.

In chapter 3 we present a general thermodynamic formalism relating changes in step free energy to variations in chemical potential, surface free energy, temperature, and non-hydrostatic strains. This formalism provides the basis for a new computational framework for calculations of step free energies under general thermodynamic conditions. We demonstrate the application of the formalism in thermodynamic-integration calculations of the temperature dependence of the step free energy for $\langle 110 \rangle$ steps on the $\{111\}$ surface of a classical potential model for elemental copper using Molecular Dynamics simulations, from zero temperature to the melting point.

In chapter 4 we consider the application of the capillary-fluctuation method (CFM) for studying thermodynamic and kinetic properties of steps on crystalline surfaces, focusing on a classical interatomic potential model of elemental copper as a representative model metal system. We employ equilibrium Molecular Dynamics simulations at a homologous temperature of 0.98 to analyze the step fluctuation spectra of $\langle 110 \rangle$ and $\langle 211 \rangle$ steps on the $\{111\}$ surface. The simulation study involves a detailed analysis of system-size effects and methods for determining dynamic step positions. Our focus on the Cu(111) system enables a direct comparison with the results in chapter 3, which are discussed within the framework of statistical-mechanical theories for configurational contributions to step free energies.

The role of quantum effects on dislocation motion is investigated in chapter 5. The quantum motion of atoms was proposed to explain a long-standing discrepancy between theoretically computed and experimentally measured low-temperature resistance (Peierls stress) to dislocation motion in iron and possibly other body-centered cubic metals. We present a study of thermally-activated dislocation motion in α-iron at low temperatures using the Ring-Polymer Molecular Dynamics simulation method, an approach that rigorously accounts for quantum-fluctuation effects on the dynamics of dislocation motion, including zero-point energy, atomic quantum dispersion, and barrier tunneling, while making no assumptions about the Peierls-barrier crossing events. The calculated result for the Peierls stress using Ring-Polymer Molecular Dynamics are compared to the value from classical dynamics, as obtained from Molecular Dynamics simulations. We discuss what competing factors are involved in determining the importance of quantum effects on dislocation motion.

In chapter 6 we present a summary highlighting the main conclusions and results. We also discuss directions and suggestions for future work.

Chapter 2:

Theory and simulation methods

2.1 The embedded-atom method

When modeling materials it is necessary to pick a level of theory to describe the material's relevant physical features. The models employed in this dissertation explicitly account for individual atoms and their interactions; numerical modeling within this level of theory is known as *atomistic simulation* of materials [30, 31]. The most important input in atomistic simulations is the description of the interatomic interactions, because it is from them that all properties of the material emerge. The problem of describing atomic interactions between a set of atoms can be fundamentally reduced to the explicit solution of the quantum mechanical equations for the atoms' electrons [32], from which it is possible to compute the force on each atom or any other property of this system. At the time of writing the status of this approach, known as *ab initio* simulations, is such that it cannot be applied to more than a few hundreds of atoms due to the prohibitive computational cost of solving the electronic equations involved. Hence, the simulation of systems large enough for the investigation of the thermodynamics and kinetics of extended defects in metals requires a treatment of interatomic interactions that is computationally less intensive. Such reduction in computational cost can be achieved with methods where the interaction between atoms is obtained directly from analytical mathematical functions that make no explicit reference to electrons, bypassing the need to solve the quantum mechanical electronic equations involved in *ab initio* methods. These functions, known as interatomic potentials or force fields, are decidedly less accurate than *ab initio* methods but still capture important characteristics of the chemical bonding relevant to the material under study. In this dissertation the interatomic interactions between atoms is modelled using the embedded-atom method [22, 33, 34] (EAM); a class of potentials appropriated for metallic bonding.

In order to better understand the physical motivation behind the EAM potential, let us consider first the following pairwise potential for a system of N atoms[1]:

$$U_{\text{pair}} = \sum_{i=1}^{N} \sum_{j>i}^{N} V(r_{ij}), \tag{2.1}$$

where $V(r_{ij})$ is a two-body interaction between the atom pair (i, j), and r_{ij} is the distance between the pair of atoms. The fundamental assumption behind all potentials with this functional form is that the bond between any two atoms is independent from all other bonds in the system, this can be seen in eq. (2.1) by noticing that the potential energy due to the interaction between atoms i and j, $V(r_{ij})$, does not depend on any property (such as

[1]For clarity it is assumed that all atoms in the system are the same metallic element.

the distance) of the surrounding atoms $k \neq i$ or j. The hypothesis that the strength of the bond between two atoms is unaffected by the presence of other nearby bonds can be tested by considering the two following quantities: the cohesive energy of an atom in a solid and the vacancy formation energy in the same system. The cohesive energy of a pairwise potential is the sum of the interaction energy between all atoms bonded to a certain atom i. Likewise, the vacancy formation energy is, within the pairwise approximation, the energy necessary to break each of the bonds between atom i and all other atoms. Therefore, pairwise potentials predict that the cohesive energy and the vacancy formation energy should be exactly the same. It is well known that this does not hold true for metallic systems, consider for example copper (used in the simulations of chapters 3 and 4): the cohesive energy is 2.7 times larger than the vacancy formation energy. The origin of this discrepancy is that when atomic bonds are broken (in order to form a vacancy for example) the nearby atomic bonds are *strengthened*: the less coordination an atom in a metallic system has, the stronger and shorter its bonds with neighboring atoms will be. Thus, metallic bonding is notably non-pairwise and interatomic potentials for metals require the inclusion of coordination-dependent bonding beyond the pairwise functional form of eq. (2.1).

The EAM potential incorporates an approximation to the many-atom interactions neglected by pairwise potentials, the EAM functional form introduced by Daw and Baskes [22] in 1984 is

$$U_{\text{eam}} = \sum_{i=1}^{N} \sum_{j>i}^{N} V(r_{ij}) + \sum_{i=1}^{N} F(\rho_i), \tag{2.2}$$

where U_{eam} is the potential energy of a system with N atoms, F is known as the embedding energy, and ρ_i the electron density at the position where atom i is located:

$$\rho_i = \sum_{j \neq i} \rho(r_{ij}),$$

where $\rho(r)$ is the electron density at r created by an atom at the origin. Thus, the energy of an atom is the energy of embedding the atom in the local electron density provided by all its neighbors; this feature of EAM potentials is what accounts for the coordination-dependent character of metallic bonds. For example: atoms near defects, such as a surface, are embedded in an electron density that is different from the electron density for bulk atoms. Notice how the functional form of the EAM potentials appeal to our intuitive understanding of metallic bonding [35], where an atom's valence electrons abandon the atom's immediate neighborhood to join the valence electrons of other atoms in forming a "sea of free electrons" that surrounds all atoms (ions, to be precise), creating an electronic density distribution in which all system's atoms are embedded in.

One important remark about the functional form in eq. (2.2) is that the separation of the potential energy into a pairwise term and a many-atom term is completely arbitrary, as discussed next. We have argued before that for pairwise potentials the bonds are independent of each other, thus the cohesive energy increases linearly with the coordination of an atom, but this is the same as saying that the cohesive energy increases linearly with the electron density. Therefore, adding a linear contribution to the embedding function, $F(\rho)$, can translated exactly into an equivalent change in the pairwise component of U_{eam}. In fact, if $F(\rho)$ is completely linear it can be shown that the resulting EAM potential in eq. (2.2)

can be cast into the pairwise potential form of eq. (2.1). Hence, it is the nonlinearity of the embedding function that incorporates the many-atom interactions and results in the increase in bond strength as the coordination is decreased (or, equivalently, in the saturation of the metallic bond as the coordination is increased).

Since EAM's first formulation, the exact functional form of $V(r)$, $\rho(r)$, and $F(\rho)$ have varied wildly, from physically-motivated functions to general splines treated only as fitting functions. Of considerable more importance nowadays is the consideration of the materials properties to which these functions have been fitted to. This is a reflection of the limited transferability of interatomic potentials, the prudent approach has been to trust EAM potentials only as interpolations between quantities it has been fitted to, and perhaps extrapolation slightly outside this region, always keeping in mind that interatomic potentials do not capture all nuances of chemical bonds. Nevertheless, with careful considerations of the limits of applicability, EAM potentials make it possible to investigate a plethora of defects and processes of importance in metallic systems, such as point defects, grain boundaries, dislocations, melting and solidification, alloying, dislocations, and surface defects.

2.2 Molecular Dynamics

2.2.1 Time evolution

Interatomic potentials, such as the EAM, allow us to compute the potential energy $U(\mathbf{r}_1, \mathbf{r}_2, \ldots, \mathbf{r}_N)$ of a system composed of N metallic atoms. Moreover, with $U(\mathbf{r})$ we can, in principle, compute all static properties of this system, such as the force $\mathbf{F}_i = -\partial U/\partial \mathbf{r}_i$ on atom i. In order to obtain dynamic properties it is necessary to consider the time evolution of the system. For clarity let us write $\mathbf{r} = \{\mathbf{r}_1, \mathbf{r}_2, \ldots, \mathbf{r}_N\}$ for the coordinates and $\mathbf{p} = \{\mathbf{p}_1, \mathbf{p}_2, \ldots, \mathbf{p}_N\}$ for the conjugated momenta, where $\mathbf{p}_i \equiv \partial \mathcal{L}/\partial \dot{\mathbf{r}}_i$ and $\mathcal{L}$ is the system's Lagrangian. The classical equations of motion for this system are given by Hamilton's equations:

$$\begin{cases} \dot{\mathbf{p}}_i = -\dfrac{\partial \mathcal{H}}{\partial \mathbf{r}_i} \\ \dot{\mathbf{r}}_i = \dfrac{\partial \mathcal{H}}{\partial \mathbf{p}_i} \end{cases} \tag{2.3}$$

for $i = 1, 2, \ldots, N$, where

$$\mathcal{H}(\mathbf{r}, \mathbf{p}) = \sum_{i=1}^{N} \frac{\mathbf{p}_i^2}{2m} + U(\mathbf{r})$$

is the system's Hamiltonian. Because $U(\mathbf{r})$ is, in general, too complicated for the equations of motion to be solved analytically, we discuss in this section a method for solving eqs. (2.3) numerically.

The numerical solution of eqs. (2.3) is not trivial because it is necessary that all symmetries and conservation laws in Hamilton's equations are observed and adequately taken into account in the numerical algorithm [36]. For example, from Hamilton's formulation of classical mechanics we know that the equations of motion can all be derived from a function, namely the Hamiltonian $\mathcal{H}(\mathbf{r}, \mathbf{p})$, as shown in eqs. (2.3). This is a very specific property of eqs. (2.3), since not all differential equations can be generated from a function. Thus, if we

want numerical solutions for eqs. (2.3) that obey the properties of classical mechanics we need to account for eqs. (2.3) properties and symmetries into the numerical algorithm, also known as the *integrator*. Tuckerman, Berne, and Martyna [37] were the first to show how to systematically derive integrators that contain all necessary physical properties. For example, the integrator needs to be time reversible and symplectic (i.e., conserve phase-space volume under time evolution). The simplest and most used symplectic integrator is the velocity Verlet algorithm, which was first derived [38] in 1907 by Störmer [39] and later popularized[2] by Verlet [41] in 1967, and shown to be symplectic by Tuckerman et al. [37] in 1992. We can summarize the steps involved in the velocity Verlet as follows:

$$(1) \quad \mathbf{p}_i(t + \tfrac{\Delta t}{2}) = \mathbf{p}_i(t) + \frac{\mathbf{F}_i(t)}{m}\frac{\Delta t}{2}$$

$$(2) \quad \mathbf{r}_i(t + \Delta t) = \mathbf{r}_i(t) + \frac{\mathbf{p}_i(t + \frac{\Delta t}{2})}{m}\Delta t$$

(3) Compute $\mathbf{F}_i(t + \Delta t)$ using $\mathbf{r}_i(t + \Delta t)$.

$$(4) \quad \mathbf{p}_i(t + \Delta t) = \mathbf{p}_i(t + \tfrac{\Delta t}{2}) + \frac{\mathbf{F}_i(t + \Delta t)}{m}\frac{\Delta t}{2}$$

(5) Go back to (1) with $t \equiv t + \Delta t$.

Given an interatomic potential for the system, $U(\mathbf{r})$, and a set of initial conditions $\{\mathbf{r}(t = 0), \mathbf{p}(t = 0)\}$, we can use the velocity Verlet algorithm to solve the equations of motion and obtain $\mathbf{r}(t)$ and $\mathbf{p}(t)$ for $t > 0$, from which we can compute the system's properties at time t. This numerical simulation technique is known as *Molecular Dynamics* (MD) [36].

2.2.2 Ensemble averages

Consider $\{\mathbf{r}(t), \mathbf{p}(t)\}$ for t in the interval $0 \leq t \leq t_{\mathrm{f}}$, as obtained from a MD simulation. In classical mechanics the position and momentum of the particles is all the information needed to fully characterize the physical state of the system at any given moment, but to understand how meaningful thermodynamic information can be extracted from this data we need a short digression into statistical mechanics [36]. In order to simplify the notation we use $\mathrm{x}(t) \equiv \{\mathbf{r}(t), \mathbf{p}(t)\}$ in this section.

In statistical mechanics x is known as a *microstate*: a point in the vector space, known as the *phase space*, of this system of particles. In contrast, a *macrostate* is defined by a set of thermodynamic variables, such as the system temperature, volume, and density. Given a specific macrostate of the system there are a multitude of microstates that are compatible with the set of thermodynamic variables defined by the macrostate, we call the set of microstates sharing a common macrostate an *ensemble*. The macrostate of the system imposes certain constraints that cause the microstates of this ensemble to be clustered more

[2] According to ref. [38] the first appearance of the Verlet integrator can be traced back to Sir Isaac Newton's *Principia* [40], in the figure for Theorem I.

densely in certain regions of the phase space and less densely in others. Thus, the distribution of systems in an ensemble is described by a phase-space distribution function $\rho(\mathrm{x})$ such that

$$\rho(\mathrm{x}) \geq 0 \qquad \text{and} \qquad \int \rho(\mathrm{x})\ \mathrm{dx} = 1,$$

where the integral is over the entire phase space, i.e., each vectorial coordinate of the position and momentum of each particle is integrated from $-\infty$ to $+\infty$.

Consider now a certain property $A(\mathrm{x})$ of the system that is a function of the microstate x. For example, $A(\mathrm{x})$ could be the system energy $A(\mathrm{x}) = \mathcal{H}(\mathrm{x})$, or the system pressure:

$$P(\mathrm{x}) = -\frac{\partial \mathcal{H}}{\partial V}.$$

When a macroscopic measurement of $A(\mathrm{x})$ is made we do not measure the instantaneous value of $A(\mathrm{x})$, what is actually measured is the average value of $A(\mathrm{x})$ as weighted by the distribution function $\rho(\mathrm{x})$ corresponding to the ensemble defined by the macrostate constraints:

$$\langle A \rangle \equiv \int \mathrm{dx}\, A(\mathrm{x})\rho(\mathrm{x}). \tag{2.4}$$

We call this an ensemble average. One can intuitively understand that this averaging comes from the fact that the macroscopic measurement made is over a large extension of the system dimension, which could be divided into many "sub-systems" of N particles, each on its own microstate x with probability $\rho(\mathrm{x})$.

The thermodynamic information to be extracted from MD simulations is of the form $\langle A \rangle$, as given by eq. (2.4). But, as discussed in the beginning of this section, the data extracted from a MD simulation is $\mathrm{x}(t)$ for $0 \leq t \leq t_\mathrm{f}$, not $\rho(\mathrm{x})$ for all x in the phase space, which is need to compute $\langle A \rangle$ using eq. (2.4). The connection between the information extracted from MD simulations and the result of an ensemble average is justified as follows. As the system evolves in time the point that represents its location on the phase space moves around, creating the system trajectory, $\mathrm{x}(t)$, on the phase space as it visits different microstates. The specific trajectory taken by the system depends on the constraints imposed by the macrostate, the very same constraints that result in the distribution $\rho(\mathrm{x})$, therefore the system will only visit microstates belonging to the same ensemble along its trajectory. Let us define now the following *time average* of $A(\mathrm{x})$:

$$\bar{A} \equiv \lim_{t_\mathrm{f}\to\infty} \frac{1}{t_\mathrm{f}} \int_0^{t_\mathrm{f}} \mathrm{d}t\, A[\mathrm{x}(t)] \approx \frac{1}{M} \sum_{i=1}^{M} A[\mathrm{x}(t_i)]$$

where $t_{i+1} - t_i \equiv \tau$, $M = t_\mathrm{f}/\tau$, and τ is a time interval longer than any correlation time of physical events happening in this system. The right-hand side of the equation above is the time average estimate as obtained from the MD simulation data. Given t_f long enough, it is reasonable to assume that the system visits all microstates accessible to it; moreover, the frequency of these visits is determined by the same constraints that define the system ensemble. It is reasonable then to assume that the ensemble average and the time average should give the same result: $\langle A \rangle = \bar{A}$. Thus, provided this assumption (known as Ergodic

hypothesis[3]) holds, we can compute time averages from MD simulations that correspond to thermodynamic information about the system under study.

2.2.3 The canonical ensemble and the Langevin thermostat

In the canonical ensemble the macroscopic constraints consist of specifying the system temperature T, volume V, and number of particles N. In a system where these thermodynamic variables are specified, the microstates are distributed on the phase space according to the Boltzmann distribution:

$$\rho(\mathrm{x}) = \frac{1}{N!h^{3N}} \frac{\mathrm{e}^{-\beta\mathcal{H}(\mathrm{x})}}{Z(N,V,T)} \tag{2.5}$$

where h is the Planck constant, $\beta \equiv 1/k_{\mathrm{B}}T$, k_{B} is the Boltzmann constant, and

$$Z(N,V,T) = \frac{1}{N!h^{3N}} \int \mathrm{dx}\, \mathrm{e}^{-\beta\mathcal{H}(\mathrm{x})}$$

is known as the partition function.

The velocity Verlet algorithm described in sec. 2.2.1 results in a system dynamics compatible with Hamilton's equations, eqs. (2.3), and it is a conservation law inherent of Hamilton's equations that energy is conserved along any trajectory obtained from eqs. (2.3). Given all microstates with the same energy E there are no physical grounds for picking one microstate as being more probable than any other microstate, therefore the distribution function must be $\rho_{\mathrm{micro}}(\mathrm{x}) \propto \delta[E - \mathcal{H}(\mathrm{x})]$ where $\delta(\mathrm{x})$ is the Dirac delta distribution, notice that it favors equally all microstates with energy E. The ensemble with constant energy, volume, and number of particles is known as the microcanonical ensemble. Hence, if we want to measure thermodynamic properties of systems at fixed temperature T we need to modify the velocity Verlet algorithm to sample $\rho(\mathrm{x})$ as given by eq. (2.5) instead of $\rho_{\mathrm{micro}}(\mathrm{x})$.

There are multiple algorithms that modify the velocity Verlet integrator to sample the canonical ensemble distribution, throughout this dissertation we have chosen to use the so-called Langevin thermostat [31], where Hamilton's equations, eqs. (2.3), are modified as follows:

$$\begin{cases} \dot{\mathbf{p}}_i = -\dfrac{\partial\mathcal{H}}{\partial\mathbf{r}_i} + \mathbf{f}_i(\mathbf{p}_i, t) \\ \dot{\mathbf{r}}_i = \dfrac{\partial\mathcal{H}}{\partial\mathbf{p}_i} \end{cases}$$

with

$$\mathbf{f}_i(\mathbf{p}_i, t) = -\gamma\mathbf{p}_i(t) + \sqrt{2m\gamma k_{\mathrm{B}}T}\,\mathbf{R}_i(t),$$

[3] Another intuitive way to justify the validity of the Ergodic hypothesis and the equivalence of $\langle A\rangle$ and $\bar{A}$ is to think of eq. (2.4) as arising not because a macroscopic measurement is made over a large extension of the system but, instead, because the microscopic state of the system $\mathrm{x}(t)$ changes fast with time when compared to the time taken to perform the macroscopic measurement. For example, the time for an atom to oscillate back and forth in a typical metal is $\mathcal{O}(10^{-13}\,\mathrm{s})$, while the time taken to make temperature measurements using a fast thermocouple is $\mathcal{O}(10^{-3}\,\mathrm{s})$. Thus, the macroscopic measurement result (i.e., the ensemble average) is nothing but the average of $A(\mathrm{x})$ as the system moves around the phase space constrained by the macrostate properties. But this is exactly the information obtained from a MD simulation, provided that the simulation length is long enough for the system to sample the phase-space satisfactorily.

where γ is a friction coefficient, and the second term on the right-hand side is a random and impulsive force with $\mathbf{R}_i(t)$ a Gaussian random number with variance equal to one such that

$$\langle \mathbf{R}_i(t) \rangle = 0 \qquad \text{and} \qquad \langle \mathbf{R}_i(t)\mathbf{R}_j(t') \rangle = \delta(t-t')\delta_{ij}.$$

Thus, the dynamics created by the Langevin thermostat is stochastic and it consists of adding to each particle a drag force proportional to the particle momentum, and a random force with no memory and zero average, also known as a white noise. Notice that these two forces added by the Langevin thermostat are not independent, the magnitude of the random force is related to the magnitude of the drag force by the dissipative force parameter γ. It is because of this specific connection between the forces, which itself is a manifestation of the fluctuation-dissipation theorem, that it can be rigorously shown that the trajectories obtained from MD simulations using the Langevin thermostat sample the Boltzmann distribution, eq. (2.5), instead of $\rho_{\text{micro}}(\text{x})$.

2.3 Ring-Polymer Molecular Dynamics

Atomic motion dynamics in MD simulations is assumed to be classical, eqs. (2.3); thus the properties computed from MD do not account for quantum mechanical effects on the atomic motion, which are known to result in important contributions to physical properties of systems composed of light atoms or systems at low temperatures. In this section we present a practical approach, namely Ring-Polymer Molecular Dynamics (RPMD), to include quantum dynamical effects in atomistic simulations.

2.3.1 Path-Integral Molecular Dynamics

The PIMD method [36, 42–44] is a numerical technique for simulating atomistic systems while taking into account quantum statistical effects on ensemble averages. In the next paragraphs we will give a short description of this method by considering a one dimensional system composed of a single particle, the generalized equations for a system of N particles in three dimensions is given in sec. 2.4.

Let us start by considering some elements of the path-integral formulation of quantum mechanics [45, 46]. Suppose that the particle's initial wavefunction is $\Psi(x,0)$ and that after $t = 0$ this system evolves in time until a later time t while under the influence of a Hamiltonian $\hat{H} = \hat{T}+\hat{V}$, where $\hat{T}$ is the kinetic energy operator and $\hat{V}$ is the potential energy operator. The probability associated with measurements performed at t is determined by the wavefunction $\Psi(x,t) = \langle x|\Psi(t)\rangle$ that can be computed by using the time-evolution operator $\hat{U}(t) = \mathrm{e}^{-i\hat{H}t/\hbar}$:

$$\Psi(x,t) = \langle x|\hat{U}(t)|\Psi(0)\rangle = \int \mathrm{d}x' \, \langle x|\mathrm{e}^{-i\hat{H}t/\hbar}|x'\rangle\langle x'|\Psi(0)\rangle = \int \mathrm{d}x' \, U(x,x';t)\Psi(x',0),$$

where $U(x,x';t) \equiv \langle x|\mathrm{e}^{-i\hat{H}t/\hbar}|x'\rangle$ is known as the quantum propagator. Therefore, $\Psi(x,t)$ is determined by the matrix elements of the quantum time-evolution operator in the position

representation: $U(x,x';t)$. According to the path integral formulation of quantum mechanics [45, 46] we can represent the quantum mechanical propagator as

$$U(x,x';t)=\int_{x(0)=x}^{x(t)=x'}\mathcal{D}x(s)\exp\left\{\frac{i}{\hbar}\int_0^t \mathrm{d}s\left[\frac{1}{2}m\dot{x}^2(s)-V(x(s))\right]\right\}, \tag{2.6}$$

where $\int\mathcal{D}x(s)$ is an integration along all possible functions $x(s)$ that satisfy the endpoint conditions $x(0)=x$ and $x(t)=x'$, also known as a functional integration. Note that the integrand inside the exponential is just the classical Lagrangian $\mathcal{L}(x,\dot{x},t)$ and therefore the integral over s is the classical action $A[x(s)]$ of a specific classical path $x(s)$. Thus, the contribution to the functional integral of a given path $x(s)$ that begins at x and ends at x' in time t is weighted by the complex exponential $\exp(iA[x(s)]/\hbar)$.

The connection between the path-integral representation of the quantum propagator, eq. (2.6), and the PIMD method comes from considering the important similarity between the quantum propagator and the canonical density matrix:

$$\hat{U}(t)=\mathrm{e}^{-i\hat{H}t/\hbar}\qquad\text{and}\qquad\hat{\rho}(\beta)=\mathrm{e}^{-\beta\hat{H}}, \tag{2.7}$$

or $\hat{U}(-i\beta\hbar)=\hat{\rho}(\beta)$ and $\hat{\rho}(it/\hbar)=\hat{U}(t)$. Hence, the density matrix can be obtained by evaluating the propagator at imaginary times, which can be interpreted as a rotation in the complex plane (known as Wick rotations). We can explore this similarity to develop an expression for the quantum partition function for the canonical ensemble, defined in quantum statistical mechanics as

$$Z(T)\equiv\mathrm{Tr}\big[\hat{\rho}(\beta)\big]=\int\mathrm{d}x\,\rho(x,x;\beta). \tag{2.8}$$

where $\rho(x,x';\beta)\equiv\langle x|\mathrm{e}^{-\beta\hat{H}}|x'\rangle$ is the matrix element of the density matrix in the position representation. First we notice that the functional integral in eq. (2.6) can be discretized[4] [42] as:

$$U(x,x';t)=\lim_{P\to\infty}\left(\frac{mP}{2\pi it\hbar}\right)^{P/2}\int\mathrm{d}x_2...\,\mathrm{d}x_P \tag{2.9}$$
$$\exp\left\{\frac{i}{\hbar}\sum_{k=1}^{P}\left[\frac{mP}{2t}(x_{k+1}-x_k)^2-\frac{t}{2P}\Big(V(x_{k+1})+V(x_k)\Big)\right]\right\}$$

where in we have denoted $x_1\equiv x$ and $x_{P+1}\equiv x'$. Next, if we use eq. (2.7) to evaluate eq. (2.9) at $t=-i\beta\hbar$ (Wick rotation) and substitute this result in the expression for the partition function [eq. (2.8)] we obtain

$$Z(T)=\lim_{P\to\infty}\left(\frac{m\omega^2\beta}{2\pi}\right)^{P/2}\int\mathrm{d}x_1\,\mathrm{d}x_2...\,\mathrm{d}x_P\,\exp\left\{-\beta\sum_{k=1}^{P}\left[\frac{m\omega^2}{2}(x_{k+1}-x_k)^2+\frac{1}{P}V(x_k)\right]\right\}, \tag{2.10}$$

[4] One could understand the process of discretizing a functional integral as being analogous to transforming a regular integral over an interval into a Riemann sum. Equation (2.9) can also be obtained from $U(x,x';t)=\langle x|\hat{U}(t)|x'\rangle$ by using Trotter's theorem [36].

where we have denoted $\omega \equiv \sqrt{P}/\beta\hbar$. This equation can be made clearer by rewriting it as:

$$Z(T) = \lim_{P\to\infty} \int \mathrm{dx}\, \mathrm{e}^{-\beta \mathcal{H}_{\mathrm{rp}}(\mathrm{x},P)}, \tag{2.11}$$

where $\mathrm{x} \equiv \{p_1, p_2, \ldots, p_P, x_1, x_2, \ldots, x_P\}$ and

$$\mathcal{H}_{\mathrm{rp}}(\mathrm{x}, P) \equiv \sum_{k=1}^{P} \left[\frac{p_k^2}{2m'} + \frac{m\omega^2}{2}(x_{k+1} - x_k)^2 + \frac{1}{P} V(x_k) \right]$$

is known as the *ring-polymer Hamiltonian*, with $m' = mP/(2\pi\hbar)^2$.

Equation (2.10) possesses some fascinating physical content, first noted by Feynman and Kleinert [42], that reveals the essence of the PIMD method. On the left-hand side we have the canonical partition function of the one-particle quantum system described by the Hamiltonian operator $\hat{H}$, from which all equilibrium properties of the quantum system can be derived from. For finite P the right-hand side of eq. (2.10) resembles the configurational partition function of a *classical* system of P particles connected to each other through harmonic springs as to form a closed loop[5]. This resemblance is fully explored in rewriting the prefactor of eq. (2.10) as Gaussians integrals to obtain the momentum variables p_k in eq. (2.11). In the common jargon of the field of path-integral methods the closed loop of particles is known as *ring polymer* and each particle is referred to as a *bead*. The similarity between the quantum partition function of system $\hat{H}$ to the classical partition function of the ring-polymer system $\mathcal{H}_{\mathrm{rp}}$ was coined *classical isomorphism* by Chandler and Wolynes [47]. The classical isomorphism between the partition functions guarantees that ensemble averages computed in the classical system of ring polymers can be converted exactly to equivalent ensemble averages for the quantum system in the limit of $P \to \infty$, i.e., in the limit of an infinitely long ring polymer. Hence, the PIMD consists of using MD simulations to compute ensemble averages of the ring-polymer system, $\mathcal{H}_{\mathrm{rp}}$, with which we can obtain ensemble averages of the quantum system. In sec. 2.4 it is shown how to compute ensemble averages for quantum system from the information gathered from the classical ring-polymer system. An important part of this process is the convergence of results from PIMD simulations with the number of beads P, in chapter 5 we demonstrate how this convergence is achieved for different physical systems.

2.3.2 Quantum dynamics

Let us now consider dynamical properties of quantum systems in thermal equilibrium [36, 45]. Many of these properties can be directly related to the time correlation function between two operators

$$c_{AB}(t) = \langle \hat{A}(0)\hat{B}(t) \rangle = \frac{1}{Z} \mathrm{Tr}\left[\mathrm{e}^{-\beta\hat{H}} \hat{A}(0)\hat{B}(t) \right], \tag{2.12}$$

where $\hat{B}(t) = U^{\dagger}(t)B(0)U(t)$. It is possible to compute $c_{AB}(t)$ exactly at $t = 0$ using PIMD, because in this case it will be reduced to an ensemble average between two operators as

[5]Notice in eq. (2.10) that we have $x_{P+1} = x_1$, which closes the polymer ring. This condition comes from the fact that only closed Feynman paths are necessary to compute the density matrix elements in eq. (2.8).

measured in the same instant: $c_{AB}(0) = \langle \hat{A}(0)\hat{B}(0)\rangle = \langle \hat{A}\hat{B}\rangle$. If the extended phase space defined by the ring-polymer Hamiltonian, $\mathcal{H}_{\mathrm{rp}}(\mathrm{x})$, can be used to compute $c_{AB}(0)$, it is reasonable to ask if the classical dynamics of this same artificial phase space is capable of reproducing the quantum dynamics of the system defined by $\hat{H}$, i.e., if the following is a good approximation for the correlation function:

$$c_{AB}(t) \approx \frac{1}{N!h^P Z_{\mathrm{rp}}} \int \mathrm{dx}\, \mathrm{e}^{-\beta\mathcal{H}_{\mathrm{rp}}(\mathrm{x})} A\left[\mathrm{x}(0)\right] B\left[\mathrm{x}(t)\right],$$

where Z_{rp} is the partition function of the ring-polymer system. This possibility, first proposed by Craig and Manolopoulos [48], was considered based on physical arguments that seemed to indicate that this approach could give a reasonable short-time approximation to quantum correlation functions[6], eq. (2.12). It is now known that eq. (2.14) can indeed capture the dynamics of quantum system under certain conditions, and this approach became to be known as RPMD [49]. In the remainder of this section we present the qualities and limitations of the RPMD method, our goal is to make the assumptions behind RPMD clear, instead of delving into the theoretical demonstration of how RPMD arises from the exact quantum dynamics.

It is a fundamental assumption of the RPMD method that the system is in thermal equilibrium. This assumption is necessary because RPMD is derived from PIMD, which is used to compute ensemble averages of quantum systems in thermal equilibrium. It is important to notice that the assumption of thermal equilibrium affects the dynamics of the system in not only that the ensemble distribution is given the canonical density operator, but also in that the interaction between the system and the thermal reservoir will erase any memory of the system's initial state. It will be discussed extensively in chapter 5 how the motion of dislocations can be examined as to make sure that the thermal equilibrium assumption holds.

The most important limitation of the RPMD method is the lack of quantum coherence [49], i.e., the wavefunction phase information is not included in the RPMD equations of motion, causing all coherence effects in RPMD to derive from thermal fluctuation effects, which typically cannot persist beyond the thermal time $\beta\hbar$. The intrinsic lack of quantum coherence of RPMD is due to the fact that the classical isomorphism is obtained from the partition function, which defines only equilibrium properties – and some quasi-equilibrium properties through Green-Kubo linear response theory. Once we bring the system far from equilibrium the partition function is not enough anymore to predict the system's behavior;

[6] In reality, $\mathcal{H}_{\mathrm{rp}}$ gives a good short-time approximation to the Kubo-transformed correlation function, defined as

$$\tilde{c}_{AB}(t) = \frac{1}{Z}\int_0^\beta \frac{1}{\beta}\mathrm{Tr}\left[\mathrm{e}^{-(\beta-\lambda)\hat{H}}\hat{A}(0)\mathrm{e}^{-\lambda\hat{H}}\hat{B}(t)\right]\mathrm{d}\lambda. \tag{2.13}$$

This correlation function – which arises naturally in the analysis of real-time quantum dynamics – possesses the same symmetries as the classical correlation function. The Fourier transform of the time correlation function and the Kubo-transformed correlation function are related by

$$c_{AB}(\omega) = \frac{\beta\hbar\omega}{1-\mathrm{e}^{-\beta\hbar\omega}}\tilde{c}_{AB}(\omega), \tag{2.14}$$

thus, knowledge of one is enough to determine the other one.

in this regime the system's properties become strongly dependent on the initial conditions and, therefore, it is fundamental to capture all quantum coherence effects by fully solving the exact quantum dynamics from Schrodinger's equation. In practice the limitation due to the lack of quantum coherence can be understood as an implicit assumption that thermal fluctuations lead to quantum decoherence (i.e., quantum coherence dissipation) in a timescale much shorter than any natural timescale for the system in consideration. This assumption means that between any two barrier-crossing events, such as vacancy or interstitial hopping, the system is given enough time to thermalize in such way that the next barrier-crossing event has its initial state draw from the canonical ensemble distribution, thus not being affected by the last event. This has shown to be a good approximation for many condensed-phase problems, where system-bath interactions and strong intermode coupling cause the dominating effects on the dynamics of these systems to be due the equilibrium quantum statistics and not quantum coherence. Another important limitation of RPMD is that the method does not sample exchange moves between identical particles, in practice this means that exchange effects are ignored, resulting in the sampling of the quantum Boltzmann distribution instead of the Bose-Einstein or Fermi-Dirac distributions.

Historically both approximations – lack of quantum coherence and exchange effects – have shown to be fundamental in obtaining the dynamics of quantum systems with more then a few hundred atoms, given the great computational cost of algorithms that do not make such approximations. Moreover, the repertoire of successful applications of RPMD [49] to a wide variety of physical systems have demonstrated that these approximation are very accurate for many condensed-phase systems. For example, RPMD has been successfully applied to para-hydrogen [50] at temperatures as low as 14 K, where the diffusion coefficients computed from RPMD agree with experimental results. RPMD has also been applied to electron-transfer reactions in water [51], where the computed reaction rates across 13 orders of magnitude are in excellent agreement with exact quantum mechanical methods, with the only deviation occurring in the regime where quantum coherence effects become an integral part of the reaction mechanism, but in this regime RPMD fails to capture the essential physics of the reaction.

One important benefit of the RPMD method is that its consists of performing classical MD simulations on the extended phase space defined by $\mathcal{H}_{\mathrm{rp}}$, thus its implementation can draw on a multitude of efficient computational methods and techniques developed over the years for MD simulations. In the next section we give the generalized RPMD equations for N particles in three dimensions and we present our implementation of RPMD in a publicly available and widely adopted MD code.

2.4 Ring-Polymer Molecular Dynamics code implementation[7]

In section our RPMD implementation in LAMMPS [29] is described. First we give the generalized equations of the RPMD method in sec. 2.4.1, then we provide essential details

[7]The results presented in this section, chapter 5, and appendix B have been submitted to publication as an article with title "*Quantum effects on dislocation motion from Ring-Polymer Molecular Dynamics*" by Rodrigo Freitas, Mark Asta, and Vasily V. Bulatov [52]. The material is presented here with the permission of the coauthors.

of our RPMD implementation in LAMMPS in sec. 2.4.2, and finally we present two critical tests of our implementation comparing our RPMD-LAMMPS predictions to known analytical results for the harmonic oscillator (sec. 2.4.3) and to data previously computed using path-integral Monte Carlo [53] for the Stillinger-Weber model of silicon (sec. 2.4.4).

2.4.1 The ring-polymer system and the classical isomorphism

The ring-polymer Hamiltonian describes a classical system of $P \times N$ identical particles of mass m organized into N polymer rings each containing P particles (also known as "beads"), each ring representing a single atom:

$$\mathcal{H}_{\text{rp}} = \sum_{i=1}^{P} \left\{ \sum_{n=1}^{N} \left[\frac{\mathbf{p}_{n,i}^2}{2m} + \frac{1}{2} k \left(\mathbf{r}_{n,i+1} - \mathbf{r}_{n,i} \right)^2 \right] + \frac{1}{P} V(\mathbf{r}_{1,i}, \mathbf{r}_{2,i}, \ldots, \mathbf{r}_{N,i}) \right\} \tag{2.15}$$

where $\mathbf{r}_{n,i}$ and $\mathbf{p}_{n,i}$ are the coordinate and momentum, respectively, of the ith bead belonging to the nth ring-polymer (atom), $k = mP/(\beta\hbar)^2$ is the stiffness constant of springs connecting particles belonging to the same ring-polymer (atom), and $V(\mathbf{r}_{1,i}, \mathbf{r}_{2,i}, \ldots, \mathbf{r}_{N,i})$ is the many-body interatomic potential through which all beads with the same number i (one per polymer) interact. Given that each polymer is a ring, $\mathbf{r}_{n,P+1} = \mathbf{r}_{n,1}$ and $\mathbf{p}_{n,P+1} = \mathbf{p}_{n,1}$ for each atom $n = 1, 2, \ldots, N$. Figure 2.1 is a schematic illustration of a ring-polymer system in which beads with different numbers i are shown in different colors and only the beads of the same color n (within the same replica) interact with each other through the many-body potential V. The equations of motion obtained from eq. (2.15) for $P \times N$ particles are

$$\begin{cases} \dot{\mathbf{r}}_{n,i} = \dfrac{\mathbf{p}_{n,i}}{m} \\ \dot{\mathbf{p}}_{n,i} = -k(2\mathbf{r}_{n,i} - \mathbf{r}_{n,i+1} \quad -\mathbf{r}_{n,i-1}) - \dfrac{1}{P} \dfrac{\partial V(\mathbf{r}_{1,i}, \mathbf{r}_{2,i}, \ldots, \mathbf{r}_{N,i})}{\partial \mathbf{r}_{n,i}}. \end{cases}$$

By comparison to the classical system, the many-body interaction potential through which the particles within each replica n interact is P times weaker (scaled down) than the classical potential $V(\mathbf{r}_{1,i}, \mathbf{r}_{2,i}, \ldots, \mathbf{r}_{N,i})$, whereas the string stiffness k increases linearly with P. It can be shown that canonical ensemble averages of a quantum system described by Hamiltonian operator

$$H = \sum_{n=1}^{N} \left[\frac{\mathbf{P}_n^2}{2m} + V(\mathbf{R}_1, \mathbf{R}_2, \ldots, \mathbf{R}_N) \right]$$

are the same as the canonical ensemble averages of the classical ring-polymer system [36] defined by eq. (2.15) in the limit of $P \to \infty$. In particular, the ensemble average energy of the quantum system at temperature T can be estimated by averaging the following quantity of the classical ring-polymer system with finite number of beads P:

$$E_P = \frac{3}{2} N P k_{\text{B}} T - \sum_{n=1}^{N} \sum_{i=1}^{P} \frac{1}{2} k \left(\mathbf{r}_{n,i+1} - \mathbf{r}_{n,i} \right)^2 + \frac{1}{P} \sum_{i=1}^{P} V \left(\mathbf{r}_{1,i}, \mathbf{r}_{2,i}, ..., \mathbf{r}_{N,i} \right). \tag{2.16}$$

Likewise, the stress tensor is estimated as

$$(\sigma_{\alpha\beta})_P V = -N P k_{\text{B}} T \, \delta_{\alpha\beta} + \sum_{i=1}^{P} \sum_{n=1}^{N} \left[k \left(r_{n,i}^{(\alpha)} - r_{n,i+1}^{(\alpha)} \right) \left(r_{n,i}^{(\beta)} - r_{n,i+1}^{(\beta)} \right) - \frac{1}{P} F_{n,i}^{(\alpha)} r_{n,i}^{(\beta)} \right], \tag{2.17}$$

where α and β are x, y, or z, and $\mathbf{F}_{n,i}$ is the force exerted the many-body potential V on bead i of polymer n. Finally, the pressure is

$$\mathcal{P}_P = -\frac{1}{3}\sum_{\alpha=x,y,z}(\sigma_{\alpha\alpha})_P = PN\left(\frac{k_\mathrm{B}T}{V}\right) - \frac{1}{3V}\sum_{i=1}^{P}\sum_{n=1}^{N}\left[k\left(\mathbf{r}_{n,i}-\mathbf{r}_{n,i+1}\right)^2 - \frac{1}{P}\mathbf{F}_{n,i}\cdot\mathbf{r}_{n,i}\right].$$

2.4.2 LAMMPS algorithm

Figure 2.1 is a key schematic of our RPMD implementation in LAMMPS. Each of the N ring-polymers represents a single atom and is made up of P beads (classical particles) of different "colors" (the colors are used here to aid visualization, otherwise all particles within each ring-polymer are identical). Each bead interacts through the springs with its two immediate neighbors within the same ring-polymer. Beads of the same color belonging to different ring-polymers interact with each other through the scaled down many-body potential $\frac{1}{P}V(\mathbf{r}_{1,i},\mathbf{r}_{2,i},\ldots,\mathbf{r}_{N,i})$.

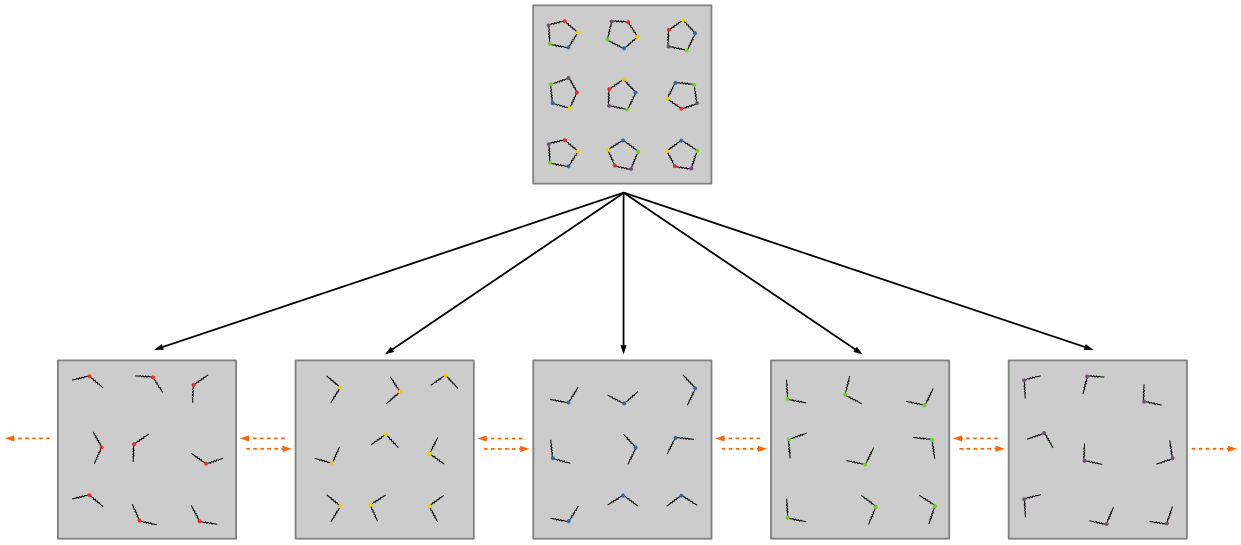

Figure 2.1: A schematic of workload partitioning and communications in RPMD-LAMMPS simulations. The $P\times N$-dimensional RPMD model is divided in P partitions, each containing beads of only one color. Calculations of spring forces within each ring-polymer and other related calculations require communications between partitions (orange arrows).

We have implemented a new command in LAMMPS called `fix rpmd`. This fix separates an RPMD-LAMMPS simulation into P independent classical MD simulations, or partitions, each partition containing beads of only one color, as shown in fig. 2.1. `fix rpmd` computes the many-body interaction among beads within each partition and performs inter-partition communications needed to compute spring interactions between beads belonging to the same ring-polymers. For the latter, `fix rpmd` defines the spring constant k and maintains a neighbor list of beads within each ring-polymer independent of the usual neighbor lists of particles within each partition. Additionally, the same fix tracks which parallel process each bead belongs to - calculations within each partition (color) are typically run on more than

one processor - and synchronizes neighbor list communications within each partition. Finally, `fix rpmd` calculates observables such as eqs. (2.16) and (2.17). In addition to parameters defined according to the standard LAMMPS specifications in the input script, the only additional input needed for `fix rpmd` to work is a target simulation temperature T and the number of replicas P (necessary to define the spring constants).

Our computational experiments show that, within parallelization model implemented in `fix rpmd` and illustrated fig. 2.1, LAMMPS achieves nearly perfect parallel efficiency with respect to the number of partitions for $P > 3$ (because each partition only communicates with two other partitions). A moderate hidden cost in our parallelization model is that inter-partition communications increase with the number of processors per partition since each partition needs to communicate whereabouts of its atoms (position and processor) potentially to all processors belonging to its two neighbor partitions.

2.4.3 Harmonic oscillator

Quantum harmonic oscillator is defined by the following Hamiltonian

$$H = \frac{\mathbf{P}^2}{2m} + \frac{1}{2}m\omega^2\mathbf{R}^2,$$

where $\mathbf{R}$ and $\mathbf{P}$ are operators of position and momentum vectors, respectively. The ensemble-average energy of this model system at temperature T can be calculated exactly [36] and is

$$\langle E\rangle_{\text{quantum}} = \frac{3}{2}\hbar\omega\coth\left(\frac{\hbar\omega}{2k_{\text{B}}T}\right).$$

For comparison, the average energy of an equivalent classical harmonic oscillator is

$$\langle E\rangle_{\text{classical}} = 3k_{\text{B}}T$$

and does not depend on frequency ω. Similarly, solution for the average energy of the ring-polymer with P beads defined by eq. (2.15) is

$$\langle E_P\rangle = 3k_{\text{B}}T\sum_{l=1}^{P}\frac{1}{1+\left[\left(\frac{2k_{\text{B}}T}{\hbar\omega}\right)P\sin\left(\frac{l\pi}{P}\right)\right]^2}.$$

The latter solution has two limits with respect to the number of beads:

$$\langle E_1\rangle = \langle E\rangle_{\text{classical}}$$

and

$$\lim_{P\to\infty}\langle E_P\rangle = \langle E\rangle_{\text{quantum}},$$

as expected from eq. (2.15): a ring-polymer with just one bead corresponds to the classical system whereas the exact quantum solution is recovered in the limit $P \to \infty$. To verify our RPMD implementation we performed a series of simulations with different number of beads at a low temperature defined by $\hbar\omega/k_{\text{B}}T = 9.5$, i.e. fairly deep into the quantum regime of

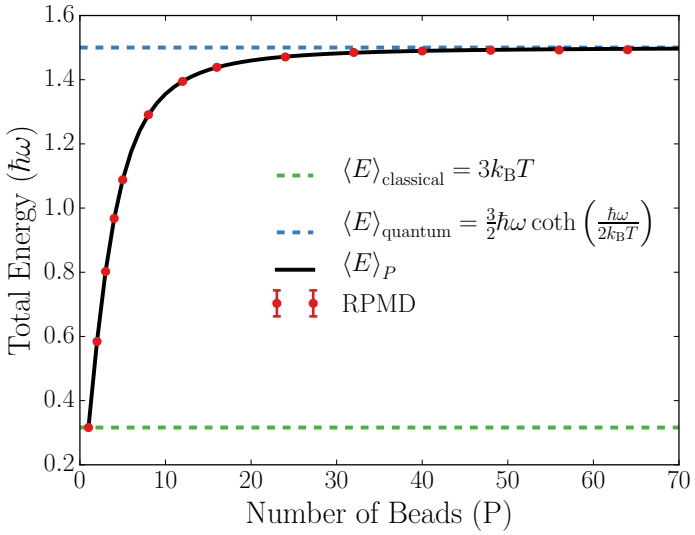

Figure 2.2: Average energy of a quantum harmonic oscillator (red solid circles) computed in RPMD simulations as a function of the number of beads P. The solid line is the analytical solution and two dashed lines are the quantum (top) and the classical (bottom) limits.

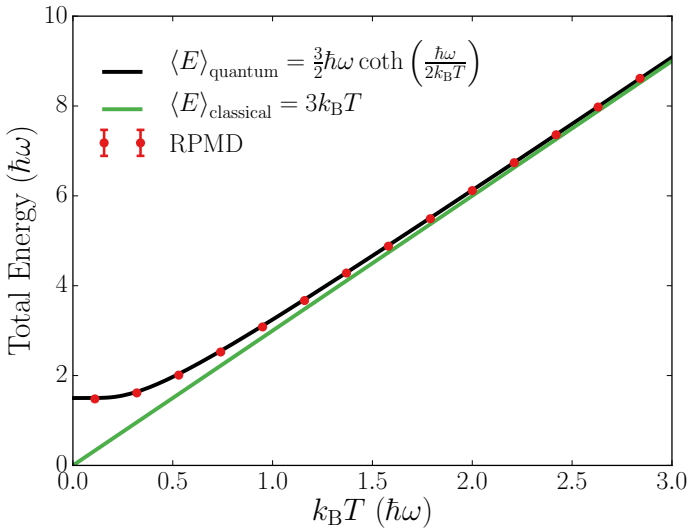

Figure 2.3: Average energy of a quantum harmonic oscillator obtained in RPMD simulations as a function of temperature (red symbols). The green line is the analytical solution for the classical oscillator and the black line is the analytical solution for the quantum oscillator. Note the close agreement between our fully converged RPMD simulations and the analytical solution.

the harmonic oscillator. Average energies of ring-polymers computed in RPMD are shown in fig. 2.2 along with the analytical solutions above. As can be seen from the plot, 40 to 50 beads are required to achieve reasonable convergence of RPMD simulations at this particular temperature.

Figure 2.3 shows average energy of a quantum harmonic oscillator obtained in RPMD simulations at different temperatures. The analytical solutions for the classical and the quantum harmonic oscillators are also shown for comparison. Clearly, in the limit of high temperatures quantum effects become negligible and the classical result is recovered. In the opposite limit of low temperatures, quantum nature of oscillations becomes increasingly dominant. When extrapolated to $T = 0$, the exact zero-point energy (ZPE) of a quantum harmonic oscillator is recovered, at $3\hbar\omega/2$.

2.4.4 Stillinger-Weber silicon

The quantum harmonic oscillator is a non-interacting system and, as such, does not make full use of our RPMD-LAMMPS code functionalities. A more stringent test of the code requires a system of particles interacting through a many-body potential. As a relevant test case here we consider a diamond-cubic crystal of silicon represented by the Stillinger-Weber interatomic potential [54]. Our choice is motivated by availability in the literature [53] of data for pressure as a function of per-atom volume previously computed for this very model system using path-integral Monte Carlo simulations (PIMC). First, to test convergence we computed the average energy and the average pressure as functions of the number of beads P in a 3D-periodic supercell containing 64 atoms of silicon arranged in a diamond cubic lattice at $T = 300\,\mathrm{K}$ which, except for the method, was precisely as in ref. 53 where the authors used 7 beads in their PIMC simulations. Figures 2.4 and 2.5 confirm that $P = 7$ is a reasonable choice for the number of beads in our RPMD simulations as well since both the energy and the pressure are reasonably converged at this number of beads.

In fig. 2.6 our RPMD simulation results for pressure as a function of per-atom volume are compared to corresponding data from PIMC simulations reported in ref. 53. Clearly, our RPMD predictions are in full agreement with the PIMC simulations. The same plot also shows pressure-versus-volume data from classical MD simulations performed under the same thermodynamic conditions. The major effect of zero-point vibrations on pressure seems to be a constant shift upward from the classical MD predictions which is equivalent to an added quantum pressure largely independent of the density.

To assess whether this shift in pressure is due solely to the ZPE, we take the energy difference between the classical and the quantum system and convert it, by equipartition of energy, into an increase in the kinetic energy raising the temperature from 300 K to 390 K. Classical MD simulations performed at this elevated temperature, fig. 2.7, suggest that ZPE accounts for most but not all of the added quantum pressure and perhaps other quantum effects beyond ZPE play a role.

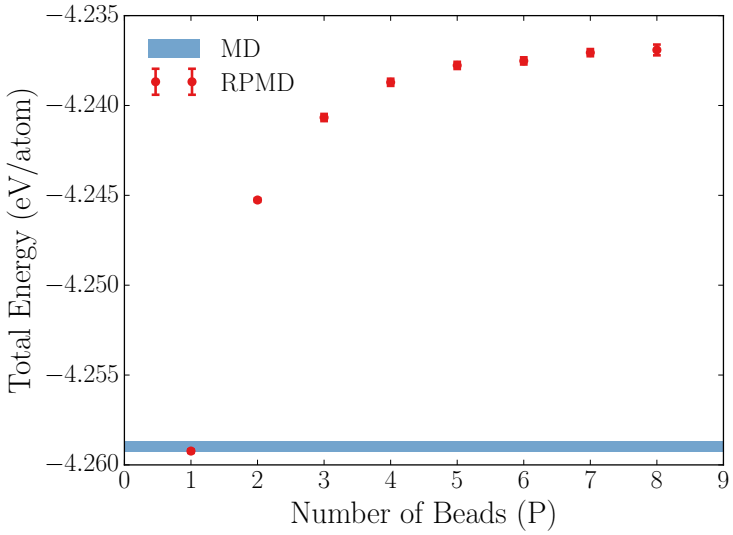

Figure 2.4: Average per-atom energy in the Stillinger-Weber model of diamond-cubic silicon computed in RPMD simulations as a function of the number of beads.

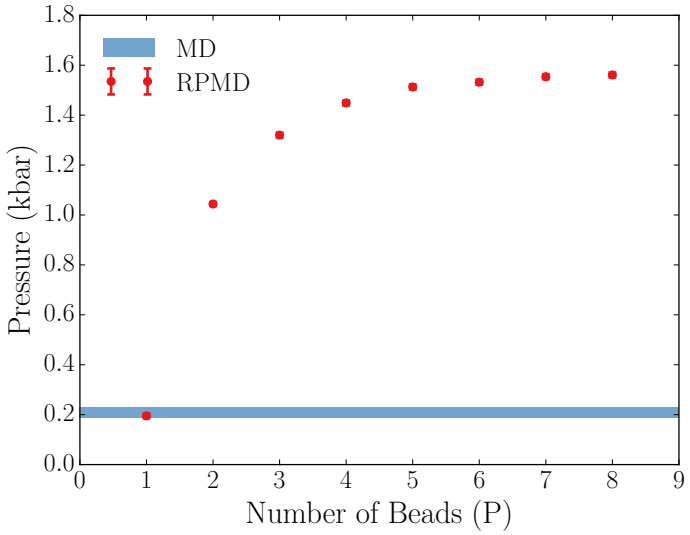

Figure 2.5: Average pressure in the Stillinger-Weber model of diamond-cubic silicon computed in RPMD simulations as a function of the number of beads.

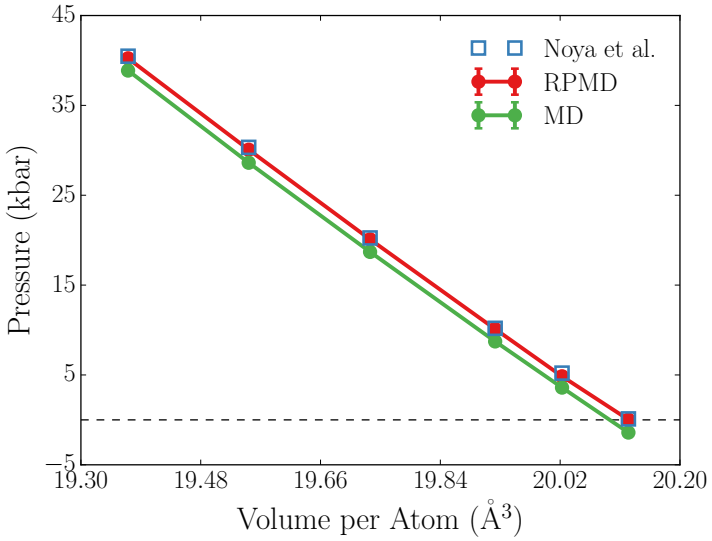

Figure 2.6: Pressure computed for the same Stillinger-Weber model of diamond-cubic silicon as a function of per-atom volume using quantum (RPMD and PIMC) and classical MD simulations. PIMC results were obtained by Noya, Herrero, and Ramírez in ref. 53.

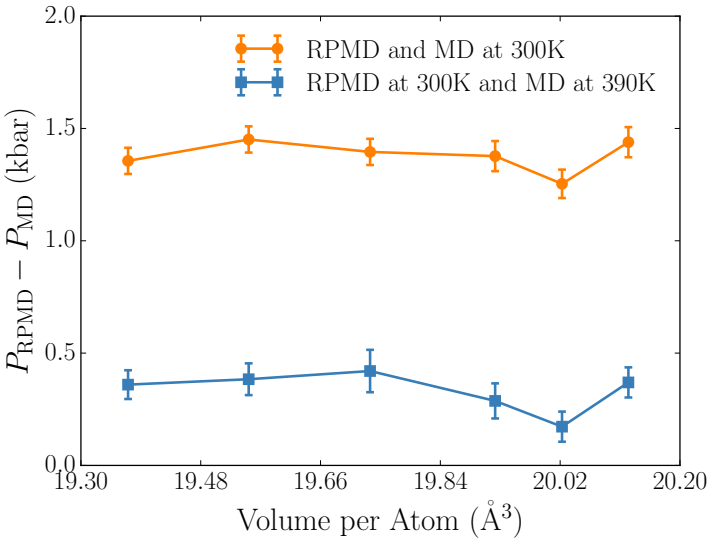

Figure 2.7: Added pressure due to quantum motion of atoms computed for the Stillinger-Weber model of diamond-cubic silicon: the red symbols and the red line are RPMD results minus classical MD predictions for pressure obtained at the same per-atom volumes; blue symbols and blue line is an approximate added pressure due to the ZPE (see text for details).

Chapter 3:

Step free energies at faceted solid surfaces

3.1 Motivation and overview

In theories of crystal morphologies and growth kinetics, a property of fundamental importance is the step free energy, γ^{st}, i.e., the excess free energy of a step line defect on a faceted solid-liquid interface or crystal surface [3, 4]. The magnitude of γ^{st} controls the depth of the cusp in the interfacial free energy versus orientation plot for faceted interfaces, and this property is thus fundamental in determining the equilibrium crystal shape [56]. The step free energy also plays an important role in governing crystallization kinetics from the melt or vapor [57], by controlling the magnitude of the barrier to island nucleation in the growth of a faceted surface or interface. The step free energy can depend strongly on temperature, and this dependence ultimately leads to the vanishing of γ^{st} above the thermodynamic roughening temperature [58, 59]. Below the roughening transition, steps with free energies that are low relative to the thermal energy will display pronounced capillary fluctuations, which have important consequences for their kinetic properties, bunching instabilities [60], and morphologies [61, 62].

Despite the importance of γ^{st} described above, measurements of this quantity remain relatively rare. Further, reported values are often available only for a fixed value of the temperature [63–66] and measurements over a wide temperature range have been undertaken in few systems [67, 68]. As a consequence, knowledge of the nature of the temperature dependence of step free energies and understanding of the microscopic factors that underlie it remain incomplete. This situation presents a challenge for the development and application of quantitative mesoscale theories in studies of faceted crystal growth phenomena in real systems, and robust methods for the direct calculation of temperature-dependent step free energies from atomic-scale simulations are thus of fundamental interest. In the present chapter we present a thermodynamic formalism that relates the temperature dependence of γ^{st} on faceted crystal surfaces to excess quantities that can be computed directly by atomistic simulations. This formalism provides a framework for the calculation of γ^{st} as a function of temperature through the thermodynamic integration of an appropriate adsorption equation.

The remainder of this chapter is organized as follows. In sec. 3.2 the thermodynamic formalism is introduced, and the relevant step excess quantities and other fundamental ther-

The results presented in this chapter and in appendix A have been published as a regular article with title "*Step free energies at faceted solid surfaces: Theory and atomistic calculations for steps on the Cu(111) surface*" in Physical Review B **95**, 155444 (2017) by Rodrigo Freitas, Timofey Frolov, and Mark Asta [55]. The material is presented here with the permission of co-authors and publishers.

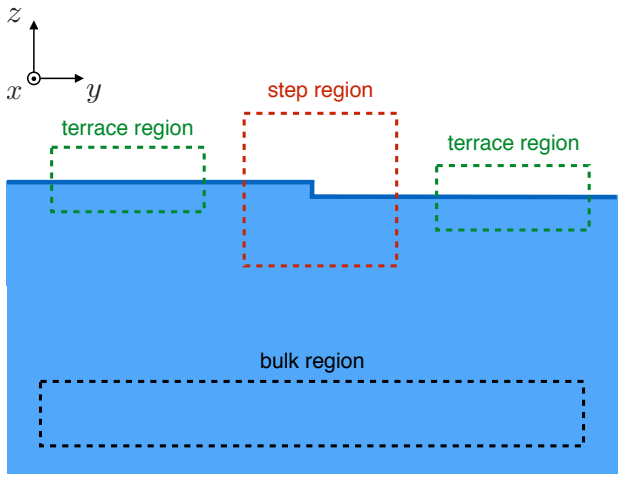

Figure 3.1: Schematic illustration of a thermodynamic system consisting of a homogeneous solid and a stepped surface. The solid is infinite along the $\pm\hat{\mathbf{x}}$, $\pm\hat{\mathbf{y}}$, and $-\hat{\mathbf{z}}$ directions. The surface normal is $\hat{\mathbf{z}}$ and the average step direction is along $\hat{\mathbf{x}}$.

modynamic equations are defined. In sec. 3.3 we demonstrate how the thermodynamic formalism can be combined with the calculation of a reference step free energy at low temperatures by the Frenkel-Ladd method [69, 70], to compute γ^{st} up to high temperatures, accounting for contributions arising from the formation of surface point defects and capillary fluctuations. In secs. 3.4 and 3.5 we present simulation details and results, respectively, of an application of the equations derived to the calculation of the free energy of $\langle 110 \rangle$ steps present on the $\{111\}$ surface of face-centered-cubic copper using molecular dynamics simulations. In sec. 3.5 we also compare the step free energy obtained here to experimentally measured [65] and first-principles-calculated [71–73] results available in the literature. Finally, in sec. 3.6 we summarize the main findings, and discuss applications of the formalism presented in this work more generally.

3.2 Thermodynamic theory of surface steps

3.2.1 Step excess quantities

Consider a thermodynamic system that consists of a homogeneous solid with a stepped surface, where the step separates two flat surface terraces as shown in fig. 3.1. Both terraces have the same structure and thermodynamic properties, while the surface around the step has properties that are different from those of the flat terraces. The step region, terraces, and bulk are in thermodynamic equilibrium with each other. We assume that atoms can migrate by diffusion between the bulk and the surface regions, allowing the concentration of point defects to vary everywhere in the system, in a way required to maintain equilibrium. We also assume that atoms can attach and detach from the step, so the system is in equilibrium with an infinite source and sink of atoms.

The properties of the bulk far away from the surface region and the properties of the flat terraces far away from the step region are well described by standard bulk and interfacial thermodynamic relations [74, 75]. In this section we will address the thermodynamic properties of the steps on the crystalline surface. Consider an imaginary region that contains a finite segment of the step, as shown in fig. 3.1. The lower boundary of this region is located inside the homogeneous part of the bulk crystal, while the side boundaries parallel and perpendicular to the step line cross the system surface normal to the terraces. The latter condition is important because it defines the total surface area inside the region.

The extensive thermodynamic properties of the step region depend on its dimensions, since the enclosed system is not homogeneous. We postulate that the total energy of the region is a function of the following extensive and intensive variables:

$$E^{\mathrm{st}} \equiv E^{\mathrm{st}}(S^{\mathrm{st}}, N^{\mathrm{st}}, A^{\mathrm{st}}, L, \varepsilon_{ij}). \tag{3.1}$$

The superscript "st" refers to variables of the step region shown in fig. 3.1: S^{st} is the entropy, N^{st} is the number of atoms, A^{st} is the surface area enclosed by the region, L is the step length, and ε_{ij} are the lateral components of strain, with $i = x, y$ and $j = x, y$. The lateral components of strain in eq. (3.1) correspond to the macroscopic strain in the homogeneous bulk lattice far away from the step, not to be confused with the local inhomogeneous strain around the step. As illustrated in fig. 3.1, the coordinate system is chosen such that $\hat{\mathbf{z}}$ is normal to the terraces, while $\hat{\mathbf{x}}$ and $\hat{\mathbf{y}}$ are parallel and normal to the step line, respectively.

Consider a variation when the physical state of the system is fixed and we extend the boundaries of the region from zero to some finite values. Assuming that E^{st} is a homogeneous function of degree one with respect to S^{st}, N^{st}, A^{st}, and L we obtain

$$E^{\mathrm{st}} = TS^{\mathrm{st}} + \mu N^{\mathrm{st}} + \gamma A^{\mathrm{st}} + \gamma^{\mathrm{st}} L, \tag{3.2}$$

where T is the temperature, μ is the chemical potential, γ is the surface free energy per unit area, and γ^{st} is the step free energy per unit step length. Note that by definition γ is the property of the terrace uninfluenced by the surface step. We assume that the external pressure is zero since the solid is in contact with vacuum.

At this point a comment should be made about the meaning of the quantities introduced above. The current thermodynamic treatment is focused on steps on solid surfaces, and it is well known that such steps produce long-range elastic fields [76, 77, 5]. As a result, both terraces and the bulk crystal are strictly speaking inhomogeneous in the entire system. Equation (3.2) can still be used to describe the system if γ and γ^{st} are understood as the properties of the terraces and the step in the limit when the system size goes to infinity. In other words, even though the inhomogeneity due to the strain fields induced by the step can extend far away from the step line, its total contribution to the energy of the system is finite. This will be demonstrated using atomistic simulations in sec. 3.4 of this study. This property of surface steps should be contrasted with the case of lattice dislocations, which are also line defects. Different from steps, the elastic contribution to the total energy of a dislocation diverges with the system size [9] and eq. (3.2) would not apply.

The amount of bulk and terrace inside the step region at this point is arbitrary, and hence quantities in eq. (3.2) depend on the choice of the step region. In order to define the step

excess quantities we need to subtract the bulk and terrace contributions from the quantities of the step region in fig. 3.1. To this end we write equations analogous to eq. (3.2) for the terrace and bulk regions shown in fig. 3.1:

$$E^{\mathrm{t}} = TS^{\mathrm{t}} + \mu N^{\mathrm{t}} + \gamma A^{\mathrm{t}} \tag{3.3}$$

$$E^{\mathrm{b}} = TS^{\mathrm{b}} + \mu N^{\mathrm{b}}, \tag{3.4}$$

where superscripts "t" and "b" refer to terrace and bulk respectively. These two regions are located sufficiently far away from the step that their extensive properties are not affected by it. The terrace region includes the surface as well as a portion of the homogeneous bulk phase, while the bulk region is unaffected by the surface. Solving the system of equations given by eqs. (3.2), (3.3), and (3.4) using Cramer's rule, we obtain an expression for step free energy γ^{st}:

$$\gamma^{\mathrm{st}} L = [E - TS - \mu N - \gamma A]_{XY} \tag{3.5}$$

where X and Y are any of the extensive quantities S, N or A. Terms $[Z]_{XY}$ are Cahn's determinants and are calculated as the ratio of two determinants [75]

$$[Z]_{XY} = \frac{\begin{vmatrix} Z^{\mathrm{st}} & X^{\mathrm{st}} & Y^{\mathrm{st}} \\ Z^{\mathrm{t}} & X^{\mathrm{t}} & Y^{\mathrm{t}} \\ Z^{\mathrm{b}} & X^{\mathrm{b}} & Y^{\mathrm{b}} \end{vmatrix}}{\begin{vmatrix} X^{\mathrm{t}} & Y^{\mathrm{t}} \\ X^{\mathrm{b}} & Y^{\mathrm{b}} \end{vmatrix}}. \tag{3.6}$$

The first row of the numerator contains extensive thermodynamic quantities of the region containing the step, while the second and the third rows contain properties of regions enclosing the terrace and the bulk, respectively. According to properties of determinants if any two columns are equal, the determinant is zero:

$$[X]_{XY} = [Y]_{XY} = 0. \tag{3.7}$$

Thus, two terms in eq. (3.5) automatically vanish.

The quantity $[Z]_{XY}$ has the meaning of the excess property of a step when the region with the step has the same amount of X and Y as the terrace and the bulk regions combined. The excess quantities generally depend on the choice of the extensive variables X and Y. On the other hand, eq. (3.5) shows that all different choices of X and Y result in the same excess amount of $\gamma^{\mathrm{st}} L$.

Considering a particular example when $X = A$ and $Y = N$, we obtain

$$\gamma^{\mathrm{st}} L = [E]_{AN} - T[S]_{AN}. \tag{3.8}$$

The step excess quantities $[E]_{AN}$ and $[S]_{AN}$ are the excess energy and entropy when the step region has the same surface area and number of atoms as terrace and bulk regions combined. The choice of A as one of the extensive variables means that the excess area of a step is

zero. The step is represented as a dividing line on the surface and the properties of terraces are extended all the way to this line. Using this representation, step excess quantities can be formulated in a manner similar to the Gibbs dividing surface construction for interfaces. On the other hand, the derivation that uses Cahn's determinants provides expressions for excess quantities that are more general. The ability to choose different definitions can be useful in applications because some excess quantities are more accessible than others to measurements or calculations. In sec. 3.4 we describe how several step excess quantities can be calculated directly from atomistic simulations by making use of the flexibility provided by Cahn's determinants.

3.2.2 Adsorption equation

In the previous section we derived an expression for the step free energy and other excess quantities. We are now in a position to derive an equation that describes how γ^{st} changes with temperature and mechanical deformation, namely the adsorption equation. Consider a variation of state when the system exchanges heat and does mechanical work. For the region containing the step the change in total energy is given by

$$\mathrm{d}E^{\mathrm{st}} = T\,\mathrm{d}S^{\mathrm{st}} + \mu\,\mathrm{d}N^{\mathrm{st}} + \sum_{i,j}^{x,y} \sigma_{ij}^{\mathrm{st}} V^{\mathrm{st}}\,\mathrm{d}\varepsilon_{ij}, \tag{3.9}$$

where $\sigma_{ij}^{\mathrm{st}}$ is the stress tensor and V^{st} is the volume. The product $\sigma_{ij}^{\mathrm{st}} V^{\mathrm{st}}$ is defined as the derivative of E^{st} with respect to elastic deformation ε_{ij}. Equation (3.9) assumes that the surface area changes due to elastic deformation of the lattice and not by incorporation of new lattice units. At the same time the number of atoms in the region and the relative areas of the terraces can change by diffusion and attachment of atoms to the step. The conditions for mechanical equilibrium between the system and the vacuum [78, 5] require that $\sigma_{iz}^{\mathrm{st}} = 0$ for $i = x$, y, or z. Thus, all summations involving the stress tensor are over the x and y indices only.

Performing a Legendre transformation on terms containing entropy and number of particles we obtain from eq. (3.9)

$$\begin{aligned}\mathrm{d}(E^{\mathrm{st}} - TS^{\mathrm{st}} - \mu N^{\mathrm{st}}) = -S^{\mathrm{st}}\,\mathrm{d}T - N^{\mathrm{st}}\,\mathrm{d}\mu \\ + \sum_{i,j}^{x,y} \sigma_{ij}^{\mathrm{st}} V^{\mathrm{st}}\,\mathrm{d}\varepsilon_{ij}.\end{aligned} \tag{3.10}$$

Combining eqs. (3.2) and (3.10) we obtain

$$\begin{aligned}\mathrm{d}(\gamma^{\mathrm{st}} L) = -S^{\mathrm{st}}\,\mathrm{d}T - N^{\mathrm{st}}\,\mathrm{d}\mu \\ - A^{\mathrm{st}}\,\mathrm{d}\gamma + \sum_{i,j}^{x,y} (\sigma_{ij}^{\mathrm{st}} V^{\mathrm{st}} - \delta_{ij}\gamma A^{\mathrm{st}})\,\mathrm{d}\varepsilon_{ij}.\end{aligned} \tag{3.11}$$

The intensive variables on the right-hand side in eq. (3.11) are not independent since equations similar to eq. (3.11) for the terrace and bulk regions impose additional constrains. For

the terrace we have [79]

$$0 = -S^{\mathrm{t}}\,\mathrm{d}T - N^{\mathrm{t}}\,\mathrm{d}\mu - A^{\mathrm{t}}\,\mathrm{d}\gamma + \sum_{i,j}^{x,y}(\sigma_{ij}^{\mathrm{t}}V^{\mathrm{t}} - \delta_{ij}\gamma A^{\mathrm{t}})\,\mathrm{d}\varepsilon_{ij}, \tag{3.12}$$

while the Gibbs-Duhem equation for the bulk reads

$$0 = -S^{\mathrm{b}}\,\mathrm{d}T - N^{\mathrm{b}}\,\mathrm{d}\mu + \sum_{i,j}^{x,y}\sigma_{ij}^{\mathrm{b}}V^{\mathrm{b}}\,\mathrm{d}\varepsilon_{ij}. \tag{3.13}$$

Solving eqs. (3.11), (3.12), and (3.13) using Cramer's rule [75], we obtain the adsorption equation for steps

$$\mathrm{d}(\gamma^{\mathrm{st}}L) = -[S]_{XY}\,\mathrm{d}T - [N]_{XY}\,\mathrm{d}\mu - [A]_{XY}\,\mathrm{d}\gamma + \sum_{i,j}^{x,y}\left[\sigma_{ij}V - \delta_{ij}\gamma A\right]_{XY}\mathrm{d}\varepsilon_{ij}, \tag{3.14}$$

where X and Y are any of the extensive quantities S, N, A, or $(\sigma_{ij}V - \delta_{ij}\gamma A)$. Notice that the coefficients of the differentials in eq. (3.14) are the step excess quantities introduced earlier in eq. (3.6), and are independent of the particular choice of the regions illustrated in fig. 3.1. Due to the property of determinants in eq. (3.7), two terms in the adsorption equation can be eliminated by specifying X and Y, leaving only independent variables. The number of variables should coincide with the number of degrees of freedom available to the system. Consider the same example given in sec. 3.2.1, where we choose X and Y equal to A and N. In this case the four possible variations are changes in temperature and deformation described by strains ε_{xx}, ε_{yy}, and ε_{xy}. It is natural to have the step free energy be a function of these variables. The differential of surface free energy γ that appears in eq. (3.14) is an unusual variable to describe the changes in the thermodynamic state of the step. While such an exotic form of the adsorption equation can be formulated and is consistent with the Gibbs phase rule, in most practical cases it is more convenient to eliminate this term by specifying $X = A$.

3.2.3 Step stress

Equation (3.14) introduces a new excess property in addition to the quantities that appeared in eq. (3.5). The last term in eq. (3.14) describes changes in $\gamma^{\mathrm{st}}L$ due to elastic deformations and defines the step excess stress as

$$[\tau_{ij}]_{XY} \equiv \frac{1}{L}\frac{\partial\left(\gamma^{\mathrm{st}}L\right)}{\partial\varepsilon_{ij}} = \frac{1}{L}\left[\sigma_{ij}V - \delta_{ij}\gamma A\right]_{XY}, \tag{3.15}$$

where $i = x, y$ and $j = x, y$. $[\tau_{ij}]_{XY}$ is a quantity with units of energy per length that represents the additional force exerted on the perimeter of the stepped surface due to the presence of the step. Different from γ^{st}, the step excess stress $[\tau_{ij}]_{XY}$ is not a unique quantity:

it is a direct consequence of the derived adsorption equation that one can introduce several valid step excess stresses by specifying different extensive properties X and Y. Notice that by the derivation above $[\boldsymbol{\tau}]$ is a second rank tensor, not a scalar like step free energy; hence it has nonzero components parallel and normal to the step line [80].

Differentiating the product $\gamma^{\mathrm{st}}L$ in eq. (3.14) and using $\mathrm{d}L = \sum_{i,j}^{x,y} \delta_{ix}\delta_{jx} L\,\mathrm{d}\varepsilon_{ij}$ we obtain the intensive form of the adsorption equation:

$$\begin{aligned}\mathrm{d}\gamma^{\mathrm{st}} = &-\frac{[S]_{XY}}{L}\,\mathrm{d}T - \frac{[N]_{XY}}{L}\,\mathrm{d}\mu \\ &-\frac{[A]_{XY}}{L}\,\mathrm{d}\gamma + \sum_{i,j}^{x,y}([\tau_{ij}]_{XY} - \delta_{ix}\delta_{jx}\gamma^{\mathrm{st}})\,\mathrm{d}\varepsilon_{ij},\end{aligned} \tag{3.16}$$

where the differential coefficients are the step excess quantities per unit step length. From eq. (3.16) we can now obtain the relation between $[\tau_{ij}]_{XY}$ and γ^{st}:

$$[\tau_{ij}]_{XY} = \delta_{ix}\delta_{jx}\gamma^{\mathrm{st}} + \frac{\partial\gamma^{\mathrm{st}}}{\partial\varepsilon_{ij}}. \tag{3.17}$$

Equations (3.15) and (3.17) are the step analogs of the stress equations for solid surfaces [81, 79, 82]. They are a direct consequence of the derived adsorption equation, eq. (3.14), and give a recipe for how $[\tau_{ij}]_{XY}$ can be calculated as an excess property using the determinant formalism.

Consider the example discussed earlier (secs. 3.2.1 and 3.2.2) when $X = A$ and $Y = N$. This choice of extensive variables eliminates differentials of chemical potential μ and surface free energy γ, leaving only independent variations with temperature and deformation:

$$\mathrm{d}\gamma^{\mathrm{st}} = -\frac{[S]_{AN}}{L}\,\mathrm{d}T + \sum_{i,j}^{x,y}([\tau_{ij}]_{AN} - \delta_{ix}\delta_{jx}\gamma^{\mathrm{st}})\,\mathrm{d}\varepsilon_{ij}. \tag{3.18}$$

The second term in eq. (3.18) describes how the step free energy changes when the surface is deformed at constant temperature. Notice that during such a process the chemical potential μ and free energy of the terraces γ are not constant. Equation (3.18) defines a particular step excess stress given by

$$[\tau_{ij}]_{AN} = \frac{1}{L}\,[\sigma_{ij}V]_{AN}\,. \tag{3.19}$$

The components of this stress tensor have been calculated in the present work from atomistic simulations, and the magnitudes of this quantity will be presented in sec. 3.5 below.

3.3 Thermodynamic integration formalism

In this section we describe how the equations derived in sec. 3.2 provide a framework for a thermodynamic-integration approach to computing the temperature dependence of the step free energy γ^{st} by atomistic simulations. We also demonstrate how the absolute free energy of the step can be derived at low temperatures (i.e., where the concentration of kinks and surface adatoms are sufficiently low that we can neglect their contribution to

the free energy) using the Frenkel-Ladd [69] method, to provide a reference value in the thermodynamic integration approach. The combination of these two methods provides a general framework for the calculation of step free energies over a wide temperature range, accounting naturally for vibrational and configurational disorder.

3.3.1 Gibbs-Helmholtz relation for step free-energy integration

The temperature dependence of the step free energy can be obtained by directly integrating $\mathrm{d}(\gamma^{\mathrm{st}}L)$, given in eq. (3.14), along a reversible thermodynamic trajectory. However, in many applications the calculation of the excess entropy $[S]_{XY}$ can be challenging. Fortunately, we can avoid the explicit calculation of $[S]_{XY}$ by integrating $\mathrm{d}(\gamma^{\mathrm{st}}L/T)$ instead of eq. (3.14). We can compute $\mathrm{d}(\gamma^{\mathrm{st}}L/T)$ explicitly by combining eq. (3.5) and (3.14):

$$\begin{aligned}\mathrm{d}\left(\frac{\gamma^{\mathrm{st}}L}{T}\right) = &-\frac{[E-\mu N-\gamma A]_{XY}}{T^2}\,\mathrm{d}T - \frac{[N]_{XY}}{T}\,\mathrm{d}\mu \\ &- \frac{[A]_{XY}}{T}\,\mathrm{d}\gamma + \sum_{i,j}^{x,y}\frac{[\tau_{ij}]_{XY}L}{T}\,\mathrm{d}\varepsilon_{ij},\end{aligned} \tag{3.20}$$

where $[\tau_{ij}]_{XY}$ depends on the choice of the X and Y variables. Equation (3.20) is the surface step analog of the Gibbs-Helmholtz equation from bulk thermodynamics. A similar equation for interfaces was derived previously [83], and was demonstrated to be efficient for calculating the temperature dependence of interface free energies [79, 83–87].

Before integrating eq. (3.20) we need to choose X and Y since the selection of these variables determines which quantities need to be calculated to perform the thermodynamic integration. A convenient choice for the applications considered here is $X = A$ and $Y = N$. In this case eq. (3.20) becomes

$$\mathrm{d}\left(\frac{\gamma^{\mathrm{st}}L}{T}\right) = -\left(\frac{[E]_{AN}}{T^2} - \sum_{i,j}^{x,y}\frac{[\tau_{ij}]_{AN}L}{T}\frac{\mathrm{d}\varepsilon_{ij}}{\mathrm{d}T}\right)\mathrm{d}T, \tag{3.21}$$

where $[\tau_{ij}]_{AN}$ is given by eq. (3.19). Equation (3.21) can be integrated along a reversible thermodynamic path, where the temperature is increased from T_0 to T while the solid is expanded to accommodate the thermal expansion, effectively maintaining zero bulk stress, i.e., $\boldsymbol{\sigma}^{\mathrm{b}} = 0$. Notice that this thermodynamic path couples the *a priori* independent variables T and ε:

$$\alpha_{ij} \equiv \left(\frac{\partial\varepsilon_{ij}}{\partial T}\right)_{\boldsymbol{\sigma}^{\mathrm{b}}=0}$$

where α_{ij} is the linear thermal-expansion factor and i and j are equal to $x, y,$ or z. We will assume here that the crystal lattice has cubic symmetry, allowing us to define our coordinate system in a way that eliminates the dependence of α_{ij} on the indexes i and j. One further implication of following this thermodynamic path is that the system is not subject to shear strain during the thermal expansion; hence $[\tau_{ij}]_{AN}$ for $i \neq j$ performs no mechanical work. With these considerations eq. (3.21) becomes

$$\mathrm{d}\left(\frac{\gamma^{\mathrm{st}}L}{T}\right) = -\left(\frac{[E]_{AN}}{T^2} - \frac{2\alpha\,[\tau_{\mathrm{avg}}]_{AN}L}{T}\right)\mathrm{d}T \tag{3.22}$$

where

$$[\tau_{\text{avg}}]_{AN} = \frac{[\tau_{xx}]_{AN} + [\tau_{yy}]_{AN}}{2} \tag{3.23}$$

is the average step stress. Upon integration of eq. (3.22) following the thermodynamic path described above we obtain

$$\begin{aligned}\gamma^{\text{st}}(T) =& \frac{T}{T_0}\frac{\gamma^{\text{st}}(T_0)\,L(T_0)}{L(T)} \\ &- \frac{T}{L(T)}\int_{T_0}^{T}\left(\frac{[E]_{AN}}{T'^2} - \frac{2\alpha\,[\tau_{\text{avg}}]_{AN}L}{T'}\right)\mathrm{d}T'.\end{aligned} \tag{3.24}$$

Note that all quantities inside the integral depend on the temperature T'.

Equation (3.24) allows for the calculation of the temperature dependence of γ^{st} if we know how to calculate all quantities on its right-hand side. The excess quantities inside the integral on the right-hand side of eq. (3.24), $[E]_{AN}$ and $[\tau_{\text{avg}}]_{AN}$, can be computed readily from atomistic simulations since they only involve the calculation of the system energy and stress tensor. Thus, the only remaining term on the right-hand side of eq. (3.24) is the step excess free energy at a reference temperature $\gamma^{\text{st}}(T_0)$. This type of term, present in all thermodynamic integration methods, cannot be trivially computed using atomistic simulations, since it involves the calculation of the absolute free energy of the system. In the next section we present a method due to Frenkel and Ladd [69, 70] which enables the calculation of the absolute free energy of solid systems. In the present context, this method enables the calculation of $\gamma^{\text{st}}(T_0)$ provided the temperature T_0 is chosen low enough such that the steps are structurally ordered (i.e., without an appreciable concentration of kinks, adatoms, or vacancies). Once we know the free energy of the step at this reference temperature, we can use eq. (3.24) to compute the absolute free energy of the step at any other temperature T from values of $[E]_{AN}$ and $[\tau_{\text{avg}}]_{AN}$ at temperatures between T_0 and T.

3.3.2 Application of Frenkel-Ladd approach for calculation of step free energies

The Frenkel-Ladd [69] (FL) method is a type of thermodynamic integration approach that allows calculation of the absolute free energy of crystalline solids from atomistic simulations. Consider a system composed of N identical particles with the Hamiltonian

$$H_0 = \sum_{i=1}^{N}\frac{\mathbf{p}_i^2}{2m} + U(\mathbf{r}_1, \mathbf{r}_2, ..., \mathbf{r}_N) \tag{3.25}$$

where m is the mass of the particles and $U(\mathbf{r}_1, \mathbf{r}_2, ..., \mathbf{r}_N)$ is a many-body interatomic potential. We assume that, at the temperature and pressure of interest, the system's stable phase is a solid with a known crystalline lattice structure. Considering this lattice structure we will construct a second Hamiltonian for a reference Einstein crystal, which consists of particles of the same mass m attached to the equilibrium lattice sites by harmonic springs with spring constant k:

$$H_{\text{E}} = \sum_{i=1}^{N}\frac{\mathbf{p}_i^2}{2m} + \sum_{i=1}^{N}\frac{1}{2}k\left(\mathbf{r}_i - \mathbf{r}_i^0\right)^2 \tag{3.26}$$

where $\mathbf{r}_i^0$ is the equilibrium lattice position of particle i in the system described by H_0.

In the FL method we use a Hamiltonian which is a linear interpolation of the Hamiltonians given by eqs. (3.25) and (3.26):

$$H(\lambda) = (1-\lambda)H_0 + \lambda H_{\mathrm{E}}, \tag{3.27}$$

where λ is a parameter of this Hamiltonian. The free energy of the system $H(\lambda)$ is

$$F(N,V,T;\lambda) = -k_{\mathrm{B}}T \ln\left\{\int \frac{\mathrm{d}\mathbf{x}}{h^{3N}} \exp\left[-\beta H(\lambda)\right]\right\} \tag{3.28}$$

where k_{B} is the Boltzmann constant, h is the Planck constant, $\mathbf{x} = \{\mathbf{r}_1, \mathbf{r}_2, ..., \mathbf{r}_N, \mathbf{p}_1, \mathbf{p}_2, ..., \mathbf{p}_N\}$ is a point in the phase space of the particles of this system, and $\beta = 1/k_{\mathrm{B}}T$. It can be easily shown, by computing the derivative of eq. (3.28), that

$$\frac{\partial F}{\partial \lambda} = \left\langle \frac{\partial H}{\partial \lambda} \right\rangle_{\lambda}$$

where $\langle \ldots \rangle_\lambda$ is the canonical ensemble average for a specific value of the parameter λ. From direct integration of the equation above from $\lambda = 0$ to $\lambda = 1$ we obtain

$$F_0(N,V,T) = F_{\mathrm{E}}(N,V,T) + \int_0^1 \langle U - U_{\mathrm{E}} \rangle_\lambda \, \mathrm{d}\lambda \tag{3.29}$$

where $F_0(N,V,T) \equiv F(N,V,T;\lambda = 0)$ is the free energy of the solid described by H_0, $F_{\mathrm{E}}(N,V,T) \equiv F(N,V,T;\lambda = 1)$ is the free energy of the Einstein crystal, and U_{E} is the potential energy of the harmonic springs in the Einstein crystal. Since H_{E} is composed of independent harmonic oscillators we can calculate its free energy analytically:

$$F_{\mathrm{E}}(N,V,T) = 3Nk_{\mathrm{B}}T \ln\left(\frac{\hbar\omega}{k_{\mathrm{B}}T}\right), \tag{3.30}$$

where $\omega = \sqrt{k/m}$ is the natural frequency of the harmonic oscillators.

Equations (3.29) and (3.30) allow calculation of the absolute free energy of the solid H_0 from atomistic simulations. The only unknown in eq. (3.29) is the integrand on the right-hand side, which is an equilibrium ensemble average and, therefore, can be calculated directly using atomistic simulation techniques [30] such as molecular dynamics or Monte Carlo with the Hamiltonian given by eq. (3.27). The evaluation of eq. (3.29) can be performed in a straightforward manner using equilibrium simulations to obtain averages necessary to calculate the integral on the right-hand side numerically. However, this is an inefficient way to perform this thermodynamic integration. State-of-the-art methods [70] for evaluating eq. (3.29) based on nonequilibrium simulations have been developed and are now implemented in high-performance atomistic simulation software such as LAMMPS [29] (Large-scale Atomic/Molecular Massively Parallel Simulator). These methods drastically reduce the computational cost of the thermodynamic-integration calculation and provide robust error-control criteria. An in-depth description of these techniques and detailed account of how they can be implemented in practice is given in ref. 70.

We have shown in sec. 3.2, eqs. (3.5) and (3.8), that the step free energy $\gamma^{\rm st}(T_0)$ is a quantity that can be computed from the free energies of the three different regions shown in fig. 3.1. Hence, our approach in the work presented below is to obtain the $\gamma^{\rm st}(T_0)$ using the FL method to compute the absolute free energies of the relevant required systems. In so doing we have followed closely the methodology described in ref. 70 to perform the FL calculations. Note, however, that the FL method has its applicability limited to low-temperature surfaces (flat and stepped), since at high temperatures the presence of surface vacancies, adatoms, and kinks on the steps breaks the FL method assumption that the atomic motion occurs around the equilibrium lattice positions, eq. (3.26). Thus, the free energy computed with the FL method is only used as an initial integration point for the thermodynamic integral approach of sec. 3.3.1, more specifically in eq. (3.24).

3.4 Atomistic simulations

3.4.1 Methodology

To demonstrate the application of the methodology described in the previous section, for computing step free energies by atomistic simulations, we focus on the (111) surface of face-centered-cubic Cu, modeled with the embedded-atom-method (EAM) interatomic potential due to Mishin et al. [88]. In previous simulations it has been found that this surface remains faceted at all temperatures up to the melting point of the EAM model ($T_{\rm m} = 1327\,{\rm K}$ for the potential model considered [89]). No evidence for surface premelting was observed in these previous simulations, such that the surface maintains the layered crystalline structure up to $T_{\rm m}$. Since the surface remains faceted, the step free energies are expected to remain finite up to this temperature.

We have chosen molecular dynamics (MD) as the atomistic simulation technique to evaluate the step excess quantities necessary for the thermodynamic integration equations. All calculations were performed using LAMMPS [29], an open source implementation of MD. The Langevin thermostat [90] was employed to sample the phase space, according to the canonical ensemble distribution. The relaxation time used for the thermostat was $\tau_{\rm L} \equiv m/\gamma = 20{\rm ps}$, where γ is the friction parameter and m is the atomic mass. The timestep was chosen based on the highest-frequency normal mode of the system ($\nu_{\rm max} = 7.8 \times 10^{12}$ Hz); we have taken Δt to be approximately 1/60th of the oscillation period of that normal mode: $\Delta t = 2\,{\rm fs}$.

3.4.2 System geometry and dimensions

In sec. 3.3 eq. (3.24) was derived for the temperature dependence of $\gamma^{\rm st}$, based on the choice $X = A$ and $Y = N$. In this sub-section we elaborate further why this is a convenient choice for the calculation of the excess quantities that appear in eq. (3.24) from atomistic

simulations. From eq. (3.6) we have

$$[Z]_{AN} = \frac{\begin{vmatrix} Z^{\mathrm{st}} & A^{\mathrm{st}} & N^{\mathrm{st}} \\ Z^{\mathrm{t}} & A^{\mathrm{t}} & N^{\mathrm{t}} \\ Z^{\mathrm{b}} & A^{\mathrm{b}} & N^{\mathrm{b}} \end{vmatrix}}{\begin{vmatrix} A^{\mathrm{t}} & N^{\mathrm{t}} \\ A^{\mathrm{b}} & N^{\mathrm{b}} \end{vmatrix}}. \tag{3.31}$$

The bulk region in fig. 3.1 does not have any surface which means $A^{\mathrm{b}} = 0$. Heretofore the regions shown in fig. 3.1 had arbitrary dimensions; from now on we choose the dimensions of the step and terrace regions in such a way that they have the same surface area, i.e., $A^{\mathrm{st}} = A^{\mathrm{t}}$. Furthermore, we choose the depth of these regions such that they contain the same number of atoms: $N^{\mathrm{st}} = N^{\mathrm{t}}$. With this particular choice of dimensions, the excess quantities shown in eq. (3.31) become $[Z]_{AN} = Z^{\mathrm{st}} - Z^{\mathrm{t}}$. Thus, the need to compute the thermodynamic properties for the bulk (Z^{b}) is eliminated and $[Z]_{AN}$ becomes a simple difference between the properties of the step and terrace regions.

To calculate step excess quantities we modeled two different simulation blocks illustrated in fig. 3.2. The simulation block shown in fig. 3.2a is a solid film with two flat (111) surfaces. Periodic boundary conditions were applied for the directions parallel to the surface. The second simulation block illustrated in fig. 3.2b was obtained from the first one by adding half of an atomic plane on the top surface and removing half of the atomic plane from the bottom surface. As a result of this construction, the second block has four surface steps. At the same time the construction ensures that the two simulation blocks have the same number of atoms and the same surface area. Properties Z^{st} and Z^{t} were then calculated for the two blocks with and without steps, respectively. The difference between these quantities gives the step excess $[Z]_{AN}$ given by eq. (3.31). Indeed, $Z^{\mathrm{st}} - Z^{\mathrm{t}}$ represents the excess of property Z due to steps, when the reference system has the same surface area and the same number of atoms. We remind the reader that the excess quantities inside the integral on the right-hand side of eq. (3.24) are $[E]_{AN} = E^{\mathrm{st}} - E^{\mathrm{t}}$ and $[\tau_{ii}]_{AN} = (\sigma_{ii}^{\mathrm{st}} V^{\mathrm{st}} - \sigma_{ii}^{\mathrm{t}} V^{\mathrm{t}})/L$ and can be readily computed from atomistic simulations since they involve only the calculation of the energy and stress tensor of each of the systems in fig. 3.2.

The steps considered in the MD simulations of the simulation cells illustrated by fig. 3.2b are directed along the close-packed $\langle 110 \rangle$ direction. The crystallographic symmetry of the (111) surface is such that the two steps shown in each of the surfaces of fig. 3.2b are slightly different; it can be seen in fig. 3.3 that they have different nearest-neighbor configurations on the (111) plane immediately below the surface. The step with lowest zero-temperature energy [5] ($U_0 = 103.13\,\mathrm{meV/\,\AA}$) is a $\langle 110 \rangle$A step, while the step with the slightly larger energy ($U_0 = 104.08\,\mathrm{meV/\,\AA}$) is a $\langle 110 \rangle$B step. Using the terminology of ref. 71 $\langle 110 \rangle$A steps have $\langle 100 \rangle$ microfacets and $\langle 110 \rangle$B steps have $\langle 111 \rangle$ microfacets.

We have chosen the simulation box size in such a way that the step-step interaction energy of all four steps in fig. 3.2b was negligible compared to the step self-energy (i.e., the energy of an isolated step). Steps are abrupt interruptions of the surface first layer; hence,

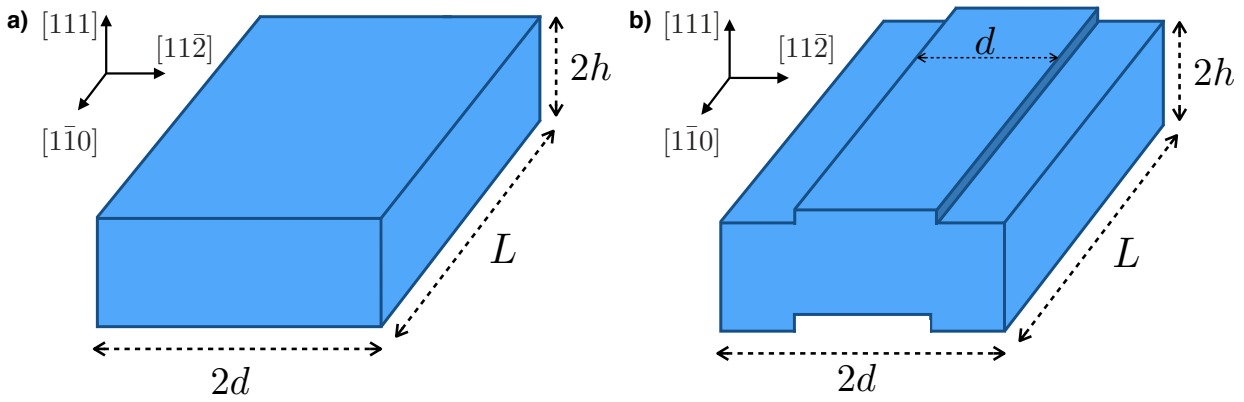

Figure 3.2: Simulation box geometry for (a) the system with a flat terrace and (b) the system containing steps. d denotes the lateral step separation distance, h the bulk depth, and L the step length. The step line is parallel to the $[1\bar{1}0]$ direction and on the (111) surface plane. The step separation, d, is measured along the $[11\bar{2}]$ direction, perpendicular to the step line direction. Periodic boundary conditions are applied along the $[1\bar{1}0]$ and $[11\bar{2}]$ directions, within the surface plane. The systems illustrated in (a) and (b) are constructed such that they contain the same number of atoms and have the same total surface area.

they deform the atomic structure around them, creating an elastic field [76]. The interaction energy due to the overlap of the strain fields of the two steps decays as d^{-2} with the step-step separation and exponentially with the bulk depth (see ref. 77 and references therein). Following the work of Shilkrot and Srolovitz [77] we have verified this behavior for the step elastic interaction energy [2] of our model and we have determined the step-step distance (d) and bulk depth (h) such that $E_{\text{int}}/U_0 \leq 10^{-4}$, where E_{int} is the total step interaction energy and U_0 is the step self-energy at zero temperature. The box dimensions obtained are $d = 70.8\,\text{Å}$ and $h = 53.2\,\text{Å}$ at $T = 0\,\text{K}$; for finite temperatures we have increased the system dimensions to account for thermal expansion, for zero bulk stress.

The simulation box length along the step line cannot be determined based on static simulations. In order to determine the step length necessary to eliminate finite-size effects along the step direction it is necessary to consider fluctuations of the step line that appear at finite temperatures, known as capillary fluctuations. The accurate evaluation of step excess quantities requires satisfactorily sampling the normal modes of these fluctuations (i.e., the capillary waves) during the simulation. If the step length used is too small the sampling of long-wavelength modes is suppressed. On the other hand, an excessively lengthy step would make the thermodynamic integration calculations prohibitively long due to the need to sample normal modes with very long wavelengths and associated long relaxation times.

[2] If these interactions are appreciable we would expect a significant difference between results obtained from supercells with symmetric (as shown in fig. 3.2) versus antisymmetric indentations on the top and bottom surfaces. But if the crystal slab is thick enough to minimize step interactions the differences would be negligible. We performed a separate independent test of the effect of system size, by comparing the step self energy derived from supercells with the geometry shown in fig. 3.2, with results obtained using non-orthogonal boundary conditions [77] where there is only one step on each surface. The values for the step self energy agreed for both geometries to within 0.01%.

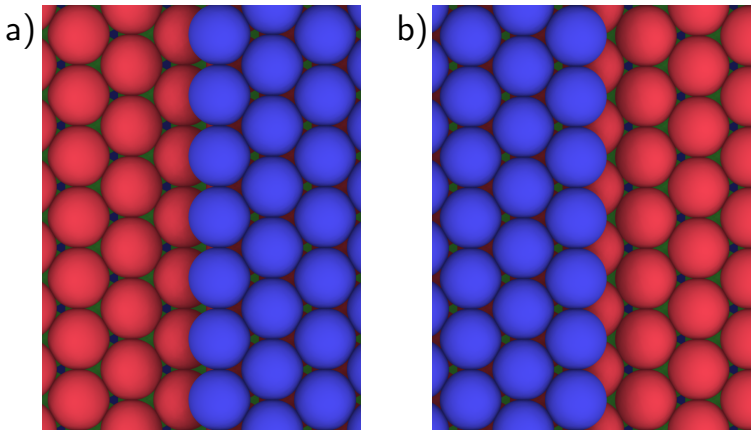

Figure 3.3: Atomic configuration of (a) ⟨110⟩A and (b) ⟨110⟩B steps on the (111) surface of an fcc lattice. Atoms are colored according to the atomic layer they belong to: blue atoms belong to the first layer, red atoms to the second layer, and yellow atoms to the third layer. Atoms at the edge of the two different ⟨110⟩A and ⟨110⟩B steps have different nearest-neighbor configurations on the (111) plane immediately below the surface.

Thus, to determine the step length required in the simulations we need to analyze the convergence of $[E]_{AN}$ and $[\tau_{\mathrm{avg}}]_{AN}$ with the step length since, according to eq. (3.24), the thermodynamic integration equation depends on the computation of these two quantities.

Using the values of d and h determined above we have run simulations at $T = 1300\,\mathrm{K}$ for systems with different step lengths (L) and calculated the step excess energy and stress. Figure 3.4 shows the convergence of the step excess quantities with step length for these simulations. Based on these results we have chosen $L = 30.7\,\text{Å}$ as the step length for the next simulations since the step excess quantities are seen to be well converged for steps of this size.

3.5 Results and discussion

3.5.1 Step free energies from Frenkel-Ladd simulations

Using the box dimensions specified in sec. 3.4.2, we have constructed two systems to be used in the FL simulations, one with a flat surface and the another with stepped surfaces, as shown in figs. 3.2a and b. Both systems have 39168 atoms and the same surface area. In fig. 3.5 we show plan-view snapshots [91] of the top layer of atoms from typical configurations for the stepped system at different temperatures. At temperatures of 700 K or lower, the step line is mostly straight with small fluctuations due to atomic vibrations, while as we raise the temperature closer to the melting point ($T_{\mathrm{m}} = 1327\,\mathrm{K}$) configurational disorder due to capillary fluctuations and the formation of vacancies and adatoms becomes pronounced. The presence of appreciable configurational disorder limits the application of the FL method to temperatures below 700 K. The formation of defects above this temperature causes a sharp increase in the dissipation during the switching to the Einstein crystal. This excessive

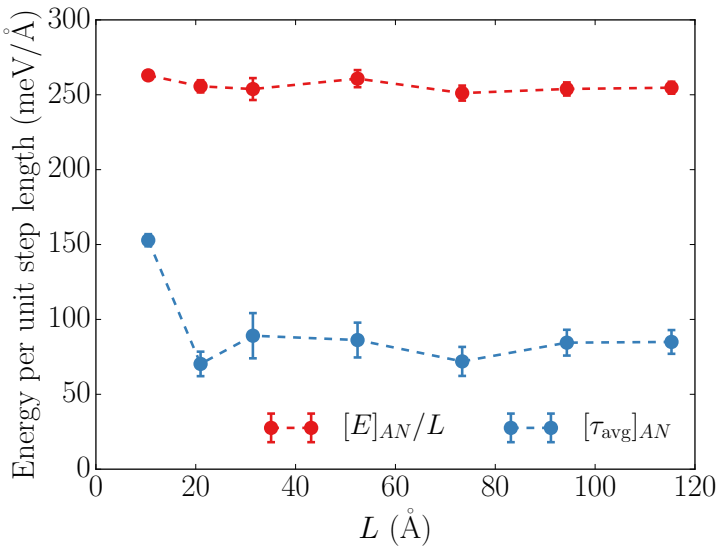

Figure 3.4: Convergence of step excess energy ($[E]_{AN}$) and average step excess stress ($[\tau_{\mathrm{avg}}]_{AN}$) with step length ($L$) at $T = 1300\,\mathrm{K}$. Error bars are the standard error of the mean, computed by taking into consideration the relaxation times of the capillary wave normal modes.

dissipation is characteristic of irreversible processes and violates the assumptions necessary for the derivation of the FL method equations, namely, the reversibility of the integration path and that the atomic motion occurs around average positions given by the equilibrium lattice positions.

The FL method was applied to both systems in fig. 3.2 according to the nonequilibrium techniques presented in ref. 70. We have employed a switching time of $t_{\mathrm{s}} = 4\,\mathrm{ns}$ and the S-shaped [70, 92] functional form for the $\lambda(t)$ parameter. The simulations were carried out at temperatures ranging from 100 K to 700 K in intervals of 100 K. Estimates for the statistical errors were obtained by performing three independent switching simulations (forward and backward) for each temperature.

Based on the discussion in sec. 3.4.2, the step excess free energy was calculated from the difference of the free energy of the two systems in fig. 3.2: $\gamma^{\mathrm{st}} = (F^{\mathrm{st}} - F^{\mathrm{t}})/L$, where L is the total length of the four steps in fig. 3.2b. Since the surfaces in the system illustrated in fig. 3.2b contain both $\langle 110\rangle$A and $\langle 110\rangle$B types of steps, the FL method provides the average of the free energy of both of these step types. The results of the FL simulations are shown as the red and green dots in fig. 3.6. Note that the error bars are smaller than the points on the plot. The standard error of the mean of the points in fig. 3.6 is $\approx 1\,\mathrm{meV/\,\AA}$, which requires the calculation of the free energy per atom for each system, which is achieved with an accuracy of $\approx 3\,\mu\mathrm{eV/atom}$. Such high statistical accuracy is achievable due to the high efficiency and accuracy of the nonequilibrium Frenkel-Ladd method used in this work. Further details about the technique as well as an in-depth analysis of error control and estimation are provided in ref. 70.

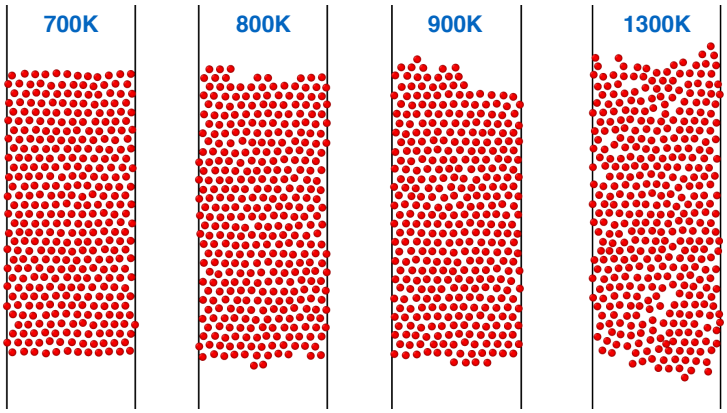

Figure 3.5: Plan view of two steps on the (111) surface, showing only atoms on the top step layer. Variations in the step position due to capillary fluctuations become larger as we raise the temperature and approach the melting point.

3.5.2 Step excess quantities

The step excess quantities were calculated for systems with the same size and number of atoms as the systems used for the FL calculations. From the MD simulations we obtained the average energy of the systems with the step E^{st} and the flat terrace E^{t}, and also the components of stress tensor $\boldsymbol{\sigma}^{\mathrm{st}}$ and $\boldsymbol{\sigma}^{\mathrm{t}}$. The step excess properties $[E]_{AN}$ and $[\tau_{\mathrm{avg}}]_{AN}$ were then computed by taking the difference between the quantities of the stepped system and the flat-terrace system, as described in sec. 3.4.2. The MD simulations were performed for temperatures ranging from 100 to 1300 K, in intervals of 100 K. Additionally, we also performed one simulation at the melting temperature for the potential $T_{\mathrm{m}} = 1327\,\mathrm{K}$. The systems were equilibrated for 6 ns before calculating the values of E^{st}, E^{t}, $\boldsymbol{\sigma}^{\mathrm{st}}$, and $\boldsymbol{\sigma}^{\mathrm{t}}$. After equilibration, these values were sampled at intervals of 2 ps for 400 ns at each temperature. Figure 3.7 shows the temperature dependence of $[E]_{AN}$ and $[\tau_{\mathrm{avg}}]_{AN}$. The error bars correspond to the standard error of the mean for each data point, obtained through a block average analysis of the data collected for each temperature. Note that the error bars of $[E]_{AN}$ are too small to appear on the plot.

The results for $[E]_{AN}$ in fig. 3.7 show that the excess energy increases with temperature from $(103.61 \pm 0.02)\,\mathrm{meV/\AA}$ at $T = 0\,\mathrm{K}$ to $(302 \pm 4)\,\mathrm{meV/\AA}$ at T_{m}. Within a large temperature interval, from zero to approximately 800 K (i.e., a homologous temperature of approximately 0.60), the value of $[E]_{AN}$ remains essentially constant, and then begins to increase much more rapidly as the melting temperature is approached. The simulations show that $[E]_{AN}$ remains finite, and does not diverge as the melting point is approached.

The results for excess stress in fig. 3.7 show that $[\boldsymbol{\tau}]_{AN}$ is appreciably anisotropic at low T: the step stress component perpendicular to the step, $[\tau_{\perp}]_{AN}$, is compressive at low temperatures while $[\tau_{\parallel}]_{AN}$ is tensile. Although they are similar in magnitude we notice that they have measurably different values at 0 K: $[\tau_{\perp}]_{AN} = -38.3\,\mathrm{meV/\AA}$ and $[\tau_{\parallel}]_{AN} = 34.3\,\mathrm{meV/\AA}$. Both parallel and perpendicular components increase with temperature, but the perpendicular does so faster, the consequence being that the anisotropy becomes reduced at high temperatures, where both components become compressive. Notice also that the excess av-

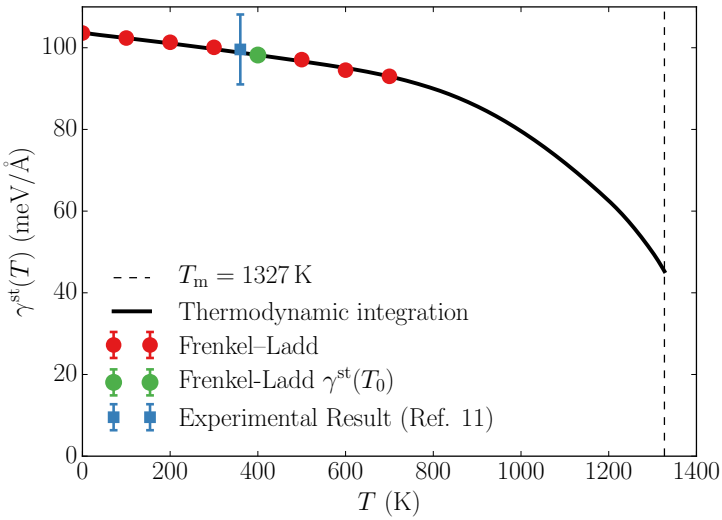

Figure 3.6: Temperature dependence of the calculated average of ⟨110⟩A and ⟨110⟩B step free energies on the (111) surface of elemental Cu. The black solid line was calculated from the step excess quantities using the thermodynamic integration method described in sec. 3.3.1. The initial point for the integration $\gamma^{st}(T_0)$ was obtained using the Frenkel-Ladd method at $T_0 = 400\,K$. Extra calculations using the Frenkel-Ladd method were performed for $T \neq T_0$; they are shown as red dots in the figure and are in excellent agreement with the independent thermodynamic integration results. Also included in the figure is an experimental measurement of the step free energy at $T = 360\,K$, taken from ref. 65, which is seen to be very close in magnitude to the computed value at this temperature.

erage stress, $[\tau_{avg}]_{AN}$, remains almost constant for low temperatures, before the onset of large capillary fluctuations of the step. As for $[E]_{AN}$, only for temperatures above approximately 800 K is a significant temperature dependence of the step excess stress observed.

3.5.3 Step free energies from thermodynamic integration calculations

In this subsection we focus on the temperature-dependent step free energies, obtained by the thermodynamic-integration (TI) approach described in sec. 3.3.1. The results obtained from this approach are shown as the solid line in fig. 3.6, which plots the value of γ^{st} over the entire temperature range from $T = 0\,K$ up to T_m. In performing the TI calculations, we have chosen $T_0 = 400\,K$ as the reference point for the thermodynamic integration, and the integration was performed in both directions, from T_0 to T_m and from T_0 to $\approx 0\,K$. As noted above, the TI values for γ^{st} agree well with those from the FL method that were not used in the integration (red points in fig. 3.6), demonstrating the consistency of the predictions for the temperature dependence of γ^{st} at low homologous temperatures obtained from these two independent methods. We present in the Appendix a discussion of the numerical convergence of the TI results, including error calculations and the independence of the final results on the choice of the reference temperature T_0.

Overall, the TI results in fig. 3.6 show that the temperature dependence of γ^{st} is large

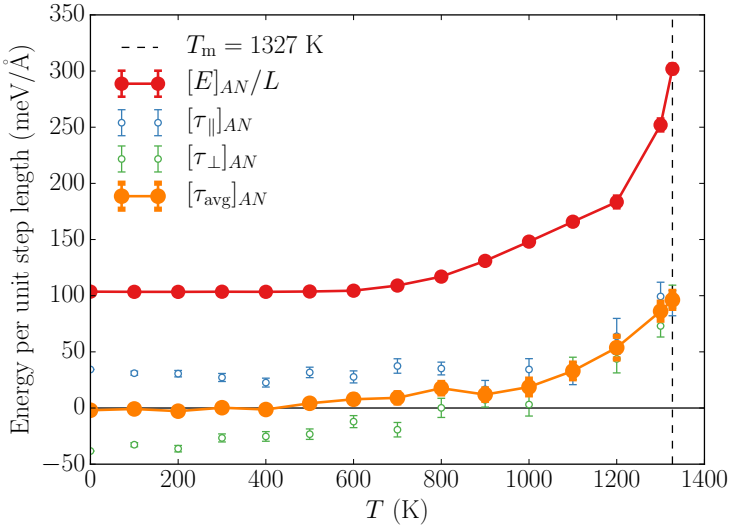

Figure 3.7: Temperature dependence of step excess energy $[E]_{AN}$ and step excess stress $[\tau_{\text{avg}}]_{AN}$. $[\tau_{\text{avg}}]_{AN}$ is the average of the step stresses parallel ($[\tau_{\parallel}]_{AN}$) and perpendicular ($[\tau_{\perp}]_{AN}$) to the step line. Notice how the stress perpendicular to the step line changes from tensile to compressive as the temperature increases. Error bars corresponding to the standard error of the mean were obtained for all data points, although they are smaller than the symbols employed for some of the data points.

and highly nonlinear over the full temperature range. Although the magnitude of γ^{st} remains finite at the melting point, indicating that the surface remains faceted up to T_{m}, the net effect of increasing temperature is a sizable decrease of γ^{st}. Specifically, increasing the temperature up to melting leads to a decrease in magnitude of γ^{st} by more than half, from a value of $(103.61 \pm 0.02)\,\text{meV}/\,\text{Å}$ at $T = 0\,\text{K}$ to $(45.8 \pm 0.4)\,\text{meV}/\,\text{Å}$ at $T = T_{\text{m}}$.

Considering the temperature dependence of γ^{st} in further detail, we divide the results into two temperature ranges: low homologous temperature up to 800 K (i.e., from homologous temperatures of zero to approximately 0.60), and high homologous temperatures from 800 K up to the melting point. In the first temperature range, the excess quantities presented in the previous section are approximately constant in value, and γ^{st} displays a relatively weak rate of decrease with temperature. Over this temperature range the value of γ^{st} decreases approximately linearly, by roughly 13% percent, from a value of $(103.61 \pm 0.02)\,\text{meV}/\,\text{Å}$ to $(90.3 \pm 0.2)\,\text{meV}/\,\text{Å}$. Since the steps are observed to remain straight on the simulation length and time scales (i.e.., no evidence of appreciable kinks, adatoms, or surface vacancies is observed) for temperatures up to 800 K, we interpret the temperature dependence of γ^{st} over this temperature range to arise primarily from atomic vibrational contributions to the step excess thermodynamic quantities.

Above $T = 800\,\text{K}$, γ^{st} displays a much more pronounced temperature dependence. From 800 K up to T_{m} the value of γ^{st} decreases by roughly 51% percent, from a value of $(90.3 \pm 0.2)\,\text{meV}/\,\text{Å}$ to $(45.8 \pm 0.4)\,\text{meV}/\,\text{Å}$. In this temperature range, the concentration of surface adatoms and vacancies increases significantly, and the magnitudes of the step capillary fluctuations become more pronounced. The larger temperature dependence of γ^{st}

over this temperature range is thus interpreted to be a manifestation of the effect of such configurational disorder on the step excess thermodynamic quantities.

3.5.4 Comparison with previous measured and calculated results

Although we are not aware of previous results presenting the temperature dependence of step free energies in Cu all the way up to the melting point, there have been measurements and previously published calculations at low temperatures for this system, to which the present simulation results can be compared.

The step free energy of Cu(111) [110]A and B steps at selected temperatures has been obtained experimentally from the analysis of adatom and vacancy islands observed using scanning tunneling microscopy [63, 67, 64, 65]. For a comprehensive comparison of two available methods for computing γ^{st} experimentally, we refer the reader to ref. 65, where Steimer *et al.* report $\gamma^{\mathrm{st}} = 256 \pm 22\,\mathrm{meV/a}$ for an average of A and B steps, where a is the atomic distance along the [110] direction and the measurement is for an average temperature of $\overline{T} = 360\,\mathrm{K}$ ($T \in [280, 440]\,\mathrm{K}$). The present results are remarkably close to this value, as indicated in fig. 3.6: we obtain values of $\gamma^{\mathrm{st}} = 254.8 \pm 0.2\,\mathrm{meV/a}$ for the same temperature. Moreover, the temperature dependence of γ^{st} shown in fig. 3.6 is consistent with the analysis in ref. 65, suggesting that the step free energy has a weak temperature dependence for the temperature range at which the experiments were conducted.

This good agreement between the present simulation results and experimental measurements is achieved despite the approximations inherent in the classical description of the interatomic interactions by an EAM potential model. Importantly, a similar level of agreement is also obtained by the EAM model and available *ab initio* values at zero temperature obtained by density functional theory (DFT). Specifically, the value of the step energy given by the EAM potential considered in this work is $\gamma^{\mathrm{st}} = 264.8\,\mathrm{meV/a}$ at $T = 0\,\mathrm{K}$, which agrees well with the DFT result of $\gamma^{\mathrm{st}} = 270\,\mathrm{meV/a}$ reported in refs. 71–73. The fact that the current results agree well with DFT at zero temperature, and with experiment at finite temperatures, suggests that the latter agreement is not a result of cancellation of errors resulting from inaccurate energetics and temperature dependencies. Rather the EAM model for Cu of Mishin *et al.* [88] employed in this work appears to yield accurate values for γ^{st} and its temperature dependence, at least at low homologous temperatures.

3.6 Summary and conclusions

We present a thermodynamic formalism for steps on faceted surfaces of single-component crystalline solids, resulting in the derivation of a general adsorption equation, eq. (3.14), relating changes in step free energy (γ^{st}) to variations in chemical potential, surface free energy, temperature, and strain. The rate of change of γ^{st} with respect to variations in these variables is related to surface excess quantities of particle number, surface area, entropy, and stress, respectively. Due to the existence of Gibbs-Duhem relations for the bulk and surface, which give rise to constraints on the variations of the intensive variables, Cramer's rule can be used to express the adsorption equation in terms of a particular choice for the set of independent variables. The approach results in the definition of step excess quantities

formulated in terms of determinants, following the formalism first introduced in the context of interfacial thermodynamics by Cahn [75]. A direct result of the formulation developed in the present work is the definition of a step excess stress, eq. (3.17), which is the step analog of the familiar surface stress quantity, and which represents the excess force on the perimeter of a stepped surface due to the presence of a step. Although the formalism presented in this work is developed only for the special case of single-component crystalline surfaces, the underlying approach is more general, and can be extended to multicomponent/multiphase situations, as demonstrated recently by Frolov and Mishin [93].

The thermodynamic formalism presented in this work is demonstrated to provide a convenient framework for thermodynamic-integration calculations of the temperature dependence of γ^{st} by atomistic simulations. For this purpose, it is natural to employ a particular choice for the set of independent intensive variables that leads to the definition of step excess quantities, in a manner that is similar to choosing a Gibbs [94] dividing surface leading to zero excess volume and particle number. By combining the resulting expression for the adsorption equation with the Gibbs-Helmholtz relation, we derive an expression for the temperature dependence of the step free energy, eq. (3.22), in terms of step excess energy and excess stress quantities that can be readily calculated in atomistic simulations. It is straightforward to extend the proposed TI approach to steps at faceted solid-liquid interfaces, grain boundaries and phase boundaries in multicomponent systems [93]. This approach can provide full temperature and composition dependence of step free energy from atomistic simulations, provided that a reference free energy value is known at some temperature and composition. In the present work we have demonstrated how the Frenkel-Ladd method can be employed for this purpose, when the interfaces of interest involve only solid phases. For solid-liquid or solid-vapor interfaces alternative approaches would be needed such as those based on nucleation simulations (e.g., ref. 95) or analyses of capillary fluctuations (e.g., refs. 96, 97).

We demonstrate the application of the thermodynamic integration formalism for the case of $\langle 110 \rangle$ steps on faceted $\{111\}$ surfaces of element Cu, employing MD simulations based on a classical EAM potential due to Mishin *et al.* [88]. By combining the thermodynamic-integration formalism with the the Frenkel-Ladd method for computing a reference value of γ^{st} at low temperatures, where the step structure remains highly ordered, we present a calculation of the step free energy over the entire temperature range from zero up to the melting point.

In the process of performing the thermodynamic-integration calculations, we compute temperature-dependent values for the step excess energies and stresses, as shown in fig. 3.7. The excess energy is found to display a weak temperature dependence up to a homologous temperature of approximately 0.60; beyond this temperature the excess energy increases strongly as the step displays growing configurational disorder due to the formation of surface adatoms and vacancies and appreciable capillary fluctuations. For the step excess stress, we have obtained negative $[\tau_{\perp}]_{AN}$ and positive $[\tau_{\parallel}]_{AN}$ at low homologous temperatures, with both terms having similar magnitudes. With increasing temperature, the low-temperature anisotropy of the step stress is greatly reduced, and at high temperatures $[\tau_{\perp}]_{AN}$ becomes positive. Therefore, thermal effects such as thermal expansion, vibrational fluctuations, and configurational disordering affect each step stress component differently. It is worth noting that this behavior is not unique to step stresses; it has been observed before in atomistic

simulations [98, 99] that the surface stress for solid-liquid interfaces also presents positive and negative values, depending on the system properties and thermodynamic conditions.

For the temperature dependence of the calculated step free energy, our findings are shown in fig. 3.6 and can be summarized as follows. At low homologous temperatures (i.e., less than approximately 0.6), where the thermal effects are interpreted to be associated primarily with atomic vibrations, γ_{st} is calculated to display a relatively weak temperature dependence. At these low temperatures, the calculated magnitudes of γ^{st} show good agreement with previously reported experimental measurements and DFT calculations, indicating the accuracy of the employed EAM potential for the present application. The calculated temperature dependence of γ^{st} increases strongly at higher homologous temperatures, as the step becomes increasingly configurationally disordered. The net effect is a reduction in the step free energy by more than half as the temperature is increased from zero up to the melting temperature. Such a strong temperature dependence at high homologous temperatures would be expected to have important consequences for kinetic processes such as surface island nucleation and growth kinetics.

Chapter 4:

Capillary fluctuations of surface steps

4.1 Motivation and overview

Capillary fluctuations are a ubiquitous phenomenon at fluid interfaces, line defects, and crystalline interfaces that are atomically rough [101, 96, 97, 102–105]. These equilibrium fluctuations, which lead to variations in the line length of a linear defect, or area of a rough interface at finite temperature, have been widely studied by advanced experimental characterization techniques and computer simulations, as they provide insights into the thermodynamic and kinetic properties of the interfaces on which they form. While a detailed overview of such studies is beyond the scope of the present dissertation, we refer the reader to comprehensive reviews and representative experimental and computational studies [106, 56, 5, 107–109] in the context of steps at faceted crystalline interfaces, which provide the focus of the present work. The properties of such steps play a critical role in governing the kinetics of crystal growth from melt, solution, or vapor phases, due to their influence on the thermodynamics of island nucleation and the kinetics of interface migration (e.g., ref. 110).

Over the last decade analyses of capillary fluctuations in molecular-scale computer simulations, based on molecular dynamics (MD) or Monte Carlo (MC) methods, have been employed extensively within the so-called capillary-fluctuation method (CFM) approach to computing interfacial free energies and their associated crystalline anisotropies for crystal-melt interfaces, grain boundaries, and solid-solid heterophase interfaces (e.g., refs. 96, 111–114, 97, 115, 116). Recently, the CFM approach has been employed also for steps at faceted crystal-melt interfaces [117] to derive temperature-dependent step stiffnesses, which are relevant in the context of modeling solidification rates and associated crystal growth morphologies. For crystal-melt interfaces, liquid surfaces, and fluid-fluid interfaces, detailed comparisons of CFM results with those obtained using alternative thermodynamic-integration and nucleation based MD methods have been undertaken to understand the range of applicability and associated accuracies of these alternative approaches (e.g., refs. 118–124). At the present time we are unaware of such comparisons for the applications of the CFM for step properties.

In the present chapter we consider the application of the CFM approach for studying thermodynamic and kinetic properties of steps on crystalline surfaces, focusing on Cu(111) as a representative model metal system. The results of equilibrium MD simulations near

The results presented in this chapter have been published as a regular article with title "*Capillary fluctuations of surface steps: An atomistic simulation study for the model Cu(111) system*" in Physical Review E **96**, 043308 (2017) by Rodrigo Freitas, Timofey Frolov, and Mark Asta [100]. The material is presented here with the permission of co-authors and publishers.

the melting temperature of the potential model considered are analyzed to compute step fluctuation spectra, characterized by the wave number (k) dependence of the mean-square amplitudes $\langle|A(k)|^2\rangle$, as well as the fluctuation relaxation times $\tau(k)$. From the dependence of $\langle|A(k)|^2\rangle$ on k we derive step stiffnesses for $\langle 110\rangle$ and $\langle 112\rangle$ step orientations, obtaining values that are isotropic (independent of orientation) within the statistical precision of the simulations. Further, we obtain values of fluctuation lifetimes that are consistent with the k^{-4} scaling associated with dynamics that are governed by step-edge diffusion.

The focus on the Cu(111) system in the present chapter enables a comparison of CFM results with step free energies obtained in chapter 3 and published by the authors [55] using an alternative thermodynamic-integration (TI) approach. The values of the step stiffnesses derived by the CFM are lower by approximately 25% compared with the step free energies calculated by the TI approach for $\langle 110\rangle$ oriented steps at the same temperature. The discrepancy is discussed within the framework of statistical-mechanical theories of the configurational contributions to step free energies (e.g., refs. 125, 126) associated with capillary fluctuations.

The remainder of this chapter is organized as follows. In sec. 4.2 we present a brief derivation of the main results from capillary-wave theory that are used in the remainder of the chapter; although similar derivations appear already in many places in the literature, the overview is included to emphasize key concepts and equations required for the analysis and interpretation of the present MD results. In sec. 4.3 we describe the details of the MD simulations of step capillary fluctuations and in sec. 4.4 we present the simulation results. In sec. 4.5 a discussion is presented focusing on the comparison of the present CFM results to step free energies obtained previously by thermodynamic integration [55]. Finally, the results and conclusions are summarized in sec. 4.6.

4.2 Capillary-wave model

In this section we summarize the main equations required for CFM analysis of surface step fluctuations. We describe how the capillary-wave Hamiltonian results from the coarse-graining of the atomic partition function, and also highlight several nuances of the CFM that will be discussed in the context of the analysis of the MD simulation results in sec. 4.3.

4.2.1 Step effective Hamiltonian

Following the notation from ref. 55, the excess free energy of a step can be defined thermodynamically through the relation:

$$[F]_{AN} \equiv F^{\mathrm{st}} - F^{\mathrm{t}} = \gamma^{\mathrm{st}} L, \tag{4.1}$$

where γ^{st} is the step free energy per unit length and L is the system dimension along the average step direction, as illustrated in fig. 4.1. F^{st} and F^{t} are the absolute free energies of systems with the same surface area (A), number of atoms (N), and temperature (T). These systems can be considered to be identical except that the system corresponding to F^{t} has a flat surface, while the one corresponding to F^{st} contains a surface step of length L. The free energy of the system with a flat surface can also be written as $F^{\mathrm{t}} = -k_{\mathrm{B}}T \ln Q^{\mathrm{t}} + 3Nk_{\mathrm{B}}T \ln \Lambda$,

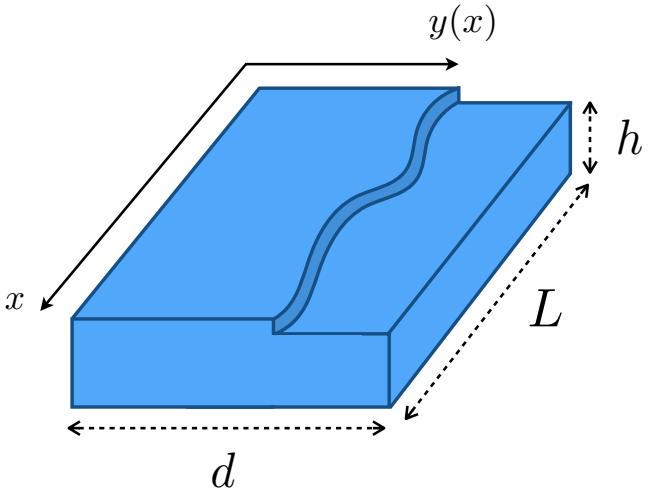

Figure 4.1: System dimensions and orientation: d is the step-step separation distance, L is the step length, and h is the bulk depth. The step average direction is along $\hat{\mathbf{x}}$, and the step line profile is given by the curve y(x). Periodic boundary conditions are applied on the x and y directions.

where $k_{\rm B}$ is the Boltzmann constant, $Q^{\rm t}$ is the configurational part of the system's partition function, and $\Lambda = (h^2/2\pi m k_{\rm B}T)^{1/2}$ is the thermal de Broglie wavelength. Similarly, the free energy of the system with a step is $F^{\rm st} = -k_{\rm B}T \ln Q^{\rm st} + 3Nk_{\rm B}T \ln \Lambda$. Hence, we can rewrite the step free energy in eq. (4.1) as follows:

$$[F]_{AN} = -k_{\rm B}T \ln Q, \tag{4.2}$$

where $Q \equiv Q^{\rm st}/Q^{\rm t}$ is the ratio of the configurational partition functions.

In order to clarify the physical meaning of Q consider the potential energy of the system with a step: $U^{\rm st}(\mathbf{x})$, where $\mathbf{x}$ is the $3N$-dimensional vector with the atomic coordinates. We can perform a canonical transformation on the atomic coordinates and separate the variables describing the step configuration from all other variables. With this transformation the potential energy can be written as $U^{\rm st} = U^{\rm st}(\mathbf{R}, \mathbf{r})$, where $\mathbf{R}$ are the step degrees of freedom and $\mathbf{r}$ represents all other degrees of freedom (i.e., bulk and surface degrees of freedom). With this set of generalized coordinates the configurational partition function of the system with the step can be written as

$$Q^{\rm st} = \int {\rm d}\mathbf{R} \, \exp\Big[-\beta U_{\rm cg}(\mathbf{R}) \Big], \tag{4.3}$$

where

$$U_{\rm cg}(\mathbf{R}) = -k_{\rm B}T \ln \left\{ \int {\rm d}\mathbf{r} \, \exp\Big[-\beta U^{\rm st}(\mathbf{R}, \mathbf{r}) \Big] \right\}, \tag{4.4}$$

is a coarse-grained potential energy which involves only the step degrees of freedom. Notice that, for convenience, we have performed the canonical transformation in such a way as to render $\mathbf{R}$ and $\mathbf{r}$ dimensionless quantities. Equation (4.4) implies that $U_{\rm cg}(\mathbf{R})$ is the portion of the free energy associated with the bulk and surface configurational degrees of freedom $\mathbf{r}$.

Alternatively, eq. (4.3) suggests that $U_{\rm cg}(\mathbf{R})$ can also be seen as the potential that generates the step dynamics on that system. Because of this last interpretation $U_{\rm cg}(\mathbf{R})$ is also known as the potential of mean force [36], i.e., it is the potential acting on the step that arises from the mean contribution of the bulk and surface degrees of freedom. In the limit of adiabatic decoupling between the step and the rest of the system $U_{\rm cg}(\mathbf{R})$ becomes an effective potential on which the step degrees of freedom ($\mathbf{R}$) can be assumed to evolve in time independently from the other degrees of freedom ($\mathbf{r}$).

The step free energy can be written as a function of the coarse-grained potential energy $U_{\rm cg}(\mathbf{R})$. First, we substitute eq. (4.3) in the equation for Q and use $Q^{\rm t} = \exp\left[-\beta(F^{\rm t} - 3Nk_{\rm B}T\ln\Lambda)\right]$:

$$Q = \frac{Q^{\rm st}}{Q^{\rm t}} = \int \mathrm{d}\mathbf{R}\, \exp\Big[-\beta\mathcal{H}(\mathbf{R})\Big],$$

where we have defined the step effective Hamiltonian $\mathcal{H}(\mathbf{R}) \equiv U_{\rm cg}(\mathbf{R}) - (F^{\rm t} - 3Nk_{\rm B}T\ln\Lambda)$. Now the step free energy can be obtained from eqs. (4.1) and (4.2):

$$\gamma^{\rm st}L = -k_{\rm B}T\ln\left\{\int \mathrm{d}\mathbf{R}\, \exp\big[-\beta\mathcal{H}(\mathbf{R})\big]\right\}. \tag{4.5}$$

Notice that eq. (4.5) does not involve any approximation, we have only separated and interpreted specific parts of the partition function Q. Hence, the calculation of the step free energy $\gamma^{\rm st}$ using eq. (4.5) still involves an integral over the phase space of all particles.

4.2.2 Capillary-wave model for steps

It is now possible to introduce a model for the step effective Hamiltonian, $\mathcal{H}(\mathbf{R})$, that simplifies the calculation of eq. (4.5) but still includes all relevant physical properties that govern the step dynamics. A reasonable model that forms the basis for capillary-wave theory (e.g., ref. 125), is to assume that a fluctuation of the step line that causes a change $\delta\ell$ in step length has an energetic cost of $\sigma\delta\ell$, where σ is the step energy per unit length. With this physical picture the step effective Hamiltonian takes the form:

$$\mathcal{H}\left[y(x)\right] = \int_y \sigma(\theta)\ \mathrm{d}\ell = \int_0^L \sigma(\theta)\sqrt{1+y'(x)^2}\,\mathrm{d}x, \tag{4.6}$$

where $\theta(x) = \tan^{-1}(y/x)$ is the step orientation with respect to the average step-line direction and the integral is over the curve $y(x)$ describing the step-line profile, as illustrated in fig. 4.1. Thus, $\mathcal{H}$ is a functional of the step configuration $y(x)$ [127].

Notice that $\sigma(\theta)$ defined in eq. (4.6) is different from the step stress tensor $\boldsymbol{\tau}^{\rm st}$ as defined in, for example, refs. 55, 128. The step stress tensor couples mechanically to the system strain and gives origin to a elastic deformation energy which can be directly measured in atomistic simulations [55]. The physical interpretation of $\sigma(\theta)$ is more complicated, as discussed in detail in ref. 125. For example, $\sigma(\theta)$ reflects the energy per unit *physical length* of the step, while $\boldsymbol{\tau}^{\rm st}$ and $\gamma^{\rm st}$ are defined per unit length of the average step direction, indicated as L in fig. 4.1 and eq. (4.1). For our purpose in this chapter we will refer to $\sigma(\theta)$ as the step tension in the line-fluctuation model given by eq. (4.6).

To compute from eq. (4.6) the equilibrium spectrum for the capillary fluctuations, and the resulting free energy, the traditional approach [114, 125, 127] is to make use of the small slope approximation where $\theta(x) \approx y'(x)$ and the terms inside the integral in eq. (4.6) can be expanded in powers of $y'(x)$. Collecting the terms with the same power and keeping only terms $O(y'^2)$ allow us to write the step effective Hamiltonian as

$$\mathcal{H}[y(x)] = \sigma L + \frac{1}{2}\tilde{\sigma}\int_0^L y'(x)^2\,\mathrm{d}x, \tag{4.7}$$

where $\sigma \equiv \sigma(0)$ is the step tension of the state with a straight step in this model, and $\tilde{\sigma} \equiv \sigma(0) + \sigma''(0)$ is the step stiffness, where $\sigma''(0)$ denotes the second derivative of the step tension with respect to the orientation of the step normal evaluated in the state where the step is straight. The term σL in eq. (4.7) is the energy of a straight step, while the second term is the energy penalty in having any curvature along the step line, i.e., the energy cost of step fluctuations.

The next step is to discretize the integral in eq. (4.7) into a Riemann sum, resulting in a Hamiltonian that is quadratic in $y(x_n)$, with $x_n = n\Delta x$ where $n = 0, 1, \ldots, M-1$ and $\Delta x = L/M$. In what follows we adopt a similar approach based on a Fourier representation of the step profile. This formulation, while equivalent, leads to expressions more aligned with the CFM analysis of computer simulation results.

The step line profile $y(x)$ shown in fig. 4.1 can be decomposed in normal modes as:

$$y(x) = \sum_{n=-(M-1)/2}^{(M-1)/2} A_n \exp\left(ik_n x\right), \tag{4.8}$$

where the wavevectors k_n are given by $k_n = n(2\pi/L)$ with $n = 0, \pm1, \pm2, ..., \pm(M-1)/2$ (assuming M is odd). Using eq. (4.8) we can compute the integral in eq. (4.7) and obtain:

$$\mathcal{H}(\{A_n\}) = \sigma L + \tilde{\sigma} L \sum_{n=1}^{(M-1)/2} k_n^2 \left|A_n\right|^2, \tag{4.9}$$

where we have made use of the fact that $A_n^* = A_{-n}$ since $y(x)$ is real. In this system of coordinates the amplitudes A_n of the normal modes are the step degrees of freedom since they define the step configuration $y(x)$ through eq. (4.8). The step effective Hamiltonian given by eq. (4.9) is quadratic in all its degrees of freedom and thus many properties of the system can be obtained exactly.

It is clear from eq. (4.9) that the properties of this system depend on how the step is coarse-grained, i.e., how closely spaced ($\Delta x = L/M$) are the M points describing the step line. This is a reflection of the number of degrees of freedom attributed to the step effective Hamiltonian [125, 126], eq. (4.6), as discussed in sec. 4.2.1; Δx determines the largest wavevector considered in the effective Hamiltonian of eq. (4.9): $k_{\max} \equiv \pi/\Delta x$. An extensive review of the consequences and interpretations of this dependency on Δx and, consequently, on the capillary-wave wavelengths considered, is given in ref. 125. We return to this point in sec. 4.5 when comparing the results of the CFM analysis to the values of the step free energy computed in ref. 55.

Notice that the term σL in eq. (4.9) is a simple shift in energy, thus the dynamics of the step is completely parametrized by the step stiffness $\tilde{\sigma}$. In the next section we review how $\tilde{\sigma}$ can be derived from atomistic simulations.

4.2.3 Step fluctuation spectrum

According to the equipartition theorem each quadratic degree of freedom in the Hamiltonian of a system at constant temperature T contributes $k_{\mathrm{B}}T/2$ to the system's average energy. We can apply this theorem to eq. (4.9) since each mode amplitude A_n appears quadratically in the Hamiltonian. Notice that the real and imaginary parts of A_n are independent and, thus, each part contributes with $k_{\mathrm{B}}T/2$ to the total energy. Hence

$$\tilde{\sigma} L k_n^2 \left\langle |A_n|^2 \right\rangle = k_{\mathrm{B}}T,$$

where $\langle \ldots \rangle$ indicates a canonical ensemble equilibrium average. This equation can be used to compute the step stiffness, $\tilde{\sigma}$, if we rewrite it as

$$\left\langle |A_n|^2 \right\rangle = \left(\frac{k_{\mathrm{B}}T}{\tilde{\sigma} L} \right) \frac{1}{k_n^2}. \tag{4.10}$$

The normal-mode amplitudes can be obtained from atomistic simulations and used to adjust a curve of $\langle |A_n|^2 \rangle$ versus k_n^{-2}, from which $\tilde{\sigma}$ can be extracted.

When using eq. (4.10) to compute $\tilde{\sigma}$ it is necessary to define the step profile, shown as $y(x)$ in fig. 4.1. Hence, the value of $\tilde{\sigma}$ obtained can be sensitive to how $y(x)$ is determined, particularly if one relies on normal modes with wavelengths comparable to the atomic spacing. The physical origin of this arises because the distinction between interface and bulk degrees of freedom is not clear for atomistic systems [125], i.e., the definition of the interface position from the atomic configuration is ambiguous. In sec. 4.3.3 we study the inherent ambiguity in defining the step configuration in atomic-scale simulations and discuss how $y(x)$ can be determined in such a way as to minimally affect the value of $\tilde{\sigma}$ obtained from eq. (4.10).

4.3 Methodology of atomistic simulations

4.3.1 Molecular dynamics simulations and system geometry

Molecular dynamics simulations of surface steps were performed using the LAMMPS [29] (Large-scale Atomic/Molecular Massively Parallel Simulator) software. The interatomic interactions were described by the embedded-atom method [33] for a system of pure copper [88] and the Langevin thermostat [90] was used to sample the particles' phase space according to the canonical ensemble distribution. The thermostat relaxation time was $\tau_{\mathrm{L}} \equiv m/\gamma = 2\,\mathrm{ps}$, where γ is the friction parameter and m the atomic mass. The timestep (Δt) for the integration of the equations of motion was chosen based on the phonon spectrum of the system; we used $\Delta t = 2\,\mathrm{fs}$ which is approximately 1/60th of the oscillation period of the highest-frequency normal mode of this system.

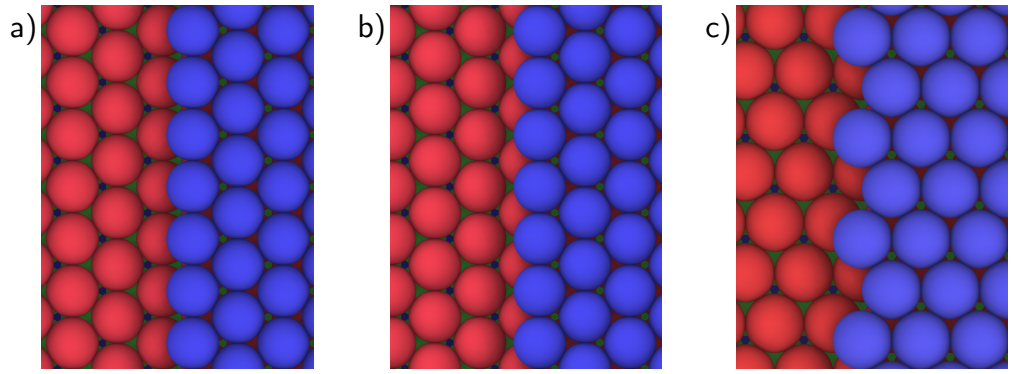

Figure 4.2: Step orientations on the (111) surface of face-centered cubic copper. The blue (dark gray) atoms on the right are in the first layer, and the red ones (light gray) on the left are in the second layer. The orientations are (a) [110]A, (b) [110]B, and (c) [211]. The difference between the [110] A and B steps are the nearest neighbors on the layer immediately below the step.

The geometry of the simulation box is illustrated in fig. 4.1. Periodic boundary conditions were used for the directions parallel to the surface ($\hat{\mathbf{x}}$ and $\hat{\mathbf{y}}$) while free boundaries were used along $\hat{\mathbf{z}}$ to create the system surface. We kept the box length along the $\hat{\mathbf{x}}$ and $\hat{\mathbf{y}}$ directions fixed while the system fluctuates freely along $\hat{\mathbf{z}}$ (normal to the surface) in order to guarantee mechanical equilibrium with the vacuum. A non-orthogonal simulation box [129] was employed in such a way as to have only one step on the system surface.

We have chosen the (111) surface of face-centered cubic copper as a representative metal surface to study steps. The surface properties of the interatomic potential employed have been studied extensively previously [79, 55]. Of relevance for this study is the fact that the {111} surfaces have been found to be faceted at all temperatures up to the melting point of this model ($T_\mathrm{m} = 1327\,\mathrm{K}$). In order to study effects of anisotropy we will consider steps of two different orientations (fig. 4.2), with step line directions along [110] and [211]. The [110] direction presents two distinct steps, [110]A and [110]B, which have different nearest-neighbor configurations on the layer immediately below the step, as illustrated in fig. 4.2. The temperature for all simulations was $T = 1300\,\mathrm{K}$; it was chosen to be close to the melting point so that the step fluctuation timescales were compatible with the short physical times accessible to the MD simulations. In sec. 4.3.4 we present an analysis of the step fluctuation relaxation times to assess which modes are adequately sampled.

4.3.2 System dimensions

Surface steps deform the crystalline lattice around them creating an elastic field that can interact with other elastic fields present in the crystal. The total energy of an isolated step will be referred to as the self-energy (U_0). Because of the periodic boundary conditions applied in the simulations the step can interact with its periodic images, as well as with the surface at the bottom of the simulation box (fig. 4.1). The effects of these interactions can be made negligibly small by choosing system dimensions such that the interaction energy is much smaller than U_0.

Simulation box dimensions ($d \times h \times L$)				
	d (Å)	h (Å)	L (Å)	U_0 (meV/Å)
[110]A	60.5	42.8	104.8	103.1
[110]B	66.6	42.8	104.8	104.1
[211]	62.9	42.8	108.9	120.5

Table 4.1: Simulation box size used for each step orientation. d is the step-step distance, h the bulk depth, L the step length, and U_0 is the step self-energy. The box geometry is illustrated in fig. 4.1.

The step-step interaction energy decreases with the distance d between the steps as [5] $E_{\text{int}} \propto d^{-2}$ and can be attractive or repulsive depending on the orientation of the steps. To determine the magnitude of this interaction we followed the approach from ref. 129 and computed the step-step interaction energy for different step separations. We have chosen the step-step separation distance for our simulations as the minimum distance such that $E_{\text{int}}/U_0 \leq 10^{-4}$. In practice this resulted in distances $d \approx 60\,\text{Å}$ as shown in Table 4.1.

The bulk depth (h in fig. 4.1 and Table 4.1) was determined by considering the step elastic-field decay along $\hat{\mathbf{z}}$, the direction normal to the surface. The step elastic energy ($E_{\text{step}}^{\text{bulk}}$) decays with the bulk depth proportionally to $\exp(-h/\xi)$ where ξ is a characteristic length which depends on the step orientation and length. After we verified this relationship we used it to impose the same energy tolerance used for the step-step interaction, i.e., $E_{\text{step}}^{\text{bulk}}/U_0 \leq 10^{-4}$. The selected bulk depth values are shown in Table 4.1. In all simulations presented here the last six layers of (111) planes at the bottom of the simulation box were frozen at their equilibrium position to guarantee that no bending of the structure would occur. The frozen layers were added beyond the values of bulk of depth h shown in Table 4.1.

In order to determine the simulation system dimension corresponding to the step length L it is necessary to consider the assumptions of the CFM, as presented in sec. 4.2. This model is not valid for the description of the step at scales smaller than its coarse-graining scale (Δx), thus we need $L \gg \Delta x$. However, it would be computationally unfeasible to have a step that is excessively large since the relaxation time of normal modes with long wavelength can be very long on MD time scales due the long-range atomic diffusion necessary to change the configuration of these modes. Therefore, it is necessary to study the normal-mode relaxation times before determining what is a satisfactory step length. The details of the analysis of these relaxation times is presented in sec. 4.3.4, and based on the results we have chosen $L \approx 100\,\text{Å}$ as shown in Table 4.1. This step length is equivalent to the largest relaxation time of the normal mode (with largest wavelength) being $\tau_{\max} \approx 1\,\text{ns}$.

4.3.3 Step profile determination

Given any interface between two distinct phases there is no unambiguous approach to determine the interface position from the microscopic atomistic structure of the system [125, 130]. Therefore, there is no algorithm that uniquely defines the step position, i.e.,

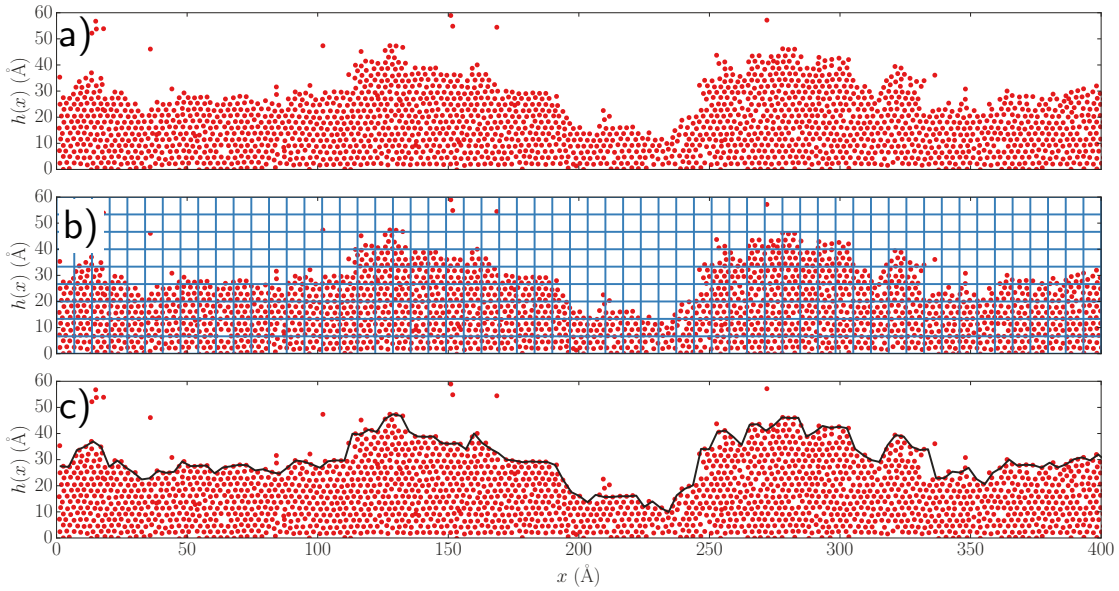

Figure 4.3: Illustration of the grid algorithm for step profile determination. (a) We select the atoms belonging the first surface layer by selecting all atoms with height above some threshold based on the number of atomic layers in the system. (b) Then we define a grid along the $\hat{\mathbf{x}}$ direction and divided each of these stripes in equally spaced bins along the $\hat{\mathbf{y}}$ direction. (c) The step height is defined as the average height between the first cell with zero density along a stripe and the cell immediately below it.

the one-dimensional interface separating two surface terraces. Here we compare two different algorithms [131, 130, 132, 121, 122] that determine the step profile from the atomic configurations captured in MD simulations.

Based on the dimensions for d and h presented in Table 4.1 we have constructed a system with a [110]A step with step-step distance $d = 60.5$ Å, bulk depth $h = 42.8$ Å, and step length $L = 403.6$ Å. This system was equilibrated for 10 ns and, afterwards, the step configuration was captured every 0.2 ps for 100 ns. All results presented in this section were obtained from this simulation. From the MD snapshots the atoms belonging to the top surface layer could be readily identified by counting the number of (111) planes and selecting all atoms with height above some threshold height based on the interplanar separation. One snapshot of the result of this selection is shown in fig. 4.3(a); from snapshots like this one we want to define the step line profile, being careful to not select any adatom belonging to the surface and also to not accidentally exclude atoms belonging to the step.

The first algorithm used will be referred to as the "grid algorithm". In this algorithm the direction along the step length, $\hat{\mathbf{x}}$, is divided in equally spaced bins or delimiting strips, as illustrated in fig. 4.3(b). We further divide each of these strips along $\hat{\mathbf{y}}$, creating rectangular cells, and calculate the density of atoms in each cell. The step height is chosen as the average value of the height of the first bin with zero density and the bin immediately before it. The parameters chosen for the dimension of each bin was 4.5 Å parallel to the step line and 6.7 Å perpendicular to the step line.

The second algorithm used is referred to as the "cluster algorithm", illustrated in fig. 4.4.

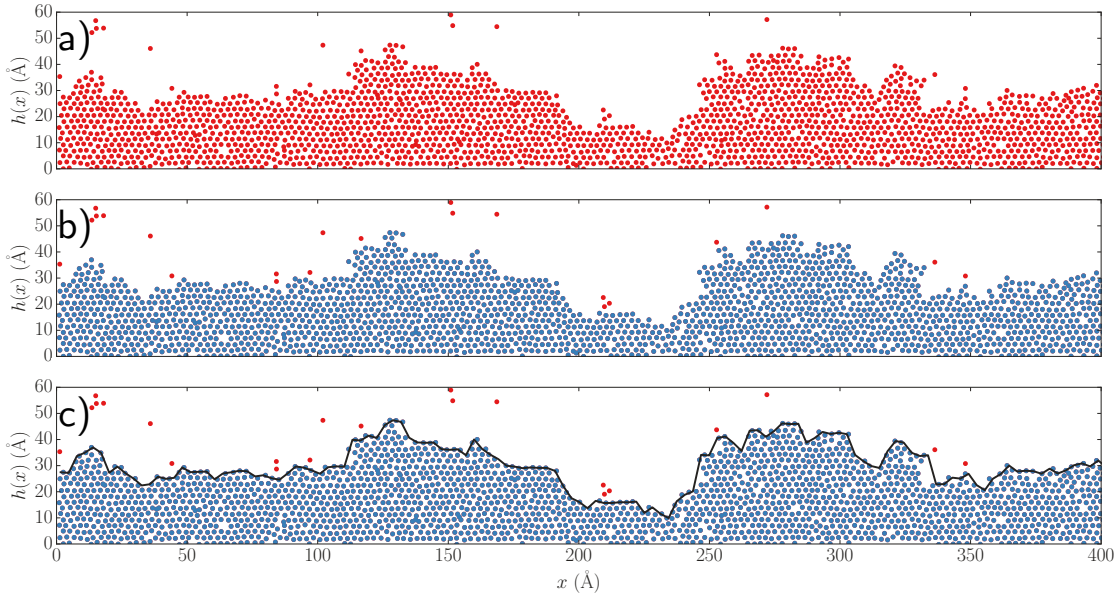

Figure 4.4: Illustration of the cluster algorithm for step profile determination. (a) We determine the atoms belonging the first surface layer by selecting all atoms with height above some threshold based on the number of atomic layers in the system. (b) Then we find the largest cluster of atoms in that layer (light gray atoms), where we consider two atoms to be neighbors if the distance between them is smaller than some distance $r_{\max}$. (c) The system is divided in bins along the $\hat{\mathbf{x}}$ direction, and the step height in each bin is determined as the atom with the highest value of $y(x)$ inside that bin.

Once again we start with the atomic configuration of the first layer, then determine all atomic clusters on this layer. Two atoms are considered to belong to the same cluster if there is a path between them through a sequence of neighbor atoms, where we consider two atoms to be neighbors if the distance between them is equal or smaller than some maximum radius $r_{\max}$. The step atoms are then defined as the largest cluster of atoms, as shown in fig. 4.4(b). From the configuration of the atoms belonging to the step the surface can be readily divided into strips along the $\hat{\mathbf{x}}$ direction and the atom with the highest value of $y(x)$ within that strip is selected to be the step height at that point. The cluster algorithm has the advantage of having only one adjustable parameter, namely, the maximum nearest-neighbor distance $r_{\max}$, which can be easily estimated by considerations of the crystal lattice geometry. We have taken $r_{\max} = 1.2 r_{\mathrm{n}}$, where r_n is the distance between nearest neighbors in the lattice, and the discretization length along the step line was 2.7 Å.

We have optimized both algorithms with respect to the parameters involved to obtain step profiles that best adjust to the real atomic configurations. Then we performed the Fourier transform of the height profiles and calculated the power spectrum (i.e., $|A_n|^2$ versus k_n). The comparison of the algorithms is shown in fig. 4.5 along with a straight line of slope -2. The agreement of the power spectrum with the k_n^{-2} behavior predicted by the CFM in eq. (4.10) is observed, this is an indication that the theory is adequate to describe the step fluctuations at the wavelengths probed in the MD simulations. From fig. 4.5 we also see that the long-wavelength modes (small k_n) are insensitive to the choice of coarse-graining

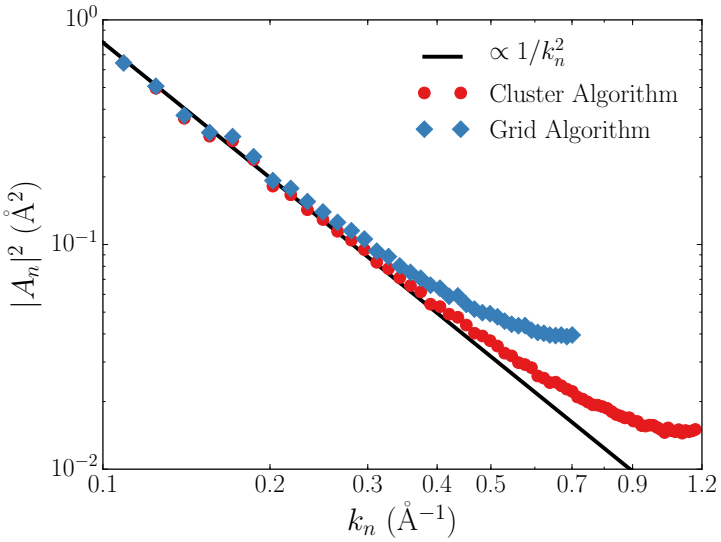

Figure 4.5: Comparison of the power spectrum of the Fourier transform of the step line profile obtained using different algorithms to determine the step profile. The cluster algorithm has shown to result in a power spectrum which better follows the k_n^{-2} behavior expected from the capillary-wave model (CFM).

algorithm, as observed before in this type of analysis [132, 131]. At intermediate values of k_n the cluster algorithm is observed to follow the CFM prediction, eq. (4.10), to higher wave numbers than the grid algorithm. Hence, the cluster algorithm is preferred for capturing the step profile details, and this algorithm has been used for analyses of step fluctuations in the remainder of this chapter. We also see that for large k_n both algorithms deviate from the k_n^{-2} behavior. This happens because when the normal-mode wavelength becomes comparable to the interatomic distance the atomic vibrations start to interfere with the step oscillations. The CFM was proposed to describe the long-wavelength capillary waves but it does not account for the discrete nature of the atomic configuration and degrees of freedom, thus it is no surprise that when these effects start to become significant (large k_n) our results start to deviate from the CFM. We further discuss the validity of the CFM to describe surface steps in sec. 4.4.

4.3.4 Step normal mode relaxation times

Each normal mode in eq. (4.10) has a different relaxation time since mass transport is required for changes in the step configuration. Short wavelength modes can change their configuration quickly since they only require short-range diffusion to modify their amplitudes, while modes with small k_n have long relaxation times that limit the statistics for their sampling in the MD simulations. Thus, these relaxation times ultimately place a limit on the wavelengths that can be probed in the simulations.

The relaxation time of the normal modes are analyzed from the simulation data employing a time autocorrelation function of the amplitudes, i.e., if $f_n(t) = |A_n(t)|^2$ then the

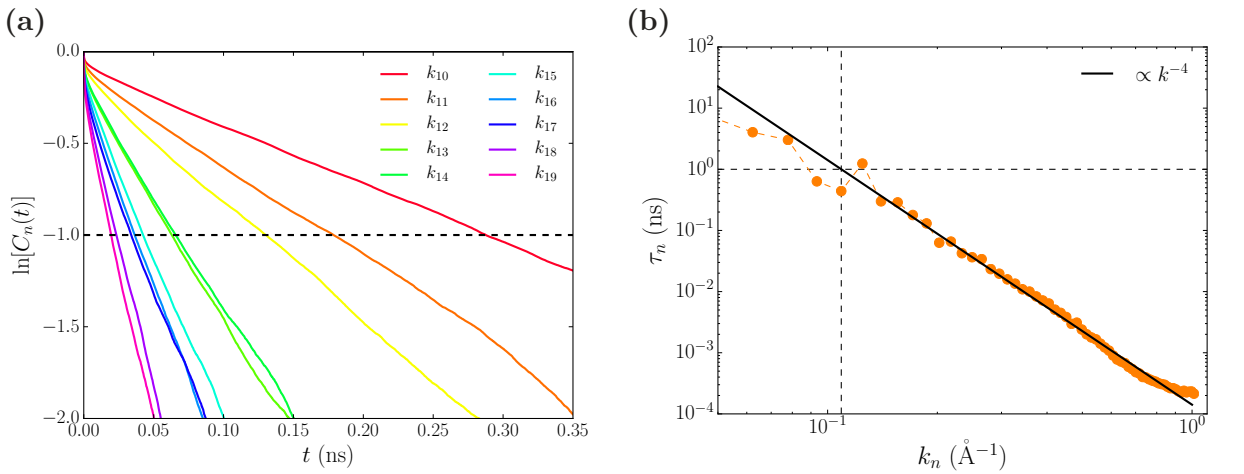

Figure 4.6: **(a)** Typical autocorrelation functions obtained for the normal modes' amplitudes (normal mode index increases in the clockwise direction or from the upper right to the bottom left). The normal modes relaxation times (τ_n) are obtained by fitting $C_n(t)$ curves to eq. (4.11). **(b)** Relaxation time of each normal mode of the step line profile. τ_n is obtained by fitting $C_n(t)$ curves to eq. (4.11). The horizontal line corresponds to $\tau_n = 1\,\text{ns}$ and the vertical line marks the wavevector value at which the adjusted curve (black solid line) intercepts the $\tau_n = 1\,\text{ns}$ relaxation time, i.e., the vertical line is at $k_n = k_{\text{min}}$.

autocorrelation function $C_n(t)$ is

$$C_n(t) = \frac{\langle f_n(t) f_n(0)\rangle}{\langle f_n(0)^2\rangle} = \exp(-t/\tau_n), \tag{4.11}$$

where τ_n is the relaxation time of the normal mode of wavevector k_n. Representative plots of $C_n(t)$ for selected normal modes are shown in fig. 4.6a, and from such data we can estimate the relaxation time of each mode, as shown in fig. 4.6b. The data used to obtain figs. 4.6a and 4.6b was extracted from the simulation performed in sec. 4.3.3 for a $[110]A$ step.

Notice in fig. 4.6b that the MD simulations resulted in $\tau_n \propto k_n^{-4}$. This result indicates that the step capillary fluctuations are predominantly governed by atomic diffusion [108] along the step line, as opposed, for example, to diffusion of adatoms on the terrace, which would lead [113] to $\tau_n \propto k_n^{-3}$, or adatom attachment or detachment to or from the step edge that would be consistent with $\tau_n \propto k_n^{-2}$.

From the relaxation times obtained in fig. 4.6b the step length appropriate for the MD simulation cells is determined as follows. We have limited the maximum relaxation time to be $\tau_{\text{max}} = 1\,\text{ns}$, with this limitation the shortest wavevector we can sample is $k_{\text{min}} \approx 0.11\,\text{Å}^{-1}$ and the shortest step to contain this wavevector has a length of $L \approx 57\,\text{Å}$. Because we are making conservative choices for the step length of all other orientations, and to increase the number of points used in the fitting of eq. (4.10), we have chosen to use step lengths of approximately 100 Å. The dimensions for the simulation cells used to obtain the results presented below are listed in Table 4.1.

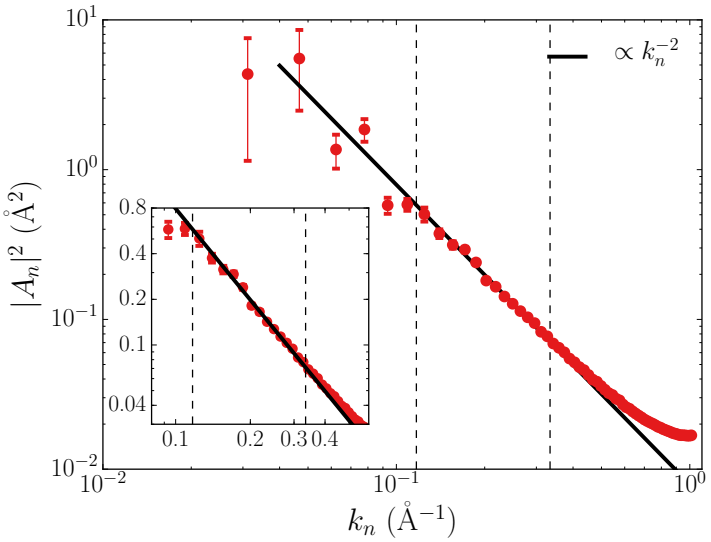

Figure 4.7: Power spectrum plot of the Fourier transform of the step line profile. Long wavevectors were discarded since they deviate from the $\langle |A_n|^2 \rangle \propto k_n^{-2}$ behavior due to the presence of atomic vibrations not accounted for the CFM, as presented in sec. 4.2. Short wavevectors were discarded because their relaxation time was long enough to be comparable to the total simulation time, hence they cannot be adequately sampled in a MD simulation. The dashed lines delimit the wavelengths used for adjusting the black solid curve to eq. (4.10). The inset highlights the agreement of the normal modes considered with the CFM predictions.

4.4 Results

Plotted in fig. 4.7 are the results of the MD calculated fluctuation amplitudes $\langle |A_n|^2 \rangle$ versus k_n, obtained as described in sec. 4.3.3 with the cluster algorithm used to characterize the instantaneous step profile. Using the normal modes with wavevectors $k_{\min} < k_n < k_{\max}$, where $k_{\min} = 0.110\,\text{Å}^{-1}$ and $k_{\max} = 0.335\,\text{Å}^{-1}$ (shown as dotted lines in fig. 4.7), we have verified the $\langle |A_n|^2 \rangle \propto k_n^{-2}$ behavior predicted by eq. (4.10) by adjusting a general power law to these points, as shown in the inset of fig. 4.7.

As explained in sec. 4.3.4 the $k_{\min}$ value was determined based on the largest relaxation time that can be adequately sampled in the MD simulations we performed. It is clear in fig. 4.7 that as k_n decreases below $k_{\min}$ the error bars become larger due to the reduced sampling statistics, associated with the longer relaxation times and the total simulation time of 100 ns.

The value of $k_{\max}$ was chosen by comparing the MD results in fig. 4.7 to a curve with slope k_n^{-2} and visually deciding at which point the data started to diverge from this behavior, $k_{\max}$ was selected as the average of the k_n value of that point and the one immediately before it. Although the choice of $k_{\max}$ is not unique (e.g., it depends on the method used to characterize the step profile), it is not completely arbitrary either and reasonable estimates can be made by inspection of the MD results, as shown in fig. 4.7. Specifically, it is clear from fig. 4.7 that at large enough k_n the MD data deviates from the k_n^{-2} behavior predicted by the CFM, and the point where this discrepancy becomes statistically significant provides the basis for

	Step stiffness $\tilde{\sigma}$ (meV/ Å)			
	(d, h, L)	$(d, 2h, L)$	$(2d, 1.7h, L)$	U_0
[110]A	37	36	37	103.13
[110]B	38	39	37	104.08
[211]	36	36	37	120.53

Table 4.2: Step stiffness for different step orientations and convergence with box size. All columns have error bar $\pm 1\,\mathrm{meV/\,\AA}$, except for the U_0 column where the error bar is $\pm 0.02\,\mathrm{meV/\,\AA}$. d is the step-step separation distance, h is the bulk depth, L is the step length, and U_0 is the step self energy. The dimensions used are with respect to the box sizes presented in Table 4.1. The box geometry is illustrated in fig. 4.1.

a reasonable estimate of a lower bound for $k_{\max}$. Hence, an important criterion is to adjust the k_n^{-2} curve in such a way that the data for small k_n lies accurately on the k_n^{-2} curve. With that reference, the only arbitrariness comes from deciding where the data starts to deviate from the curve location imposed from the small k_n points data. Here the cutoff $k_{\max} = 0.335\,\mathrm{\AA}^{-1}$ corresponds to a wavelength of $\lambda \approx 7.2a$, where a is the atomic distance along the step line for steps along $\langle 110 \rangle$ directions. This result implies that it is necessary to average over approximately seven atoms to eliminate noise due to atomic vibrations and correlated atomic displacements, to correctly capture the expected capillary wave behavior, consistent with the coarse-graining over atomic degrees of freedom necessary to define the step effective Hamiltonian $\mathcal{H}$ described in sec. 4.2.

According to eq. (4.9) the step effective Hamiltonian depends on two parameters: the step tension of a straight step (σ) and the step stiffness ($\tilde{\sigma}$). For each step orientation listed in Table 4.1 we have run a 100 ns simulation preceded by a 5 ns equilibration period and applied eq. (4.10) to obtain the step stiffness. The result is shown in the first column of Table 4.2. We have employed three different box sizes to test for size convergence: one with twice as much bulk depth and another with twice as much step-step distance (increasing the bulk depth to account for the deeper penetration of the step elastic field). Also listed in Table 4.2 are the step energies U_0 at $T = 0\,\mathrm{K}$.

The zero-temperature values U_0 are observed to show a significant anisotropy between the $\langle 110 \rangle$ and $\langle 211 \rangle$ orientations: a difference of $\approx 14\%$ characterizes these values in Table 4.2. By contrast, at 1300 K the MD results yield stiffness values that are isotropic within the statistical precision of the MD data. These results imply that $\tilde{\sigma} \approx \sigma$, i.e., that the contribution of σ'' to the stiffness is negligible. The observed decrease in anisotropy of the step tension is interpreted to reflect the fact that when the step fluctuation amplitudes become large on the scale of the atomic dimensions the effects of the lattice are averaged out.

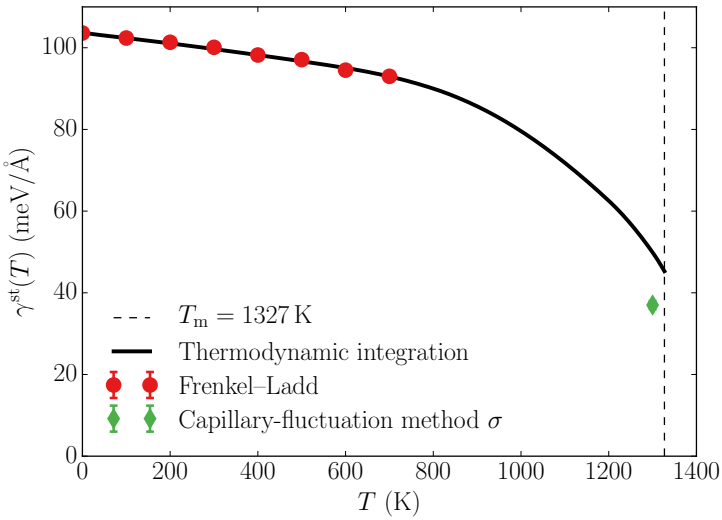

Figure 4.8: Comparison of the step free energy obtained from thermodynamic integration simulations (ref. 55) with the predictions of the capillary-wave model.

4.5 Discussion

In this section the present CFM results are compared with values of the step free energy for the same system obtained by thermodynamic-integration methods previously [55]. In fig. 4.8 we plot the results from the previous TI calculations, where the solid black line gives the temperature dependence of the step free energy up to the melting point for a $\langle 110 \rangle$ step orientation and the red circles are independent results obtained from TI calculations using the Frenkel-Ladd method. Also plotted in fig. 4.8 with the diamond symbol is the step tension σ, which is assumed isotropic based on the MD results presented in the previous section, and thus equal to the step stiffness. It can be seen that the value of σ obtained from the CFM analysis of the present MD data is lower than the step free energy obtained in ref. 55 by approximately 25%: at $T = 1300\,\mathrm{K}$ the TI results yield $\gamma^{\mathrm{st}} = (50.4 \pm 0.4)\,\mathrm{meV/\,\AA}$, while the CFM yields $\sigma = (37 \pm 1)\,\mathrm{meV/\,\AA}$. We discuss this discrepancy in what follows in the context of statistical-mechanical theories of capillary fluctuations (e.g., refs. 125, 114, 126, 133).

We begin by noting the differences in the way the two quantities are defined. In the TI (thermodynamic) formalism, which is Gibbsian in spirit, step free energy is defined as an excess free energy per unit length of the system (simulation block in this case). This thermodynamic formalism does not rely on or characterize the physical length of the fluctuating step. The configurational free energy contributions associated with these fluctuations are naturally included in the TI method. By contrast, in the capillary-wave theory the step tension σ, introduced in eq. (4.6), is defined as a free energy per unit physical length of the fluctuating step. These considerations alone suggest that the step free energy obtained by the TI method and the step tension defined in the CFM are inherently different. Moreover, in the TI and CFM simulations the average physical length of the step is larger than that of the system dimension along the step by approximately 30% to 35% for the system sizes considered in ref. 55. In the TI formalism one could in principle introduce the total excess step

free energy per unit of average physical length, which in this case would be approximately 23% smaller that the value of γ^{st} given above.

To formalize the difference between the step stiffness and the step free energy, we note that in the literature, starting with the work of Buff et al. [114], there is a distinction drawn between σ, often referred to as the "bare" stiffness, and γ^{st}, the step free energy. In these theories, the latter differs from the former due to the configurational free energy contributions associated with the step fluctuations. Formally, this difference can be derived by the use of eq. (4.9) in eq. (4.5), resulting in an expression for the configurational free energy that depends on the number of modes (coarse-graining length), as well as a length scale that is used in eq. (4.5) to make the partition function dimensionless. These issues are discussed at length by Kayser [126], who derives an expression for the configurational contribution to γ^{st} that depends on system size and geometry. Importantly, this contribution can be shown to be always *negative*, and thus lowers the magnitude of the step free energy (γ^{st}) relative to the bare stiffness (σ). We note that, as shown in fig. 4.8, we find the opposite trend, such that this cannot be the explanation for our finding that σ derived from CFM analysis of the MD data is lower than γ^{st} derived from thermodynamic integration.

To further consider the origins for this difference, we note that one possibility is that the TI results in ref. 55 could suffer from hysteresis effects associated with sharp changes in the excess quantities as the step configuration evolves from being straight at low temperatures to rough at higher temperatures. We have investigated these issues in detail in our previous work and concluded that for the system sizes and time scales considered in ref. 55 the excess quantities behave smoothly and no evidence of artifacts that would bias the TI integration was found.

We consider then an alternative explanation for the discrepancy between the TI derived value of γ^{st} and CFM derived value of σ shown in fig. 4.8. Specifically, as discussed by Gelfand and Fisher [125] and also noted by Kayser [126], the theoretical analysis of Abraham [133] for one-dimensional line interfaces in the 2D Ising model shows that the stiffness that governs the growth the mean-square width of the step with system size is exactly equal to the interfacial free energy. This result suggests a limitation to the classical capillary-fluctuation theory where the two quantities σ and γ^{st} are distinct. This limitation is discussed by Kayser who argues that the stiffness that governs step fluctuations should depend on the wave number k of the fluctuation, i.e., Kayser argues that large-wavelength fluctuations "see a 'renormalized' surface tension" that differs from the bare stiffness due to the configurational degrees of freedom associated with the smaller wavelength fluctuations. In this picture, it could be possible that the stiffness governing step fluctuations for the lowest wave numbers considered in our simulations, which dominate our fitting of the MD data to extract the stiffness values, is lower than the value of γ^{st} obtained from TI in ref. 55 which considered considerably smaller step lengths. These considerations suggest an interesting direction for future work that would involve detailed analysis of the size dependence of both TI and CFM results in the calculation of step free energies.

4.6 Summary and conclusions

Molecular dynamics simulations have been employed in a study of capillary fluctuations of $\langle 110\rangle$A, $\langle 110\rangle$B, and $\langle 211\rangle$ steps on the (111) surface of face-centered cubic copper at a homologous temperature of 0.98. The simulation results were analyzed within the framework of the statistical-mechanical theory of capillary waves. Specifically, the mean-square fluctuation amplitudes $\langle |A(k)|^2 \rangle$ derived from the simulation data were found to follow the inverse square dependence on wave number (k^{-2}) predicted from capillary fluctuation theory over a range k_{min} to k_{max}. This range is bounded by values k_{min}, below which the fluctuation relaxation times were too long to be adequately sampled in an MD simulation of 100 ns, and k_{max}, above which the atomic-scale wavelengths of the fluctuations lead to deviations from from the theoretical k^{-2} scaling. Over this range of wave numbers, the fluctuation relaxation times were observed to display a dependence on wave number consistent with a k^{-4} scaling, corresponding to kinetics limited by step-edge diffusion. We notice that although there are no theoretical restrictions to the application of the CFM to temperatures much lower than T_{m}, it is possible to find a limit due to computational resources because lower temperatures will require longer simulation times to sample the step fluctuations adequately.

From the measured fluctuation amplitudes we derive step stiffness values ($\tilde{\sigma}$) for each of the step orientations considered, obtaining values for the largest system sizes of $(37 \pm 1)\,\mathrm{meV/\AA}$ that are isotropic within the statistical precision of the simulation results. The values of $\tilde{\sigma}$ derived by this CFM approach are compared to recent results for the step free energy (γ^{st}) obtained for the same system using an alternative thermodynamic-integration approach [55]. The TI values of γ^{st} and CFM values of $\tilde{\sigma}$ show discrepancies at the level of 25%.

We discuss that the level of discrepancy can be considered within statistical-mechanical theories for step free energies (e.g., ref. 125) that draw a distinction between values for the "bare" stiffness σ and the step free energy γ^{st} that arises from configurational free energy contributions to the latter. The theoretical considerations developed in this previous literature, discussed in the context of the present results, point to an opportunity to use the CFM analysis framework described in this chapter and the TI formalism in ref. 55 to derive more detailed insights into the connection between the (possibly k-dependent) values of σ that govern fluctuations at intermediate length scales and the step free energy.

Chapter 5:

Quantum effects on dislocation motion

5.1 Motivation and overview

Quantum motion of atoms known as zero-point vibrations is recognized to be important at low temperatures in condensed matter systems comprised of light atoms or ions, affecting such properties and behaviors as proton-transfer reactions [134, 135], vibrational spectra of water [136, 137] and ice [138, 139], and mechanical properties of low temperature helium [140, 141]. Recently, quantum motion of atoms was proposed to explain a long-standing discrepancy between theoretically computed and experimentally measured low-temperature resistance (Peierls stress) to dislocation motion in iron and possibly other metals with high atomic masses [142–144]. Here we report the first direct simulations of quantum motion of screw dislocations in iron within the exact formalism of Ring-Polymer Molecular Dynamics (RPMD) [48, 49] that rigorously accounts for quantum effects on the statistics of condensed-phase systems. Our quantum RPMD simulations predict only a modest ($\approx$13%) reduction in the Peierls stress in iron compared to its fully classical prediction. Our simulations confirm that reduction in the Peierls stress solely due to the zero-point energy (ZPE) is close to 50% predicted earlier [142], but its effect is substantially offset by an increase in the effective atom size with decreasing temperature, an effect known as quantum dispersion. Thus, quantum motion of atoms does not resolve the notorious discrepancy between theoretical and experimental values of the Peierls stress in iron.

5.2 Results and discussion

Experimental estimates for the Peierls stress τ_{P} in body-centered cubic (bcc) metals are obtained by relating this parameter to the low-temperature yield strength of the metal extrapolated to zero temperature. In α-iron, the so-obtained experimental estimates for τ_{P} range between 0.35 GPa and 0.45 GPa [145–148] whereas atomistic calculations consistently predict τ_{P} to be much higher, ranging between 0.9 GPa and 1.2 GPa depending on the interatomic potential model used in the calculations [149, 150, 142]. At first perceived as a failure of interatomic potentials, subsequent electronic structure calculations confirmed the stubbornly high theoretical values of τ_{P} in α-iron to be between 1.0 GPa and 1.4 GPa [151–153]. In ref. 142 the effect of zero-point vibrations was accounted for by computing an approximate quantum correction to the rate of dislocation motion predicted within the

The results presented in this chapter, section 2.4, and appendix B have been submitted to publication as an article with title "*Quantum effects on dislocation motion from Ring-Polymer Molecular Dynamics*" by Rodrigo Freitas, Mark Asta, and Vasily V. Bulatov [52]. The material is presented here with the permission of the coauthors.

classical transition state theory (TST) [142]. The resulting correction reduced the Peierls stress from its fully classical value of 0.9 GPa by about 50%, to $\tau_{\rm P} = 0.45\,{\rm GPa}$ thus bringing it in close agreement with the experimental estimates.

Although appealing, the dramatic two-fold reduction in the Peierls stress was predicted from a harmonic approximation to the classical TST in which classical populations of vibrational modes were replaced with their quantum analogs. Given its potential importance, here we re-examine the effect of zero-point vibrations on dislocation motion in α-iron using Ring-Polymer Molecular Dynamics [48, 49] simulations (RPMD). Based on Feynman's path integral formulation of quantum mechanics, RPMD is a rigorous method fully accounting for all effects of quantum motion of atoms on equilibrium statistical properties. As detailed in appendix B, RPMD amounts to a simultaneous simulation of P replicas of the entire N-atom system in which each atom is represented by its P clones connected into a "polymer ring" (a closed Feynman path) by elastic springs. RPMD is asymptotically exact in the limit $P \to \infty$. To take full advantage of RPMD accuracy, in the following we make no assumptions on the character of dislocation motion and measure the effect of zero-point vibrations on the Peierls stress in the most direct manner possible, akin to the very method by which the Peierls stress is estimated in experiment. Using the same interatomic model of α-iron as in ref. 142, here we compute the resistance to dislocation motion twice – first using fully classical Molecular Dynamics (MD) and then using RPMD simulations – and compare the results in the limit of zero temperature to assess the differences.

As a baseline for subsequent comparison, first we compute the Peierls stress using fully classical simulations. Defined as the minimal stress required to make a dislocation move in the limit of zero temperature, Peierls stress can be computed in a static simulation in which stress or strain is increased in increments, each increment followed by a full relaxation of atom positions. The Peierls stress is taken to be just one increment below the stress at which the dislocation begins to move. Our so-computed "static" Peierls stress is $\tau_{\rm P} = (0.98 \pm 0.01)\,{\rm GPa}$ for a $\frac{1}{2}\langle 111\rangle$ screw dislocation moving on a $\{112\}$ plane in the so-called twinning direction [154]. This value is close to the ones previously reported for the same potential [142, 143] ($\approx 0.91\,{\rm GPa}$). For reasons explained in appendix B, the RPMD method does not permit similar static calculations which prompted us to compute the same Peierls stress again but now using classical dynamic simulations, to facilitate subsequent direct comparisons with RPMD. Another reason for us to perform dynamic simulations was an alarming, even if unnoticed, discrepancy in the literature between "static" and "dynamic" predictions for the Peierls stress reported by different research groups for the same model potential of iron [150, 152, 155].

Shown in fig. 5.1 is the flow stress of a single screw dislocation extracted from our MD simulations, plotted as a function of simulation temperature. The flow stress is seen to decrease monotonically with increasing temperature which is typical of dislocations whose motion is temperature- and stress-activated: as the temperature is increased additional thermal energy becomes available helping the dislocation to overcome its motion barriers at an increased rate which requires lower stress to maintain the same dislocation velocity $v_{\rm d}$. To make sure that our "dynamic" calculations of the Peierls stress are consistent and robust, we performed two series of MD simulations over the same range of temperatures in which the dislocation was forced to move at two different velocities $v_{\rm d}$: $50\,{\rm m/s}$ and $10\,{\rm m/s}$

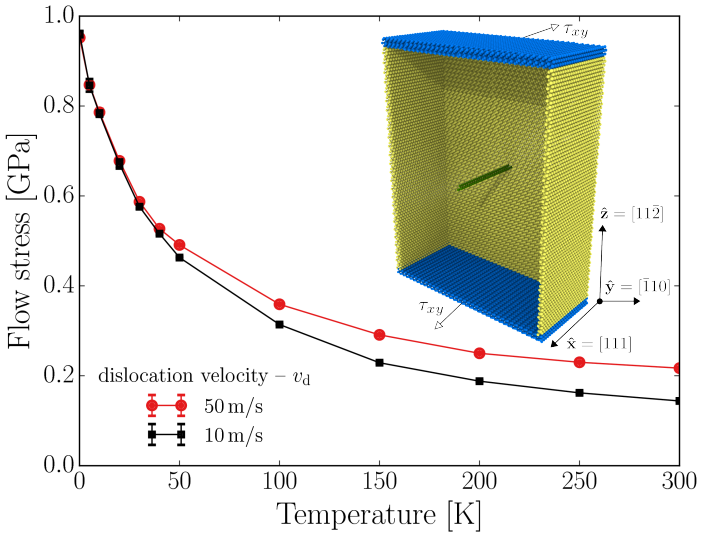

Figure 5.1: Flow stress of a single screw dislocation in iron predicted in classical MD simulations as a function of temperature. The simulations were performed at two different dislocation velocities v_d: 50 m/s (red symbols and red line) and 10 m/s (black symbols and black line). The statistical error bars are smaller than the symbols. The inset depicts the simulation volume in which most atoms are deleted for clarity except for atoms closest to the core of a $\frac{1}{2}\langle 111\rangle$ screw dislocation near the center (green) and atoms at the boundaries of the simulation volume (blue and yellow). To persuade the dislocation to move along the horizontal $(11\bar{2})$ plane, the blue atoms in the top and in the bottom layers were moved along the $\hat{\mathbf{x}}$ axis at constant and opposite velocities.

(see appendix B). As is seen in fig. 5.1, the flow stress at any given temperature is clearly velocity-dependent, however the same Peierls stress is obtained by extrapolation to $T = 0$ K: $\tau_P = (0.95 \pm 0.02)$ GPa at 50 m/s and $\tau_P = (0.96 \pm 0.02)$ GPa at 10 m/s. Within small error bars, our two "dynamic" predictions agree with our own as well as previously published "static" predictions for the Peierls stress [150, 152].

We now turn to RPMD simulations to compute the Peierls stress. Except for the method – classical MD versus quantum RPMD – our classical and quantum simulations were performed using the same interatomic potential and in otherwise identical simulation conditions. Figure 5.2 presents a comparison between MD and RPMD predictions of flow stress from 5 K to 50 K. Following the same extrapolation procedure previously used to extract the Peierls stress from the classical MD data, the Peierls stress predicted in the quantum RPMD simulations is 13% smaller than the classical MD result. In sec. 2.4 we present substantial evidence that our implementation of the RPMD method is highly accurate. Thus, we regard our prediction of only a modest reduction in the Peierls stress due to zero-point vibrations in α-iron as more accurate than the dramatic 50% reduction predicted earlier [142].

Although it may be difficult to separate factors that may have contributed to the substantial over-estimation of the effect of zero-point vibrations on the Peierls stress, several explicit or implicit assumptions used in ref. 142 to arrive at the dramatic prediction can be suspected. First, reliance on the fully classical TST in defining a critical pathway – a minimum energy path (MEP) – for quantum motion of atoms is inconsistent. Clearly,

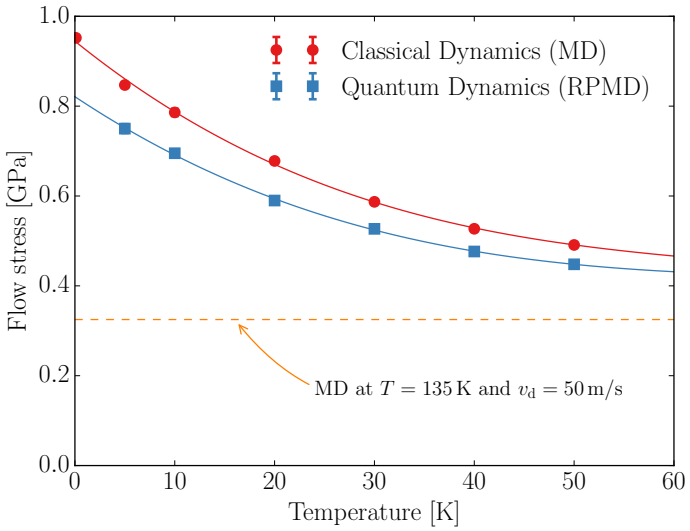

Figure 5.2: Temperature dependence of the flow stress of a single screw dislocation predicted in classical (red symbols and red line) and quantum (blue symbols and blue line) simulations. In both cases, the Peierls stress was obtained by a third-order polynomial (solid lines) extrapolation of the finite temperature flow stress to $T = 0\,\mathrm{K}$.

quantum-mechanical transition states relevant for dislocation motion must be defined and should be searched for in the extended space of closed Feynman paths [156, 157], i.e. in $3NP$-dimensional RPMD space. Another potential source of error is that Wigner correction (replacing the classical populations of vibrational states with the quantum ones) enhances the population of vibrational modes which accounts for the ZPE effect while ignoring other potentially important aspects of quantum motion. That something is amiss about limiting the effect of zero-point vibrations to just the Wigner correction is corroborated by the following qualitative argument.

As shown in fig. 5.3, the ZPE of a perfect crystal computed with the same interatomic potential model of iron (see appendix B) is 35 meV/atom. To approximately account for added agitation supplied in the form of zero-point vibrations, let us partition the ZPE equally between the potential and the kinetic energy per atom in the classical system, resulting in a classical temperature of 135 K. By reference to our classical MD results for the flow stress, fig. 5.1, this extra temperature would reduce the classical Peierls stress to 0.35 GPa, close to 0.45 GPa reported in ref. 142. That our explicit RPMD simulations predict a much more modest reduction suggests that some other effect(s) originating in quantum motion of atoms counterbalances this added agitation. We propose that such a contribution comes from quantum dispersion of atoms, i.e., finite size of a quantum particle compared to a point-particle in classical mechanics.

As was previously observed in the context of quantum diffusion [158] and glass transition in quantum liquids [159, 160], quantum dispersion can hinder atom re-arrangements because in condensed-phase systems the wave-packet of an atom is contracted due to its interaction with neighbor atoms. In other words, each atom is confined/squeezed by its neighboring atoms which reduces atom dimensions below its free-particle size. In RPMD, how much con-

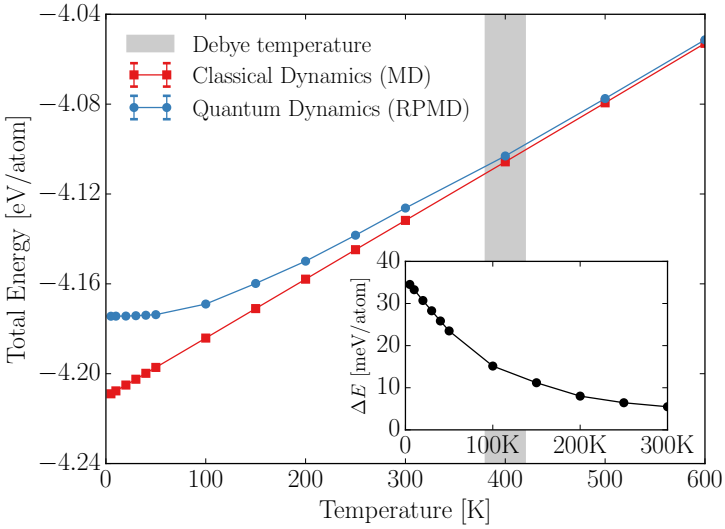

Figure 5.3: Temperature dependence of the per-atom energy in a perfect bcc lattice of α-iron in the quantum (blue symbols and blue line) and the classical (red symbols and red line) systems. Shown in the inset is the excess energy of the quantum system equal to the ZPE at $T = 0\,\mathrm{K}$. Shown as a gray vertical band is the Debye temperature of the model of α-iron studied here, $T_\mathrm{D} = (400 \pm 20)\,\mathrm{K}$.

finement from its neighbors an atom sees, can be assessed by computing the average radius of gyration r_G of the ring-polymers representing the atoms. Shown in the inset to fig. 5.4 is a plot of r_G in a perfect crystal computed for the same model of α-iron as a function of temperature (see appendix B). That atomic confinement is significant can be gauged from another plot in the same figure showing the ratio of r_G to the radius of gyration of a free atom $r_\mathrm{G}^\mathrm{free} = \sqrt{\hbar^2/mk_\mathrm{B}T}/2$ as a function of temperature. When it comes to thermally-activated mechanisms that require overcoming an energy barrier, such as dislocation motion, the already squeezed atoms have to additionally contract their wave packets as they pass through narrow paths leading over the barrier, this additional contraction resulting in an increase in both kinetic and potential energy of atomic configurations corresponding to the barrier states. In the temperature range between 5 K and 50 K explored in our RPMD simulations, r_G increases by 30% with decreasing temperature partially offsetting the 50% increase in the energy of zero-point vibrations over the same temperature interval (see fig. 5.3).

As a method for computing equilibrium statistical properties of quantum systems, RPMD is asymptotically exact in the limit of continuous Feynman paths ($P \to \infty$). On the other hand, motion dynamics of ring-polymers in RPMD is fictitious and does not necessarily reproduce dynamics of quantum motion of atoms. Every time RPMD is used to study dynamic properties, such as dislocation motion of interest here, the validity of simulation results must be carefully examined. Generally, for an RPMD simulation to be a valid representation of quantum dynamics, the simulated RPMD trajectory should consist of discrete transitions from one potential energy well (basin) to another. Further, the system should reside for a sufficiently long time within each energy basin before transitioning to the next basin, to forget about its preceding dynamic trajectory. This is precisely as expected in the equilibrium quantum TST for which RPMD was recently proven to be exact [156, 161, 162, 157, 163, 164].

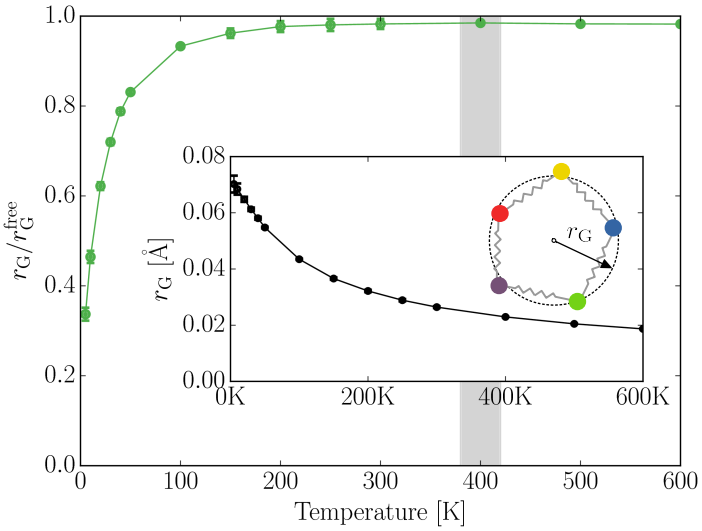

Figure 5.4: Temperature dependence of the time- and ensemble-averaged radius of gyration of ring-polymers r_G. r_G^{free} is the radius of gyration of a free particle of the same mass. The radius of gyration is a measure of the quantum dispersion of the atomic wave function.

For the classical TST to be applicable, the residence time within each basin should exceed the thermalization time. Additionally, when atomic motion is quantum, the same residence time should be longer than the quantum decoherence time (see appendix B). In our RPMD simulations, a screw dislocation moves in a stop-and-go fashion at the prescribed average velocity of 50 m/s. Given the distance between two neighboring energy basins (Peierls valleys) of 2.5 Å in α-iron, this velocity dictates that the dislocation spends on average 5 ps in each Peierls valley, including the residence and the transition segments of its RPMD trajectory as shown in fig. B.4. The quantum thermal time $\beta\hbar$ becomes longer than 5ps below $T = 5$K, as shown in fig. B.5, defining the lower bound temperature of our RPMD simulations. The upper bound of 50K is chosen judiciously, since we observed that at temperatures above 50K most of the 5ps time is spent in transition between the Peierls valleys rather than in residence in one of them. To extend the trust range of our RPMD simulations to temperatures above 50K, the dislocation should be allowed to spend longer time in each Peierls valley necessitating simulations at still lower dislocation velocities.

Our RPMD simulations of quantum motion of dislocations are unprecedented in scale and accuracy. Indeed, all previous RPMD simulations dealt with systems not exceeding a few thousand atoms at temperatures typically above 0.1 of the Debye temperatureT_D. By comparison, our RPMD simulations entail extended crystal defects embedded in a crystal lattice comprised of $\approx 150,000$ atoms at temperatures as low as $0.01\theta_D$. But RPMD method's rigor comes at a great computational cost: to achieve convergence of quantum RPMD simulations under such conditions, up to 200 replicas of the entire 150,000 atom system had to be integrated using time steps comprising a small fraction of one femtosecond over many nanoseconds. In terms of its raw computational cost, each RPMD simulation takes hundreds and thousands times more compute cycles per unit of simulated time compared to a classical MD simulation with the same interatomic potential. We achieved the needed computational

performance by building our RPMD simulations on top of an existing highly efficient MD code LAMMPS [29] and optimizing the resulting RPMD-LAMMPS method for massively parallel computing. To help make the RPMD method more accessible to materials scientists, we make our code freely available and give sufficient technical details of the method's implementation in sec. 2.4.

5.3 Summary and conclusions

We have developed an efficient implementation of the RPMD method enabling the study of extended defects in materials accounting accurately for quantum corrections to atom dynamics. We employ RPMD for a detailed investigation of the effect of quantum dynamics on dislocation motion in α-iron, which had been previously suggested as a source of the notorious discrepancy between calculated and measured values of the Peierls barrier in bcc metals. The present work utilizes RPMD to show that such corrections are smaller than previously suggested, likely due to quantum dispersion partially compensating the effect of ZPE. The results thus establish that the long-standing discrepancy between calculated and experimental estimates of the Peierls stress in bcc metals remains and further work is needed to settle this outstanding issue in physical metallurgy.

Chapter 6:

Summary and future work

In this chapter we present a summary highlighting the main conclusions and results of chapters 3, 4, and 5. We also discuss directions and suggestions for future work.

6.1 Thermodynamics and kinetics of surface steps

6.1.1 Step free energy at faceted solid surfaces

In chapter 3 a theory for the thermodynamic properties of steps on faceted crystalline surfaces was presented. The new formalism led to the definition of step excess quantities, including an excess step stress that is the step analogy of surface stress. A relationship was developed between the temperature dependence of the step free energy (γ^{st}) and step excess quantities for energy and stress that can be readily calculated by atomistic simulations. The application of this formalism was demonstrated in thermodynamic-integration (TI) calculations of the step free energy, based on Molecular Dynamics simulations, considering $\langle 110 \rangle$ steps on the $\{111\}$ surface of a classical potential model for elemental Cu. In this application we employed the Frenkel-Ladd approach to compute the reference value of γ^{st} for the TI calculations. Calculated results for excess energy and stress show relatively weak temperature dependencies up to a homologous temperature of approximately 0.6, above which these quantities increase strongly and the step stress becomes more isotropic. From the calculated excess quantities we computed γ^{st} over the temperature range of zero up to the melting point (T_{m}). We found that γ^{st} remains finite up to T_{m}, indicating the absence of a roughening temperature for this $\{111\}$ surface facet, but decreases by roughly fifty percent from the zero-temperature value. The strongest temperature dependence occurs above homologous temperatures of approximately 0.6, where the step becomes configurationally disordered due to the formation of point defects and appreciable capillary fluctuations.

6.1.2 Capillary fluctuations of surface steps

In chapter 4 Molecular dynamics (MD) simulations were employed to investigate the capillary fluctuations of steps on the surface of a model metal system. The fluctuation spectrum, characterized by the wave number (k) dependence of the mean squared capillary-wave amplitudes and associated relaxation times, was calculated for $\langle 110 \rangle$ and $\langle 112 \rangle$ steps on the $\{111\}$ surface of elemental copper near the melting temperature of the classical potential model considered. Step stiffnesses were derived from the MD results, yielding values from the largest system sizes of $(37 \pm 1)\,\mathrm{meV/\,\AA}$ for the different line orientations, implying that the stiffness is isotropic within the statistical precision of the calculations. The fluctuation

lifetimes were found to vary by approximately four orders of magnitude over the range of wave numbers investigated, displaying a k dependence consistent with kinetics governed by step-edge mediated diffusion. The values for step stiffness derived from these simulations are compared to step free energies for the same system and temperature in the MD-based TI result of chapter 3. Results from the capillary-fluctuation analysis and TI calculations yielded statistically significant differences that were justified within the framework of statistical-mechanical theories for configurational contributions to step free energies.

6.1.3 Future work

The thermodynamic formalism presented in this dissertation provides a general framework for the calculation of step free energies for elemental systems using atomistic simulation methods, and it is applicable beyond the application demonstrated in this work for elemental Cu modeled by an EAM classical potential. For example, the underlying approach can be extended to multicomponent/multiphase situations such as steps at faceted solid-liquid interfaces, grain boundaries and phase boundaries in multicomponent systems [93]. In practical applications to other systems, several considerations should be taken into account. First, the Frenkel-Ladd approach provides a methodology to compute step free energies only at temperatures where contributions of configurational disorder due to kinks, adatoms, and vacancies can be ignored, i.e., where vibrational contributions to the temperature dependence of the excess properties dominate; to ensure that this is the case sufficiently long simulations are required to guarantee structural equilibration, or theoretical analyses based on calculated kink and point-defect formation energies should be performed. For temperatures where the steps remain structurally ordered, the Frenkel-Ladd approach converges sufficiently rapidly that it is expected to be applicable to systems with more complex interatomic potentials, or even within the framework of DFT-based MD simulations, provided large enough systems can be considered to account for the strain fields around the steps and adequate sampling of the phonon spectra. Once reference values have been computed by the Frenkel-Ladd approach, the thermodynamic-integration formalism developed in this work can be used to compute step free energies incorporating configurational and vibrational contributions on an equal footing. In general, such calculations require combinations of efficient interatomic potential models and/or advanced sampling methods to enable equilibration of kink and point-defect densities. Nevertheless, provided these various considerations are taken into account, the formalism presented in this work provides a framework for computing benchmark results against which theories for vibrational (e.g., refs. 165 and 166) and configurational (e.g., refs. 167 and 125) contributions to the step free energies can be compared. We thus anticipate the approach to be useful for furthering understanding of the thermodynamic properties of steps on crystalline surfaces well beyond the application demonstrated in this dissertation.

Similarly, the application of the CFM steps can be generalized to multicomponent [117] and multiphase systems as well, resulting in a nice synergy with the TI approach. We notice that although there are no theoretical restrictions to the application of the CFM to temperatures much lower than T_{m}, it is possible to find a limit due to computational resources because lower temperatures will require longer simulation times to sample the

step fluctuations adequately. Additionally, the contributions due to capillary fluctuations can give rise to large size effects (due to the long-wavelength modes) particularly near the roughening temperature (e.g., refs. 125 and 168), and to account for these effects calculations with different system sizes and/or analysis of the capillary wave spectra may be necessary. The TI values of γ^{st} and CFM values of the stiffness, σ, show discrepancies at the level of 25% that, when considered within statistical-mechanical theories for step free energies (e.g., ref. 125), point to an opportunity to use the CFM analysis framework of chapter 4 and the TI formalism of chapter 3 to derive more detailed insights into the connection between the (possibly k-dependent) values of σ that govern fluctuations at intermediate length scales and the step free energy.

6.2 Quantum effects on dislocation motion

In chapter 5 we studied the thermally activated motion of dislocations in α-iron using a simulation method that rigorously accounts for quantum-fluctuations effects on the dynamics of condensed-phase systems, namely the Ring-Polymer Molecular Dynamics method [48, 49]. Calculated results for the flow stress of $\frac{1}{2}\langle 111\rangle$ screw dislocations show that quantum effects result in a 13% reduction in τ_{P} when compared to results from classical simulations, as obtained from Molecular Dynamics simulations. Moreover, we demonstrate that there are two competing factors that determine the magnitude of the Peierls stress reduction; the first is the zero-point energy due to the quantum occupation of phonon states, which facilitates the dislocation motion and reduces the Peierls stress. The second factor is the "swelling" of the atomic dimensions known as atomic quantum dispersion, this effect is due to the finite size of the atomic wave functions (as opposed to the point-particle representation in classical mechanics) and it counterbalances the effects due to the zero-point energy by hindering the motion of atoms past each other.

6.2.1 Future work

Recent studies suggested that zero-point vibrations should have important effects on dislocation motion even in metals with atomic weights much larger than hydrogen or its neighbors – for which such effects are widely appreciated – explaining long standing discrepancies between experimental estimates and theoretical predictions of the Peierls stress (τ_{P}) of body-centered cubic metals. The work presented in chapter 5 reaffirms this long-standing discrepancy between theoretical predictions and experimental estimates of the Peierls stress in bcc metals, establishing that quantum effects are most likely a modest correction to the Peierls stress that cannot account for the discrepancies between experimental and theoretical predictions. Thus, we conclude that whatever causes this discrepancy has a different physical mechanism not accounted for in the physical models employed so far. While further work is required to understand this outstanding issue in physical metallurgy, we speculate that it is likely to lie beyond the single dislocation behavior. Rather, the effect of dislocation interactions with other defects, which are unavoidable in experimental studies and neglected in current simulation approaches, should be considered.

Our work also confirms that zero-point energy alone – without consideration of other

quantum effects – results in an overestimation the role of quantum effects in dislocation motion. We suspect that the balance between zero-point energy and atomic dimensions is equally important for other metallic systems and the thermally activated motion of other defects, such as vacancies and interstitials. It would be interesting to extend the present analysis to these systems, and possibly to the mobility of dislocations in other systems with different lattice structures as well.

Finally, the RPMD code described in sec. 2.4 introduces the possibility of investigating quantum fluctuation effects on the dynamics of large systems where the interatomic interactions are described by force fields. Such simulations were not possible before due to the lack of adequate software integrating all necessary methods. Given the important role of quantum effects for light elements, the investigation of quantum effects on the properties of light metals such as beryllium and lithium might be a desirable next application of our code.

References

[1] W. Cai and W. D. Nix, *Imperfections in Crystalline Solids*. Cambridge University Press, 2016.

[2] R. Phillips, *Crystals, Defects and Microstructures: Modeling Across Scales*. Cambridge University Press, 2001.

[3] E. D. Williams, "Surface steps and surface morphology: understanding macroscopic phenomena from atomic observations," *Surface Science*, vol. 299, pp. 502–524, 1994.

[4] H.-C. Jeong and E. D. Williams, "Steps on surfaces: experiment and theory," *Surface Science Reports*, vol. 34, pp. 171–294, 1999.

[5] P. Müller and A. Saúl, "Elastic effects on surface physics," *Surface Science Reports*, vol. 54, pp. 157–258, 2004.

[6] G. S. Rohrer, "Grain boundary energy anisotropy: a review," *Journal of Materials Science*, vol. 46, p. 5881, 2011.

[7] M. Asta, C. Beckermann, A. Karma, W. Kurz, R. Napolitano, M. Plapp, G. Purdy, M. Rappaz, and R. Trivedi, "Solidification microstructures and solid-state parallels: Recent developments, future directions," *Acta Materialia*, vol. 57, pp. 941–971, 2009.

[8] P. R. Cantwell, M. Tang, S. J. Dillon, J. Luo, G. S. Rohrer, and M. P. Harmer, "Grain boundary complexions," *Acta Materialia*, vol. 62, pp. 1–48, 2014.

[9] J. P. Hirth and J. Lothe, *Theory of Dislocations*. John Wiley & Sons, 1982.

[10] V. Bulatov and W. Cai, *Computer Simulations of Dislocations*. Oxford University Press on Demand, 2006.

[11] L. A. Zepeda-Ruiz, A. Stukowski, T. Oppelstrup, and V. V. Bulatov, "Probing the limits of metal plasticity with molecular dynamics simulations," *Nature*, vol. 550, pp. 492–495, 2017.

[12] T. Zhu and H. Gao, "Plastic deformation mechanism in nanotwinned metals: an insight from molecular dynamics and mechanistic modeling," *Scripta Materialia*, vol. 66, pp. 843–848, 2012.

[13] C. Koch, R. Scattergood, K. Darling, and J. Semones, "Stabilization of nanocrystalline grain sizes by solute additions," *Journal of Materials Science*, vol. 43, pp. 7264–7272, 2008.

[14] T. Chookajorn, H. A. Murdoch, and C. A. Schuh, "Design of stable nanocrystalline alloys," *Science*, vol. 337, pp. 951–954, 2012.

[15] A. Jain, S. P. Ong, G. Hautier, W. Chen, W. D. Richards, S. Dacek, S. Cholia, D. Gunter, D. Skinner, G. Ceder, and K. a. Persson, "The Materials Project: A materials genome approach to accelerating materials innovation," *APL Materials*, vol. 1, p. 011002, 2013.

[16] J. Hachmann, R. Olivares-Amaya, S. Atahan-Evrenk, C. Amador-Bedolla, R. S. Sánchez-Carrera, A. Gold-Parker, L. Vogt, A. M. Brockway, and A. Aspuru-Guzik, "The Harvard Clean Energy Project: large-scale computational screening and design of organic photovoltaics on the world community grid," *The Journal of Physical Chemistry Letters*, vol. 2, pp. 2241–2251, 2011.

[17] B. J. Alder and T. E. Wainwright, "Phase transition for a hard sphere system," *The Journal of Chemical Physics*, vol. 27, p. 1208, 1957.

[18] S. Nosé, "A unified formulation of the constant temperature molecular dynamics methods," *The Journal of Chemical Physics*, vol. 81, pp. 511–519, 1984.

[19] W. G. Hoover, "Canonical dynamics: equilibrium phase-space distributions," *Physical Review A*, vol. 31, p. 1695, 1985.

[20] M. Parrinello and A. Rahman, "Polymorphic transitions in single crystals: A new molecular dynamics method," *Journal of Applied physics*, vol. 52, pp. 7182–7190, 1981.

[21] M. Tuckerman, B. J. Berne, and G. J. Martyna, "Reversible multiple time scale molecular dynamics," *The Journal of Chemical Physics*, vol. 97, pp. 1990–2001, 1992.

[22] M. S. Daw and M. I. Baskes, "Semiempirical, quantum mechanical calculation of hydrogen embrittlement in metals," *Physical Review Letters*, vol. 50, p. 1285, 1983.

[23] R. Car and M. Parrinello, "Unified approach for molecular dynamics and density-functional theory," *Physical Review Letters*, vol. 55, p. 2471, 1985.

[24] M. Parrinello and A. Rahman, "Study of an F center in molten KCl," *The Journal of Chemical Physics*, vol. 80, pp. 860–867, 1984.

[25] J. Cao and G. A. Voth, "The formulation of quantum statistical mechanics based on the Feynman path centroid density. I. Equilibrium properties," *The Journal of Chemical Physics*, vol. 100, pp. 5093–5105, 1994.

[26] R. P. Feynman and H. Kleinert, "Effective classical partition functions," *Physical Review A*, vol. 34, p. 5080, 1986.

[27] H. Jónsson, G. Mills, and K. W. Jacobsen, "Nudged elastic band method for finding minimum energy paths of transitions," in *Classical and Quantum Dynamics in Condensed Phase Simulations*. World Scientific, 1998, pp. 385–404.

[28] C. Dellago, P. G. Bolhuis, F. S. Csajka, and D. Chandler, "Transition path sampling and the calculation of rate constants," *The Journal of Chemical Physics*, vol. 108, pp. 1964–1977, 1998.

[29] S. Plimpton, "Fast parallel algorithms for short-range molecular dynamics," *Journal of Computational Physics*, vol. 117, pp. 1–19, 1995.

[30] D. Frenkel and B. Smit, *Understanding Molecular Simulation: From Algorithms to Applications*. Academic Press, 2001.

[31] M. P. Allen and D. J. Tildesley, *Computer Simulation of Liquids*. Oxford University Press, 2017.

[32] R. M. Martin, *Electronic Structure: Basic Theory and Practical Methods*. Cambridge University Press, 2004.

[33] M. S. Daw and M. I. Baskes, "Embedded-atom method: Derivation and application to impurities, surfaces, and other defects in metals," *Physical Review B*, vol. 29, p. 6443, 1984.

[34] M. S. Daw, S. M. Foiles, and M. I. Baskes, "The embedded-atom method: a review of theory and applications," *Materials Science Reports*, vol. 9, pp. 251–310, 1993.

[35] M. L. Cohen and S. G. Louie, *Fundamentals of Condensed Matter Physics*. Cambridge University Press, 2016.

[36] M. Tuckerman, *Statistical Mechanics and Molecular Simulations*. Oxford University Press, 2008.

[37] M. Tuckerman, B. J. Berne, and G. J. Martyna, "Reversible multiple time scale molecular dynamics," *The Journal of Chemical Physics*, vol. 97, pp. 1990–2001, 1992.

[38] E. Hairer, C. Lubich, and G. Wanner, *Geometric numerical integration: structure-preserving algorithms for ordinary differential equations*. Springer Science & Business Media, 2006, vol. 31.

[39] C. Störmer, "Sur les trajectoires des corpuscules electriques dans 1'espace sous 1'action du magnetisme terrestre, chapitre iv," *Arch. Sci. phys. et naturelles*, vol. 24, pp. 317–364, 1907.

[40] I. Newton, *Philosophiæ Naturalis Principia Mathematica*, 1687.

[41] L. Verlet, "Computer experiments on classical fluids. I. Thermodynamical properties of lennard-jones molecules," *Physical Review*, vol. 159, p. 98, 1967.

[42] R. P. Feynman and H. Kleinert, "Effective classical partition functions," *Physical Review A*, vol. 34, p. 5080, 1986.

[43] M. Parrinello and A. Rahman, "Study of an F center in molten KCl," *The Journal of Chemical Physics*, vol. 80, pp. 860–867, 1984.

[44] B. J. Berne and D. Thirumalai, "On the simulation of quantum systems: Path integral methods," *Annual Review of Physical Chemistry*, vol. 37, pp. 401–424, 1986.

[45] C. Cohen-Tannoudji, B. Diu, F. Laloë, and B. Crasemann, *Quantum Mechanics*. Wiley-VCH, 1992.

[46] R. P. Feynman, A. R. Hibbs, and D. F. Styer, *Quantum Mechanics and Path Integrals*. Courier Corporation, 2010.

[47] D. Chandler and P. G. Wolynes, "Exploiting the isomorphism between quantum theory and classical statistical mechanics of polyatomic fluids," *The Journal of Chemical Physics*, vol. 74, pp. 4078–4095, 1981.

[48] I. R. Craig and D. E. Manolopoulos, "Quantum statistics and classical mechanics: Real time correlation functions from ring polymer molecular dynamics," *The Journal of Chemical Physics*, vol. 121, 2004.

[49] S. Habershon, D. E. Manolopoulos, T. E. Markland, and T. F. Miller III, "Ring-polymer molecular dynamics: quantum effects in chemical dynamics from classical trajectories in an extended phase space," *Annual Review of Physical Chemistry*, vol. 64, 2013.

[50] T. F. Miller III and D. E. Manolopoulos, "Quantum diffusion in liquid para-hydrogen from ring-polymer molecular dynamics," *The Journal of Chemical Physics*, vol. 122, 2005.

[51] A. R. Menzeleev, N. Ananth, and T. F. Miller III, "Direct simulation of electron transfer using ring polymer molecular dynamics: Comparison with semiclassical instanton theory and exact quantum methods," *The Journal of Chemical Physics*, vol. 135, 2011.

[52] R. Freitas, M. Asta, and V. V. Bulatov, "Quantum effects on dislocation motion from ring-polymer molecular dynamics," *arXiv preprint arXiv:1712.04629*, 2017.

[53] J. C. Noya, C. P. Herrero, and R. Ramírez, "Thermodynamic properties of c-Si derived by quantum path-integral Monte Carlo simulations," *Physical Review B*, vol. 53, 1996.

[54] F. H. Stillinger and T. A. Weber, "Computer simulation of local order in condensed phases of silicon," *Physical Review B*, vol. 31, 1985.

[55] R. Freitas, T. Frolov, and M. Asta, "Step free energies at faceted solid surfaces: Theory and atomistic calculations for steps on the cu(111) surface," *Physical Review B*, vol. 95, p. 155444, 2017.

[56] T. L. Einstein, *Equilibrium Shape of Crystals*. Elsevier, 2014.

[57] H. H. Teng, P. M. Dove, C. A. Orme, and J. J. De Yoreo, "Thermodynamics of calcite growth: baseline for understanding biomineral formation," *Science*, vol. 282, pp. 724–727, 1998.

[58] E. D. Williams, R. J. Phaneuf, J. Wei, N. C. Bartelt, and T. L. Einstein, "Thermodynamics and statistical mechanics of the faceting of stepped si (111)," *Surface Science*, vol. 294, pp. 219–242, 1993.

[59] E. D. Williams, R. J. Phaneuf, J. Wei, N. C. Bartelt, and T. L. Einstein, "Erratum to "thermodynamics and statistical mechanics of the faceting of stepped si (111)"[surface science 294 (1993) 219]," *Surface Science*, vol. 310, pp. 451–452, 1994.

[60] J. Tersoff, Y. H. Phang, Z. Zhang, and M. G. Lagally, "Step-bunching instability of vicinal surfaces under stress," *Physical Review Letters*, vol. 75, p. 2730, 1995.

[61] N. C. Bartelt, J. Goldberg, T. L. Einstein, and E. D. Williams, "The equilibration of terrace width distributions on stepped surfaces," *Surface Science*, vol. 273, pp. 252–260, 1992.

[62] N. C. Bartelt, T. L. Einstein, and E. D. Williams, "The influence of step-step interactions on step wandering," *Surface Science*, vol. 240, pp. L591–L598, 1990.

[63] D. C. Schlößer, L. K. Verheij, G. Rosenfeld, and G. Comsa, "Determination of step free energies from island shape fluctuations on metal surfaces," *Physical Review Letters*, vol. 82, p. 3843, 1999.

[64] M. Giesen, C. Steimer, and H. Ibach, "What does one learn from equilibrium shapes of two-dimensional islands on surfaces?" *Surface Science*, vol. 471, pp. 80–100, 2001.

[65] C. Steimer, M. Giesen, L. Verheij, and H. Ibach, "Experimental determination of step energies from island shape fluctuations: a comparison to the equilibrium shape method for cu (100), cu (111), and ag (111)," *Physical Review B*, vol. 64, p. 085416, 2001.

[66] H. Gabrisch, L. Kjeldgaard, E. Johnson, and U. Dahmen, "Equilibrium shape and interface roughening of small liquid pb inclusions in solid al," *Acta materialia*, vol. 49, pp. 4259–4269, 2001.

[67] G. Schulze Icking-Konert, M. Giesen, and H. Ibach, "Novel method for the experimental determination of step energies," *Physical Review Letters*, vol. 83, pp. 3880–3883, Nov 1999.

[68] H. J. Zandvliet, "The ge (001) surface," *Physics Reports*, vol. 388, pp. 1–40, 2003.

[69] D. Frenkel and A. J. Ladd, "New monte carlo method to compute the free energy of arbitrary solids. application to the fcc and hcp phases of hard spheres," *The Journal of Chemical Physics*, vol. 81, pp. 3188–3193, 1984.

[70] R. Freitas, M. Asta, and M. de Koning, "Nonequilibrium free-energy calculation of solids using lammps," *Computational Materials Science*, vol. 112, pp. 333–341, 2016.

[71] P. J. Feibelman, "First-principles step-and kink-formation energies on cu (111)," *Physical Review B*, vol. 60, p. 11118, 1999.

[72] J. L. F. Da Silva, C. Barreteau, K. Schroeder, and S. Blügel, "All-electron first-principles investigations of the energetics of vicinal cu surfaces," *Physical Review B*, vol. 73, p. 125402, 2006.

[73] T. J. Stasevich, T. L. Einstein, and S. Stolbov, "Extended lattice gas interactions of cu on cu (111) and cu (001): Ab initio evaluation and implications," *Physical Review B*, vol. 73, p. 115426, 2006.

[74] J. W. Gibbs, *The Scientific Papers of J. Willard Gibbs*. Longmans, Green and Company, 1906, vol. 1.

[75] W. C. Johnson and J. M. Blakely, Eds., *Thermodynamics of Solid and Fluid Surfaces*. Metals Park, OH: American Society for Metals, 1979.

[76] V. I. Marchenko and A. Y. Parshin, "Elastic properties of crystal surfaces," *Sov. Phys. JETP*, vol. 52, pp. 129–131, 1980.

[77] L. E. Shilkrot and D. J. Srolovitz, "Elastic field of a surface step: Atomistic simulations and anisotropic elastic theory," *Physical Review B*, vol. 53, p. 11120, 1996.

[78] L. D. Landau and E. M. Lifshitz, *Theory of Elasticity*. Pergamon Press, Oxford, UK, 1986.

[79] T. Frolov and Y. Mishin, "Temperature dependence of the surface free energy and surface stress: an atomistic calculation for cu (110)," *Physical Review B*, vol. 79, p. 045430, 2009.

[80] W. Li, H. Duan, K. Albe, and J. Weissmüller, "Line stress of step edges at crystal surfaces," *Surface Science*, vol. 605, pp. 947–957, 2011.

[81] R. Shuttleworth, "The surface tension of solids," *Proceedings of the Physical Society. Section A*, vol. 63, p. 444, 1950.

[82] T. Frolov and Y. Mishin, "Thermodynamics of coherent interfaces under mechanical stresses. i. theory," *Physical Review B*, vol. 85, p. 224106, 2012.

[83] T. Frolov and Y. Mishin, "Solid-liquid interface free energy in binary systems: Theory and atomistic calculations for the (110) cu–ag interface," *The Journal of Chemical Physics*, vol. 131, p. 054702, 2009.

[84] T. Frolov and Y. Mishin, "Effect of nonhydrostatic stresses on solid-fluid equilibrium. ii. interface thermodynamics," *Physical Review B*, vol. 82, p. 174114, 2010.

[85] T. Frolov and Y. Mishin, "Thermodynamics of coherent interfaces under mechanical stresses. ii. application to atomistic simulation of grain boundaries," *Physical Review B*, vol. 85, p. 224107, 2012.

[86] B. B. Laird, R. L. Davidchack, Y. Yang, and M. Asta, "Determination of the solid-liquid interfacial free energy along a coexistence line by gibbs–cahn integration," *The Journal of Chemical Physics*, vol. 131, p. 114110, 2009.

[87] B. B. Laird and R. L. Davidchack, "Calculation of the interfacial free energy of a fluid at a static wall by gibbs–cahn integration," *The Journal of Chemical Physics*, vol. 132, p. 204101, 2010.

[88] Y. Mishin, M. J. Mehl, D. A. Papaconstantopoulos, A. F. Voter, and J. D. Kress, "Structural stability and lattice defects in copper: Ab initio, tight-binding, and embedded-atom calculations," *Physical Review B*, vol. 63, p. 224106, 2001.

[89] T. Frolov and Y. Mishin, "Effect of nonhydrostatic stresses on solid-fluid equilibrium. i. bulk thermodynamics," *Physical Review B*, vol. 82, p. 174113, 2010.

[90] T. Schneider and E. Stoll, "Molecular-dynamics study of a three-dimensional one-component model for distortive phase transitions," *Physical Review B*, vol. 17, p. 1302, 1978.

[91] A. Stukowski, "Visualization and analysis of atomistic simulation data with ovito–the open visualization tool," *Modelling and Simulation in Materials Science and Engineering*, vol. 18, p. 015012, 2010.

[92] M. de Koning and A. Antonelli, "Einstein crystal as a reference system in free energy estimation using adiabatic switching," *Physical Review E*, vol. 53, p. 465, 1996.

[93] T. Frolov and Y. Mishin, "Phases, phase equilibria, and phase rules in low-dimensional systems," *The Journal of Chemical Physics*, vol. 143, p. 044706, 2015.

[94] J. W. Gibbs, *The Collected Works of J. Willard Gibbs, Volume I: Thermodynamics*. Yale University Press, 1928.

[95] T. Frolov and M. Asta, "Step free energies at faceted solid-liquid interfaces from equilibrium molecular dynamics simulations," *The Journal of Chemical Physics*, vol. 137, p. 214108, 2012.

[96] J. J. Hoyt, M. Asta, and A. Karma, "Method for computing the anisotropy of the solid-liquid interfacial free energy," *Physical Review Letters*, vol. 86, p. 5530, 2001.

[97] Y. Mishin, "Calculation of the γ/γ' interface free energy in the ni–al system by the capillary fluctuation method," *Modelling and Simulation in Materials Science and Engineering*, vol. 22, p. 045001, 2014.

[98] C. A. Becker, J. J. Hoyt, D. Buta, and M. Asta, "Crystal-melt interface stresses: Atomistic simulation calculations for a lennard-jones binary alloy, stillinger-weber si, and embedded atom method ni," *Physical Review E*, vol. 75, p. 061610, 2007.

[99] T. Frolov and Y. Mishin, "Orientation dependence of the solid–liquid interface stress: atomistic calculations for copper," *Modelling and Simulation in Materials Science and Engineering*, vol. 18, p. 074003, 2010.

[100] R. Freitas, T. Frolov, and M. Asta, "Capillary fluctuations of surface steps: An atomistic simulation study for the model cu(111) system," *Physical Review E*, vol. 96, p. 043308, Oct 2017.

[101] D. G. Aarts, M. Schmidt, and H. N. Lekkerkerker, "Direct visual observation of thermal capillary waves," *Science*, vol. 304, pp. 847–850, 2004.

[102] N. C. Bartelt, R. M. Tromp, and E. D. Williams, "Step capillary waves and equilibrium island shapes on si (001)," *Physical Review Letters*, vol. 73, p. 1656, 1994.

[103] A. Braslau, P. S. Pershan, G. Swislow, B. M. Ocko, and J. Als-Nielsen, "Capillary waves on the surface of simple liquids measured by x-ray reflectivity," *Physical Review A*, vol. 38, p. 2457, 1988.

[104] B. M. Ocko, X. Z. Wu, E. B. Sirota, S. K. Sinha, and M. Deutsch, "X-ray reflectivity study of thermal capillary waves on liquid surfaces," *Physical Review Letters*, vol. 72, p. 242, 1994.

[105] L. G. MacDowell, J. Benet, N. A. Katcho, and J. M. Palanco, "Disjoining pressure and the film-height-dependent surface tension of thin liquid films: New insight from capillary wave fluctuations," *Advances in Colloid and Interface Science*, vol. 206, pp. 150–171, 2014.

[106] H.-C. Jeong and E. D. Williams, "Steps on surfaces: experiment and theory," *Surface Science Reports*, vol. 34, pp. 171–294, 1999.

[107] N. Bartelt, T. Einstein, and E. D. Williams, "The influence of step-step interactions on step wandering," *Surface Science*, vol. 240, pp. L591–L598, 1990.

[108] M. Constantin, C. Dasgupta, S. D. Sarma, D. Dougherty, and E. Williams, "Persistence and survival in equilibrium step fluctuations," *Journal of Statistical Mechanics: Theory and Experiment*, vol. 2007, p. P07011, 2007.

[109] E. D. Williams, "Surface steps and surface morphology: understanding macroscopic phenomena from atomic observations," *Surface Science*, vol. 299, pp. 502–524, 1994.

[110] K. G. Libbrecht, "Physical dynamics of ice crystal growth," *Annual Review of Materials Research*, vol. 47, pp. 271–295, 2017.

[111] D. Y. Sun, M. Asta, and J. J. Hoyt, "Crystal-melt interfacial free energies and mobilities in fcc and bcc fe," *Physical Review B*, vol. 69, p. 174103, 2004.

[112] D. Y. Sun, M. I. Mendelev, C. A. Becker, K. Kudin, T. Haxhimali, M. Asta, J. J. Hoyt, A. Karma, and D. J. Srolovitz, "Crystal-melt interfacial free energies in hcp metals: A molecular dynamics study of mg," *Physical Review B*, vol. 73, p. 024116, 2006.

[113] A. Karma, "Fluctuations in solidification," *Physical Review E*, vol. 48, p. 3441, 1993.

[114] F. Buff, R. Lovett, and F. Stillinger, "Interfacial density profile for fluids in the critical region," *Physical Review Letters*, vol. 15, p. 621, 1965.

[115] S. M. Foiles and J. Hoyt, "Computation of grain boundary stiffness and mobility from boundary fluctuations," *Acta Materialia*, vol. 54, pp. 3351–3357, 2006.

[116] J. Hoyt, Z. Trautt, and M. Upmanyu, "Fluctuations in molecular dynamics simulations," *Mathematics and Computers in Simulation*, vol. 80, pp. 1382–1392, 2010.

[117] P. Saidi, R. Freitas, T. Frolov, M. Asta, and J. Hoyt, "Free energy of steps at faceted (1 1 1) solid-liquid interfaces in the Si-Al system calculated using capillary fluctuation method," *Computational Materials Science*, vol. 134, pp. 184–189, jun 2017.

[118] S. W. Sides, G. S. Grest, and M.-D. Lacasse, "Capillary waves at liquid-vapor interfaces: A molecular dynamics simulation," *Physical Review E*, vol. 60, p. 6708, 1999.

[119] A. E. Ismail, G. S. Grest, and M. J. Stevens, "Capillary waves at the liquid-vapor interface and the surface tension of water," *The Journal of Chemical Physics*, vol. 125, p. 014702, 2006.

[120] M.-D. Lacasse, G. S. Grest, and A. J. Levine, "Capillary-wave and chain-length effects at polymer/polymer interfaces," *Physical Review Letters*, vol. 80, p. 309, 1998.

[121] R. L. Davidchack, J. R. Morris, and B. B. Laird, "The anisotropic hard-sphere crystal-melt interfacial free energy from fluctuations," *The Journal of Chemical Physics*, vol. 125, p. 094710, 2006.

[122] R. L. Davidchack and B. B. Laird, "Direct calculation of the hard-sphere crystal/melt interfacial free energy," *Physical Review Letters*, vol. 85, p. 4751, 2000.

[123] R. L. Davidchack and B. B. Laird, "Direct calculation of the crystal–melt interfacial free energies for continuous potentials: Application to the lennard-jones system," *The Journal of Chemical Physics*, vol. 118, pp. 7651–7657, 2003.

[124] J. R. Morris and X. Song, "The anisotropic free energy of the lennard-jones crystal-melt interface," *The Journal of Chemical Physics*, vol. 119, pp. 3920–3925, 2003.

[125] M. P. Gelfand and M. E. Fisher, "Finite-size effects in fluid interfaces," *Physica A: Statistical Mechanics and its Applications*, vol. 166, pp. 1–74, 1990.

[126] R. F. Kayser, "Effect of capillary waves on surface tension," *Physical Review A*, vol. 33, p. 1948, 1986.

[127] M. Kardar, *Statistical Physics of Fields*. Cambridge University Press, 2007.

[128] W. Li, H. Duan, K. Albe, and J. Weissmüller, "Line stress of step edges at crystal surfaces," *Surface Science*, vol. 605, pp. 947–957, 2011.

[129] L. E. Shilkrot and D. J. Srolovitz, "Elastic field of a surface step: Atomistic simulations and anisotropic elastic theory," *Physical Review B*, vol. 53, p. 11120, 1996.

[130] R. Delgado-Buscalioni, E. Chacon, and P. Tarazona, "Hydrodynamics of nanoscopic capillary waves," *Physical Review Letters*, vol. 101, p. 106102, 2008.

[131] J. Benet, L. G. MacDowell, and E. Sanz, "Computer simulation study of surface wave dynamics at the crystal-melt interface," *The Journal of Chemical Physics*, vol. 141, p. 034701, 2014.

[132] M. Jorge, P. Jedlovszky, and M. N. D. Cordeiro, "A critical assessment of methods for the intrinsic analysis of liquid interfaces. 1. Surface site distributions," *The Journal of Physical Chemistry C*, vol. 114, pp. 11 169–11 179, 2010.

[133] D. B. Abraham, "Capillary waves and surface tension: an exactly solvable model," *Physical Review Letters*, vol. 47, p. 545, 1981.

[134] R. Collepardo-Guevara, I. R. Craig, and D. E. Manolopoulos, "Proton transfer in a polar solvent from ring polymer reaction rate theory," *The Journal of Chemical Physics*, vol. 128, 2008.

[135] S. Hammes-Schiffer and J. C. Tully, "Proton transfer in solution: Molecular dynamics with quantum transitions," *The Journal of Chemical Physics*, vol. 101, 1994.

[136] T. F. Miller III and D. E. Manolopoulos, "Quantum diffusion in liquid water from ring polymer molecular dynamics," *The Journal of Chemical Physics*, vol. 123, 2005.

[137] D. Marx, M. E. Tuckerman, J. Hutter, and M. Parrinello, "The nature of the hydrated excess proton in water," *Nature*, vol. 397, 1999.

[138] P. A. F. P. Moreira and M. de Koning, "Nuclear quantum fluctuations in ice Ih," *Physical Chemistry Chemical Physics*, vol. 17, 2015.

[139] B. Pamuk, J. M. Soler, R. Ramírez, C. Herrero, P. Stephens, P. Allen, and M.-V. Fernández-Serra, "Anomalous nuclear quantum effects in ice," *Physical Review Letters*, vol. 108, 2012.

[140] A. Haziot, X. Rojas, A. D. Fefferman, J. R. Beamish, and S. Balibar, "Giant plasticity of a quantum crystal," *Physical Review Letters*, vol. 110, 2013.

[141] E. J. L. Borda, W. Cai, and M. de Koning, "Ideal shear strength of a quantum crystal," *Physical Review Letters*, vol. 112, 2014.

[142] L. Proville, D. Rodney, and M.-C. Marinica, "Quantum effect on thermally activated glide of dislocations," *Nature Materials*, vol. 11, 2012.

[143] B. Barvinschi, L. Proville, and D. Rodney, "Quantum Peierls stress of straight and kinked dislocations and effect of non-glide stresses," *Modelling and Simulation in Materials Science and Engineering*, vol. 22, 2014.

[144] M. L. Dos Reis, A. Choudhury, and L. Proville, "Ubiquity of quantum zero-point fluctuations in dislocation glide," *Physical Review B*, vol. 95, 2017.

[145] W. Spitzig and A. Keh, "The effect of orientation and temperature on the plastic flow properties of iron single crystals," *Acta Metallurgica*, vol. 18, 1970.

[146] E. Kuramoto, Y. Aono, and K. Kitajima, "Thermally activated slip deformation of high purity iron single crystals between 4.2 K and 300 K," *Scripta Metallurgica*, vol. 13, 1979.

[147] S. Takeuchi, T. Hashimoto, and K. Maeda, "Plastic deformation of bcc metal single crystals at very low temperatures," *Transactions of the Japan Institute of Metals*, vol. 23, 1982.

[148] E. Kubamoto, Y. Aono, K. Kitajima, K. Maeda, and S. Takeuchi, "Thermally activated slip deformation between 0.7 and 77 K in high-purity iron single crystals," *Philosophical Magazine A*, vol. 39, 1979.

[149] J. Marian, W. Cai, and V. V. Bulatov, "Dynamic transitions from smooth to rough to twinning in dislocation motion," *Nature Materials*, vol. 3, 2004.

[150] J. Chaussidon, M. Fivel, and D. Rodney, "The glide of screw dislocations in bcc Fe: atomistic static and dynamic simulations," *Acta Materialia*, vol. 54, 2006.

[151] M. Itakura, H. Kaburaki, and M. Yamaguchi, "First-principles study on the mobility of screw dislocations in bcc iron," *Acta Materialia*, vol. 60, 2012.

[152] L. Proville, L. Ventelon, and D. Rodney, "Prediction of the kink-pair formation enthalpy on screw dislocations in α-iron by a line tension model parametrized on empirical potentials and first-principles calculations," *Physical Review B*, vol. 87, 2013.

[153] L. Ventelon, F. Willaime, E. Clouet, and D. Rodney, "Ab initio investigation of the Peierls potential of screw dislocations in bcc Fe and W," *Acta Materialia*, vol. 61, 2013.

[154] S. L. Frederiksen and K. W. Jacobsen, "Density functional theory studies of screw dislocation core structures in bcc metals," *Philosophical magazine*, vol. 83, pp. 365–375, 2003.

[155] M. Gilbert, S. Queyreau, and J. Marian, "Stress and temperature dependence of screw dislocation mobility in α-fe by molecular dynamics," *Physical Review B*, vol. 84, 2011.

[156] G. A. Voth, D. Chandler, and W. H. Miller, "Rigorous formulation of quantum transition state theory and its dynamical corrections," *The Journal of Chemical Physics*, vol. 91, 1989.

[157] T. J. Hele and S. C. Althorpe, "Derivation of a true ($t \to 0^+$) quantum transition-state theory. I. Uniqueness and equivalence to ring-polymer molecular dynamics transition-state-theory," *The Journal of chemical physics*, vol. 138, p. 084108, 2013.

[158] T. E. Markland, S. Habershon, and D. E. Manolopoulos, "Quantum diffusion of hydrogen and muonium atoms in liquid water and hexagonal ice," *The Journal of Chemical Physics*, vol. 128, 2008.

[159] T. E. Markland, J. A. Morrone, B. J. Berne, K. Miyazaki, E. Rabani, and D. R. Reichman, "Quantum fluctuations can promote or inhibit glass formation," *Nature Physics*, vol. 7, 2011.

[160] T. E. Markland, J. A. Morrone, K. Miyazaki, B. J. Berne, D. R. Reichman, and E. Rabani, "Theory and simulations of quantum glass forming liquids," *The Journal of Chemical Physics*, vol. 136, 2012.

[161] I. R. Craig and D. E. Manolopoulos, "Chemical reaction rates from ring polymer molecular dynamics," *The Journal of Chemical Physics*, vol. 122, 2005.

[162] I. R. Craig and D. E. Manolopoulos, "A refined ring polymer molecular dynamics theory of chemical reaction rates," *The Journal of Chemical Physics*, vol. 123, 2005.

[163] T. J. Hele, M. J. Willatt, A. Muolo, and S. C. Althorpe, "Communication: Relation of centroid molecular dynamics and ring-polymer molecular dynamics to exact quantum dynamics," *Journal of Chemical Physics*, vol. 142, 2015.

[164] T. J. H. Hele, "Quantum transition state theory," Ph.D. dissertation, University of Cambridge, 2014.

[165] T. S. Rahman, A. Kara, and S. Durukanoğlu, "Structural relaxations, vibrational dynamics and thermodynamics of vicinal surfaces," *Journal of Physics: Condensed Matter*, vol. 15, p. S3197, 2003.

[166] S. Durukanoğlu, A. Kara, and T. S. Rahman, "Local and excess vibrational free energies of stepped metal surfaces," *Physical Review B*, vol. 67, p. 235405, 2003.

[167] R. C. Nelson, T. L. Einstein, S. V. Khare, and P. J. Rous, "Energies of steps, kinks, and defects on Ag (100) and Ag (111) using the embedded atom method, and some consequences," *Surface Science*, vol. 295, pp. 462–484, 1993.

[168] B. J. Block, S. Kim, P. Virnau, and K. Binder, "Anisotropic interfacial tension, contact angles, and line tensions: A graphics-processing-unit-based monte carlo study of the ising model," *Physical Review E*, vol. 90, p. 062106, 2014.

[169] W. Cai, V. V. Bulatov, J. Chang, J. Li, and S. Yip, "Periodic image effects in dislocation modelling," *Philosophical Magazine*, vol. 83, 2003.

[170] P. Gordon, T. Neeraj, and M. Mendelev, "Screw dislocation mobility in BCC metals: a refined potential description for α-Fe," *Philosophical Magazine*, vol. 91, 2011.

[171] A. A. Correa, L. X. Benedict, D. A. Young, E. Schwegler, and S. A. Bonev, "First-principles multiphase equation of state of carbon under extreme conditions," *Physical Review B*, vol. 78, 2008.

[172] A. Stukowski, "Structure identification methods for atomistic simulations of crystalline materials," *Modelling and Simulation in Materials Science and Engineering*, vol. 20, p. 045021, 2012.

[173] T. F. Miller III, "Isomorphic classical molecular dynamics model for an excess electron in a supercritical fluid," *The Journal of Chemical Physics*, vol. 129, 2008.

[174] A. R. Menzeleev, N. Ananth, and T. F. Miller III, "Direct simulation of electron transfer using ring polymer molecular dynamics: Comparison with semiclassical instanton theory and exact quantum methods," *The Journal of Chemical Physics*, vol. 135, 2011.

[175] G. Grimvall, *Thermophysical properties of materials*. North Holland, 2011.

Appendix A:

Convergence of thermodynamic integration for steps

In this appendix we present analyses of the statistical sampling errors and numerical convergence for the thermodynamic integration results presented in sec. 3.5.3.

The numerical integration in eq. (3.24) was performed considering a linear interpolation of the excess quantities shown in fig. 3.7. We have tested interpolation schemes using polynomials of different orders and the difference compared to the linear interpolation was negligible. The reason is that the integrand of eq. (3.24) is already smooth for the linear interpolation due to the renormalization of the excess quantities by T^2 or T, as shown in fig. A.1. The second term in the integrand of eq. (3.24) (involving the excess stress) was found to be at least 50 times smaller than the first term (involving the excess energy) and therefore it is numerically negligible for the result of the integral.

We have chosen $T_0 = 400\,\mathrm{K}$ as the initial point to perform the thermodynamic integrations to compute the temperature dependence of γ^{st}. The integration was performed in both directions, from T_0 to T_{m} and from T_0 to $\approx 0\,\mathrm{K}$. The choice of $T_0 = 400\,\mathrm{K}$ as the initial integration point in fig. 3.7 was arbitrary and, within the statistical accuracy of the calculations, it should not influence the final results for γ^{st}. The free energy calculated with the FL method at any of the other temperatures (red points in fig. 3.6) should all be equally valid as an initial integration point. Thus, to verify the accuracy of the calculations, we have performed the integration in eq. (3.24) starting from all the different T_0 values for which we have available FL simulations. The result is shown in fig. A.2a where we plot the value of γ^{st} at $T_{\mathrm{m}} = 1327\,\mathrm{K}$ obtained from the integration of eq. (3.24) using different initial points. The error bar of each point corresponds to the error of the mean for the particular value of T_0. The error in the mean was obtained by a resampling process of the excess quantities and the initial value of γ^{st} used in the integration: each of the data points involved in the integration was picked randomly from a normal distribution with a mean value corresponding to the calculated average value of that quantity, and the standard deviation corresponding the calculated standard error of the mean value. The linear interpolation and numerical integration of the excess quantities for the given choice of T_0 was performed and the resulting step free energy at T_{m} was averaged over 2000 of these resampled data sets. For completeness we also show in fig. A.2b the $\gamma^{\mathrm{st}}(T)$ curve obtained from the integration starting from the different T_0 values. From figs. A.2a and A.2b it is clear that the choice of the initial integration point

The results presented in this appendix and in chapter 3 have been published as a regular article with title "*Step free energies at faceted solid surfaces: Theory and atomistic calculations for steps on the Cu(111) surface*" in Physical Review B **95**, 155444 (2017) by Rodrigo Freitas, Timofey Frolov, and Mark Asta [55]. The material is presented here with the permission of co-authors and publishers.

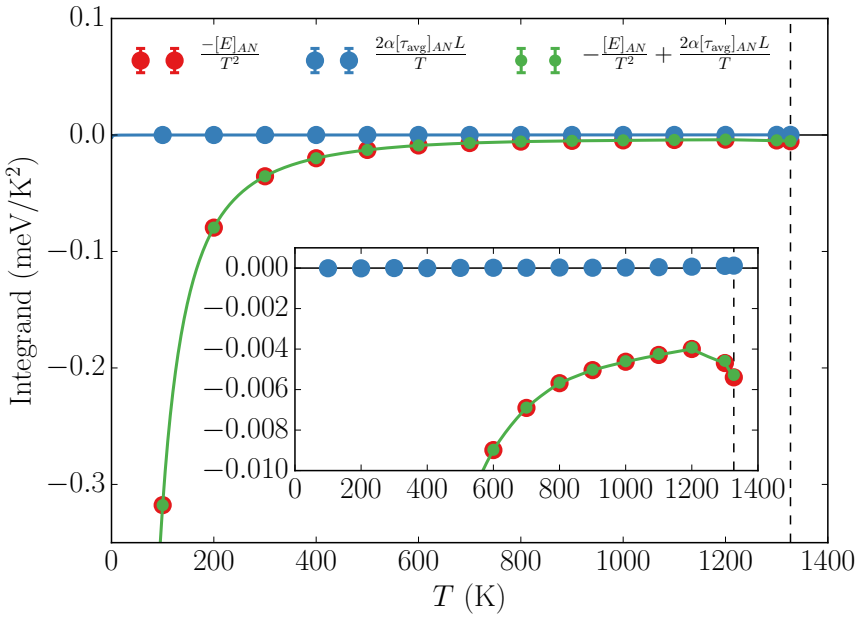

Figure A.1: Temperature dependence of each term of the integrand of eq. (3.24). Notice how the integrand term that involves the step excess stress $[\tau_{\text{avg}}]_{AN}$ is much smaller than the term involving the step excess energy $[E]_{\text{AN}}$. The solid lines are the result of the linear interpolation of the excess quantities multiplied by the factor of each term in the integrand.

T_0 does not influence the final result of the thermodynamic integration significantly.

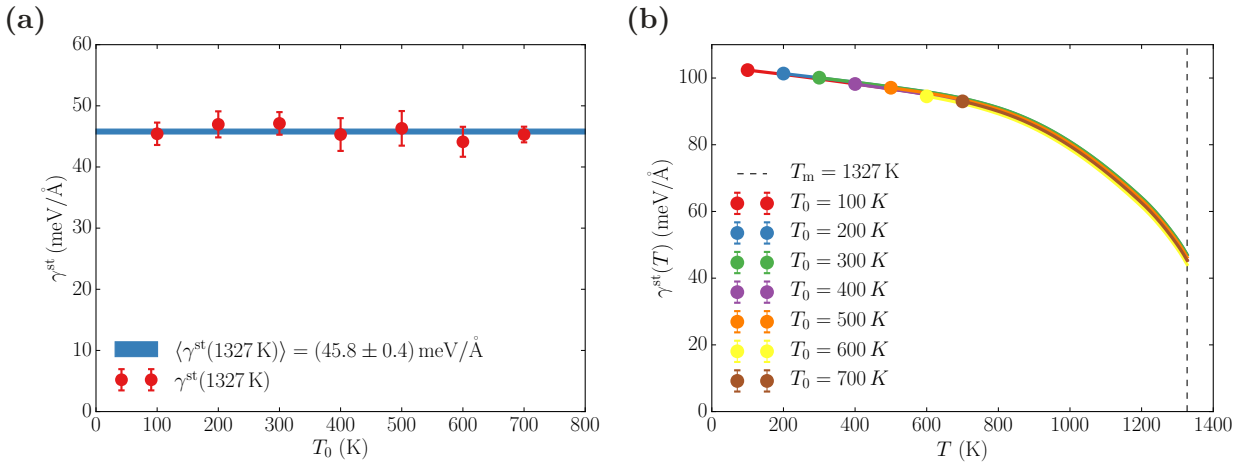

Figure A.2: **(a)** Step free energy at $T_{\text{m}} = 1327\,\text{K}$ calculated with the thermodynamic integration method using different initial points $\gamma^{\text{st}}(T_0)$ for the integration. The blue stripe is centered on the average taken considering all choices for T_0 from 100 K to 700 K, and the width of this stripe corresponds to the standard deviation of these values for $\gamma^{\text{st}}(1327\,\text{K})$. **(b)** Temperature dependence of the step free energy obtained using different reference temperatures T_0 for the thermodynamic integration [eq. (3.24)].

Appendix B:

Simulation of quantum and classical dislocation motion

This appendix presents the details of the atomistic simulations results of chapter 5, including methods and algorithms employed, details of the dislocation motion analysis, and an extended discussion of the applicability of RPMD for modeling the dynamics of dislocation motion.

B.1 Molecular Dynamics simulations of dislocation motion

All atomistic simulations were performed in a volume shaped as a rectangular prism oriented as shown in the inset in fig. 5.1 with dimensions (at $T = 0\,\mathrm{K}$) $L_{[111]} = 61.8\,\text{Å}$, $L_{[1\bar{1}0]} = 145.4\,\text{Å}$, and $L_{[11\bar{2}]} = 191.2\,\text{Å}$ containing $148,500$ atoms. Periodic boundary conditions were employed along the [111] and the $[1\bar{1}0]$ directions, and free-surface boundary conditions were employed along the $[11\bar{2}]$ direction. A $\frac{1}{2}\langle 111\rangle$ screw dislocation was inserted in the center of the simulation volume as described in refs. [10, 169]. Atomic positions in the fixed layers at the top and at the bottom of the simulation volume were corrected to enforce translational invariance along the dislocation motion direction ($\hat{\mathbf{y}}$-axis or $[1\bar{1}0]$).

Classical MD simulations were performed using LAMMPS [29] code with an embedded-atom method (EAM) potential previously developed for the bcc α-phase of elemental iron [170]. The simulation timestep was $\Delta t = 3\,\mathrm{fs}$, $\approx 1/40\,\mathrm{th}$ of the period of the highest frequency mode in the phonon spectrum computed for this model system. The Debye temperature, $T_\mathrm{D} = (400 \pm 20)\,\mathrm{K}$, was estimated from the same phonon spectrum, as described in sec. B.6 [171]. Temperature was maintained near-constant (NVT ensemble) in each simulation using a Langevin thermostat with the temperature relaxation time of 30 ps which was found to be sufficiently gentle not to affect the flow stress when compared to corresponding microcanonical simulations. Classical NVT simulations were performed at temperatures ranging from $0.1\,\mathrm{K}$ to $300\,\mathrm{K}$ using per-atom volumes adjusted at each temperature to maintain internal pressure close to zero. Prior to running mobility simulations, the model was thermalized at the desired temperatures for 300 ps after which two rigid layers (slabs) of atoms at the top and the bottom of the simulation volume (blue atoms in fig. 5.1) were displaced at a constant velocity in the opposite directions along the $\hat{\mathbf{x}}$-axis ([111]). The slab velocity was adjusted so as to make the dislocation move at a certain average velocity ($50\,\mathrm{m/s}$ or $10\,\mathrm{m/s}$)

The results presented in this appendix, section 2.4, and chapter 5 have been submitted to publication as an article with title "*Quantum effects on dislocation motion from Ring-Polymer Molecular Dynamics*" by Rodrigo Freitas, Mark Asta, and Vasily V. Bulatov [52]. The material is presented here with the permission of the coauthors.

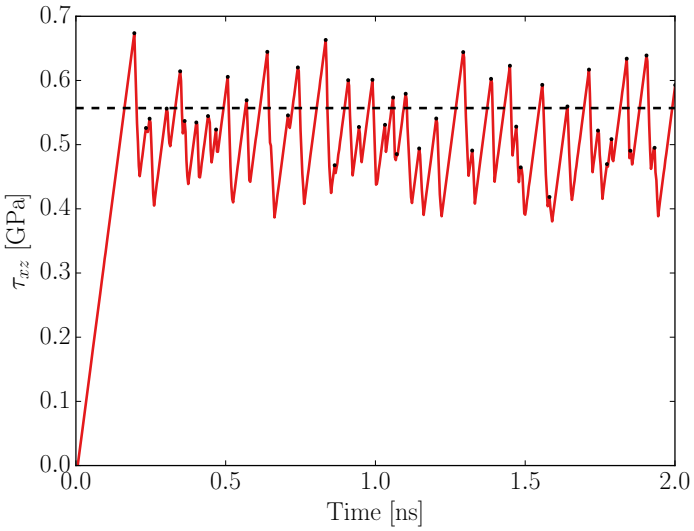

Figure B.1: Shear stress as a function of time computed in a classical MD simulation of the screw dislocation in α-iron subjected to straining at a constant rate at $T = 30\,\mathrm{K}$. The dislocation moves in a stop-and-go fashion: the red line is the τ_{xz} (shear) component of the instantaneous stress and the black dots mark times and stress levels at which the dislocation started to glide. The black dashed line is the flow stress at this temperature computed as the average over the starting stress levels (black dots).

once its motion becomes steady after an initial transient period. The straining rate was kept constant for 10 ns over which the τ_{xz} component of the internal stress was recorded as a measure of the flow stress. A stress versus time curve obtained in one such MD simulation is shown in fig. B.1.

B.2 Ring-Polymer Molecular Dynamics simulations

The RPMD simulations were performed using our own implementation of the method in LAMMPS, as described in sec. 2.4. Except for the significantly greater number of degrees of freedom – $3N$ in MD and $3NP$ in RPMD – and a shorter time step, all other details of RPMD simulations were the same as in the classical MD simulations described in sec. B.1.

The number of beads P (system's replicas) was selected individually for each temperature based on convergence of the system's energy and internal stress-tensor with the number of beads. Figures B.2 and B.3 present data obtained in one such convergence study at $T = 30\,\mathrm{K}$. Based on this data we elected to use 40 beads for RPMD simulations at this particular temperature. Based on similar analyses we ended up using 200, 100, 50, 40, 30, and 20 beads at temperatures 5 K, 10 K, 20 K, 30 K, 40 K, and 50 K, respectively. The timestep was set equal to 1/25th of the period of the highest frequency eigenmode of the ring-polymers [36] which in practice resulted in time steps of 0.48 fs for 5 K, 10 K, 20 K, and 30 K, and 0.40 fs for 40 K and 50 K. Similar to the classical MD, we adjusted the per-atom volume at each temperature in the quantum system to maintain its internal pressure close to zero; in practice the difference in the zero-pressure lattice parameter between MD and RPMD was

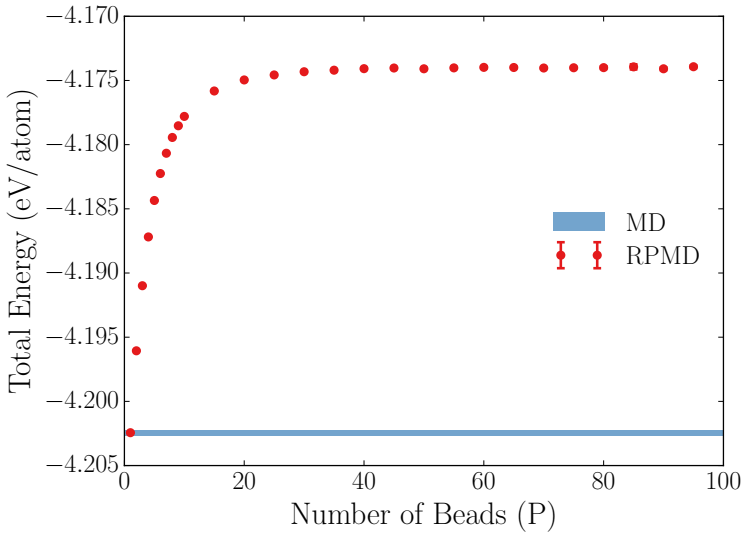

Figure B.2: Average per-atom energy in the EAM model of α-iron computed in RPMD simulations as a function of the number of beads at $T = 30\,\mathrm{K}$.

only of about $\pm 0.05\%$ (at the same temperature) and had no appreciable effect on dislocation motion.

To induce dislocation motion and to compute the Peierls stress we used the same procedures as in the classical MD simulations. To additionally verify that our RPMD predictions are accurate, we repeated RPMD simulations at $T = 40\,\mathrm{K}$ and $50\,\mathrm{K}$ using twice as many beads as was judged necessary for fully converged simulations and observed no appreciable changes in the results. Additionally, we verified that our flow stress predictions are converged with respect to time step, by repeating our RPMD simulations at $T = 30\,\mathrm{K}$ with time steps of 0.20 and 0.10 fs, i.e. $\frac{1}{2}$ and $\frac{1}{4}$ of 0.40 fs deemed acceptable at this temperature.

B.3 Calculation of the zero-point energy and the radius of gyration

RPMD simulations of a perfect bcc lattice of iron with $5,488$ atoms were used to compute the ZPE and r_G shown in figs. 5.3 and 5.4. Simulations were performed at the same temperatures and with the same numbers of beads P as in sec. B.2. Additionally, RPMD simulations were performed at higher temperatures: 100 K (with 16 beads), 150 K (12 beads), 200 K (12 beads), 250 K (10 beads), 300 K (9 beads), 400 K (8 beads), 500 K (7 beads), and 600 K (7 beads). The classical energies shown on the plot were extracted from MD simulations of the same system at the same temperatures. The radius of gyration r_G of the ring-polymers in RPMD shown in figure 5.4 was computed as

$$r_\mathrm{G} = \left\langle \frac{1}{P} \sum_{i=1}^{P} \left| \mathbf{r}_{n,i} - \bar{\mathbf{r}}_n \right|^2 \right\rangle^{1/2}$$

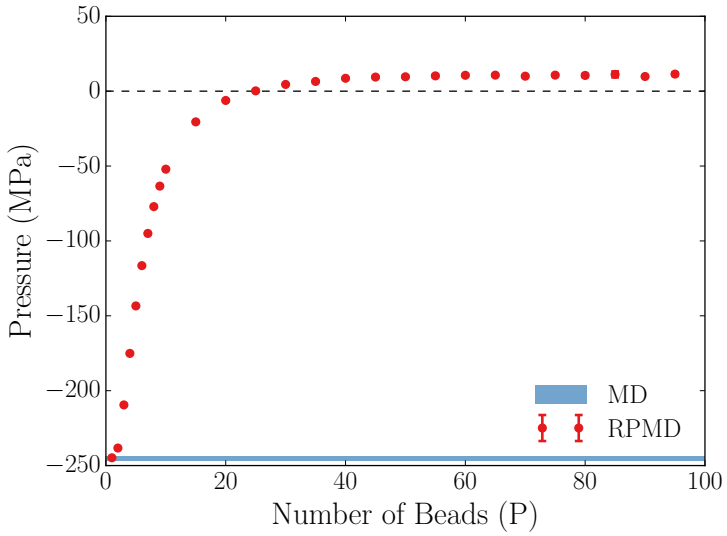

Figure B.3: Average pressure in the EAM model of α-iron computed in RPMD simulations as a function of the number of beads at $T = 30\,\mathrm{K}$.

where $\langle \ldots \rangle$ denotes the canonical ensemble average and

$$\bar{\mathbf{r}}_n = \frac{1}{P} \sum_{i=1}^{P} \mathbf{r}_{n,i} \tag{B.1}$$

is the ring-polymer centroid. The radius of gyration of the free atom shown in the same figure was computed analytically [50]:

$$r_{\mathrm{G}}^{\mathrm{free}} = \frac{1}{2} \sqrt{\frac{\hbar^2}{m k_{\mathrm{B}} T}}.$$

B.4 Dislocation motion analysis

For RPMD simulations to be representative of stochastic dynamics of dislocation motion, it was necessary to assess whether the dislocation spends sufficient time in its energy basins between basin-to-basin transitions. The analysis was performed on the snapshots of atom centroid positions, eq. (B.1), saved every 1.4 fs along the simulated RPMD trajectories. Within each time snapshot the dislocation's position was taken as a center of mass of atom centroids that were deemed "defective" according to the adaptive Common Neighbor Analysis [172, 91]; in our low-temperature RPMD simulations most such "defective" atoms belong to the dislocation core. Figure B.4 is an example of a dislocation trajectory extracted from one of our RPMD simulations. The trajectory reveals a stop-and-go character of dislocation motion in which periods of residence in the energy basins (horizontal segments) are interrupted by more or less fast transitions between the basins (step segments). Duration of the residence periods decreases with increasing temperature (fig. B.5) and at temperatures above 50 K distinct residence periods are no longer recognized. Short of running RPMD

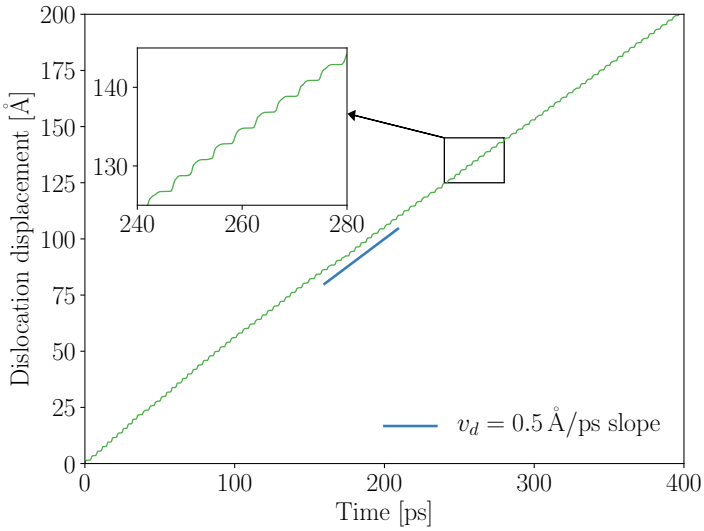

Figure B.4: Position of the screw dislocation as a function of time extracted from a classical MD simulation of dislocation motion at $T = 30\,\mathrm{K}$. The dislocation' moves in a stop-and-go fashion, each plateau representing time spent by the dislocation sampling a single Peierls valley.

simulations at a lower dislocation velocity (which would extend the average residence periods but also raise the computational cost) we no longer consider our RPMD simulations at temperatures above 50 K to be representative of dislocation motion in our model of α-iron.

B.5 Applicability of RPMD for modeling dynamics of dislocation motion

Although RPMD is decidedly successful [49] in describing quantum dynamics of many condensed-phase systems of interest, the method has an important limitation [173, 174] in neglecting effects due to quantum coherence in real-time dynamics. Being an equilibrium statistical approach, RPMD implicitly assumes that thermal fluctuations lead to quantum decoherence on a timescale much shorter than any natural timescale of the system in consideration. This has been shown to bea good approximation for many condensed-phase problems [49] in which dynamics is defined by equilibrium quantum statistics and not by quantum coherence. Hence, for RPMD to be accurate in describing the motion of $\frac{1}{2}\langle 111\rangle$ dislocations in α-iron, validity of the thermal decoherence hypothesis has to be carefully examined.

Dynamics of screw dislocation motion in α-iron and similar metals can be reasonably described as the motion of a particle on the Peierls energy landscape [9], fig. B.6, where the dislocation moves by overcoming energy barriers (humps) representing the intrinsic lattice resistance to dislocation motion. The effect of applied stress is to tilt this landscape, making the dislocation more likely to jump to the next Peierls valley of lower energy. Taking the decoherence assumption into consideration, for RPMD to be representative of this dynamics the dislocation needs to be given sufficient time between jumps to thermalize and eliminate quantum coherence effects. A practical way to determine validity of the thermal decoherence

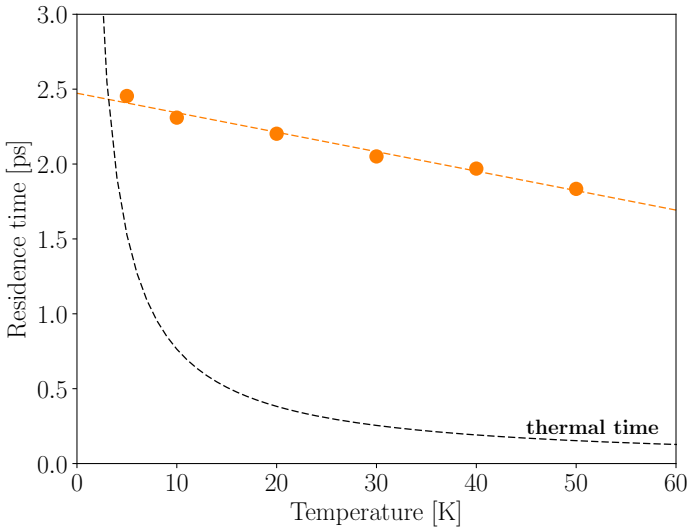

Figure B.5: Average residence time of the screw dislocations in its Peierls valleys extracted from RPMD simulations performed at different temperatures.

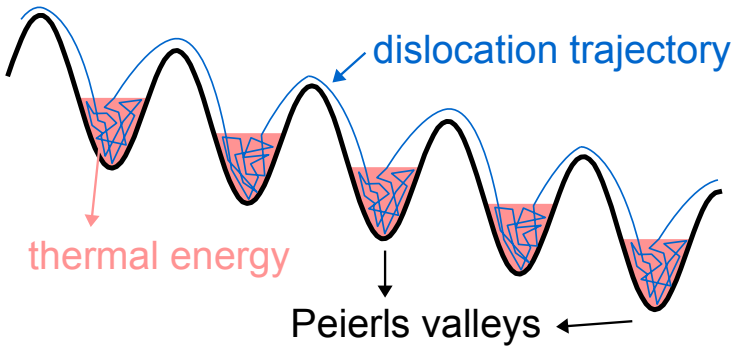

Figure B.6: Illustration of the Peierls model for the energetic landscape for dislocation motion.

assumption is to compare the residence time τ of the dislocation in each Peierls valley with time $\beta\hbar$ known as thermal time. If $\tau \gg \beta\hbar$ the system's dynamics is defined by its equilibrium thermal properties and RPMD should be applicable. On the other hand, when $\tau < \beta\hbar$, the system's dynamics is likely to have important contributions from quantum coherence effects making applicability of RPMD questionable.

We analyzed the pattern of dislocation motion in our RPMD simulations, as described in sec. B.4. Figure B.4 shows position of the screw dislocation as a function of time extracted from an RPMD simulation at $T = 30\,\mathrm{K}$. Each plateau seen on the dislocation trajectory in fig. B.4 indicates a more or less extended residence in a single Peierls valley, the length of the plateau defining the residence time τ. Shown in fig. B.5 is the average residence time τ extracted from our RPMD simulations performed at different temperatures. Comparing τ with the thermal time $\beta\hbar$ in fig. B.5, the average residence time is comfortably longer than the thermal time at temperatures above $5\,\mathrm{K}$: τ is approximately 12 times larger than $\beta\hbar$ at $50\,\mathrm{K}$ and 2 times larger at $5\,\mathrm{K}$. On the other hand, the average residence time monotonically

decreases with increasing temperature where the dislocation has less time to thermalize in each Peierls valley. At temperatures above 50 K the residence plateaus on the dislocation trajectory become rather short and eventually indistinguishable. In order to comply with the assumptions involved in the derivation of the RPMD method, we restrict our RPMD simulations to $T \geq 5\,\mathrm{K}$ to ensure that quantum coherence effects can be neglected. Moreover, to assure that dislocation motion is defined by equilibrium quantum statistics we limit our simulation to temperatures $T \leq 50\,\mathrm{K}$ were the system is given sufficient time to sample each Peierls valley before moving to the next.

B.6 Debye temperature calculation

Consider a crystal composed of N atoms, one per unit cell. The phonon density of states of this system is given by [175]

$$F(\omega) = \frac{\rho}{(2\pi)^3} \sum_{\lambda=1}^{3} \int_{\Sigma} \frac{\mathrm{d}S}{|\boldsymbol{\nabla}_{\mathbf{k}} \omega_\lambda(\mathbf{k})|}, \tag{B.2}$$

where $\rho \equiv V/N$ is the atom density, λ labels the phonon branch (all branches are acoustic for this system), $\omega_\lambda^2(\mathbf{k})$ are the eigenvalues of the dynamical matrix of this system, $\mathbf{k}$ is the wave vector, and the integral is over a surface Σ on which $\omega_\lambda(\mathbf{k}) = \omega$. The density of states defined above is normalized such that

$$\int_0^\infty F(\omega)\,\mathrm{d}\omega = 3, \tag{B.3}$$

thus $F(\omega)$ is a density of states "per atom".

In the Debye model the dispersion relation for all branches of the real crystal is approximated by $\omega_\lambda(\mathbf{k}) = v_\mathrm{s}\,|\mathbf{k}|$ for $|k| < k_\mathrm{D}$ and zero otherwise, where v_s is the sound velocity in the Debye model. The density of states for this model can be computed using the dispersion relation and eq. (B.2): $F_\mathrm{D}(\omega) = 9\omega^2/\omega_\mathrm{D}^3$, where $\omega_\mathrm{D} = v_\mathrm{s} k_\mathrm{D}$ and the cutoff value k_D is chosen such that $F_\mathrm{D}(\omega)$ obeys the normalization condition, eq. (B.3). The so-called Debye temperature is defined as: $k_\mathrm{B}\Theta_\mathrm{D} = \hbar\omega_\mathrm{D}$. The Debye model is usually good in describing the low frequency part of the density of states of real crystals, since the linearity of the dispersion relation always holds in the small wave vector (or long-wavelength) limit for the acoustic branches of any solid.

One of the benefits of the Debye model is that all physical properties derivable from its density of states depend only on one parameter: the cutoff wave vector k_D or, equivalently, the Debye temperature θ_D. Thus, given the phonon density of states of the real crystal, $F(\omega)$, it is of interest to compute the Debye temperature for that system. In order to derive a method to estimate θ_D we introduce the moment frequencies $\omega(n) = \langle\omega^n\rangle^{1/n}$, where

$$\langle\omega^n\rangle \equiv \frac{\int_0^\infty \omega^n F(\omega)\,\mathrm{d}\omega}{\int_0^\infty F(\omega)\,\mathrm{d}\omega}. \tag{B.4}$$

Note that $\omega(n)$ is a parameter giving some averaged information about the phonon density of states. For the Debye model all $\omega(n)$ can be computed analytically and they can be related

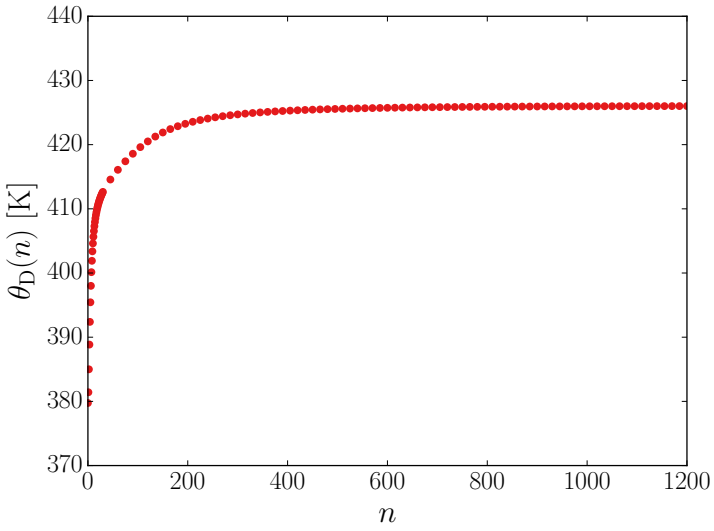

Figure B.7: Debye temperature of a system composed of elemental iron, as described in chapter 5. The predicted Debye temperature varies slightly with the moment frequency, eq. (B.5), used to estimate it.

directly to the Debye frequency:

$$\omega(n) = \left(\frac{3}{n+3}\right)^{1/n} \omega_D \qquad \text{or} \qquad \omega_D = \left(\frac{n+3}{n+3}\right)^{1/n} \omega(n), \tag{B.5}$$

where $n \geq 1$. Hence, given $F(\omega)$ one can compute $\omega(n)$ using eq. (B.4) and obtain ω_D (or, equivalently, θ_D) using eq. (B.5). In a system that strictly obeys the Debye model all $\omega(n)$ used in eq. (B.5) result in the same cutoff frequency ω_D, and thus on the same Debye temperature. This is not true for a real system, where there might be a small variation in the predicted Debye temperature depending on the $\omega(n)$ used to compute it. We denote $\omega_D(n)$ the Debye temperature obtained from using the moment frequency $\omega(n)$. Note that this variation of the predicted Debye temperature is not a problem due to using eq. (B.5) to estimate θ_D. Different Debye temperatures are obtained because we are trying to adjust a physical model to a real system. For example, we could have adjusted the linear Debye dispersion relation to the low frequency part of $F(\omega)$, and yet another Debye temperature for the system would have been predicted. Nevertheless, it is reasonable that if the Debye model is a good approximation for the real physical system, then all methods for predicting the Debye temperature will result in values that are numerically close to each other.

In fig. B.7 we show the estimate Debye temperature $\theta_D(n)$ for the system of elemental iron studied in chapter 5. Given the variation observed in $\theta_D(n)$ we estimate the Debye temperature of this system to be $\theta_D = (404 \pm 22)\,\mathrm{K}$.